UiO : Department of Informatics
University of Oslo

Investigating window-length and array processing recipes in microbarom direction-of-arrival estimation

Sverre L. Hartveit
Master's Thesis, Spring 2023

Abstract

The aim of this thesis has been to optimise the beamformers when studying infrasound, more precisely, microbaroms. Microbaroms are infrasound generated by standing ocean waves in marine storms. Processing these signals can be challenging compared to processing a transient signal. The beamformers we consider is Capon's method and delay-and-sum. After building a framework of how to process longer streams on infrasound and predicting the direction-of-arrival of microbaroms, we considered a stream of infrasound recorded from an infrasound array, IS37 at Bardufoss. This stream is complex and has multiple acoustic signals in the overlapping frequency band. We find that Capon's method was sensitive to present incoherent noise and struggles more to produce good estimates under such conditions. Therefore, the method benefits from using longer window lengths, as the variance is reduced. The delay-and-sum beamformer was more robust and handled the incoherent noise much better. Due to the robustness, we found that we can use shorter window lengths to reduce the amount of noise in the plots and the processing time. Finally, we found that Capon's method was more sensitive to noise than the delay-and-sum beamformer and that the resolution of the delay-and-sum beamformer was higher than using Capon's method.

Contents

List of Figures

List of Tables

Acknowledgments

I would like to thank my supervisor and sparring partner Sven Peter Näsholm. Your time and dedication for introducing me to the infrasound world has been deeply appreciated.

CHAPTER 1

Introduction

1.1 Problem statement and objectives

Mainstream infrasound data processing recipes and frameworks were typically developed for explosion monitoring purposes, in particular in the context of monitoring compliance with the Comprehensive Nuclear-Test-Ban Treaty (Mialle et al., 2019; Marcillo et al., 2019). This treaty bans nuclear test explosions and is monitored by an international network of sensors that include infrasound arrays to detect atmospheric explosions (for example, Dahlman et al., 2011; Marty, 2019).

However, quasicontinuous low-frequency microbarom infrasound signals, a source of noise in explosion monitoring, differ greatly in signature and nature from transient explosion infrasound. Microbaroms are infrasound generated by nonlinear interactions between counterpropagating ocean swell, and there is potential in exploiting these signals to probe the dynamics of the middle atmosphere (Donn and Rind, 1971; Garcés et al., 2004; Le Pichon, Ceranna et al., 2006; Fricke et al., 2014; Smets and Evers, 2014; Smets, Assink, Le Pichon et al., 2016; Vorobeva et al., 2021), where otherwise probing technologies are sparse.

In this study, we seek to explore various approaches to adjust the infrasound array signal processing to provide an array signal processing output that is appropriate for monitoring the direction-of-arrival of microbarom infrasound.

We aim to compare a range of array signal processing recipes with the goal of providing a robust estimate for the direction-of-arrival of the dominating incoming microbarom wavefront. All recipes rely on estimating the stacked signal power as a function of the direction-of-arrival. The direction where this stacked power is maximised is considered the dominating wavefront direction-of-arrival.

A key processing setup parameter for which an objective is to assess the effect is the processing time-window length. Moreover, comparisons are made between the use of Capon's method and conventional delay-and-sum beamforming to estimate the beamformer output power.

The aim of learning more about appropriate processing recipes in a wider context and building an intuitive understanding of the nature of transient infrasound signals, in contrast to longer-duration signals, was also investigated as part of the project. This involved a smaller study to replicate the results of Lyons et al. (2020), which

is a peer-reviewed research paper that considers open data from infrasound arrays in Alaska related to shorter-duration signals from an underwater volcano.

We used real infrasound recordings from the IS37 10-element array station in Bardufoss, Norway (Schweitzer, Köhler and Christensen, 2021) as a microbarom analysis test case and data for several months in 2016 are processed using different signal processing approaches. An important aspect is that the recordings, also after filtering in the lower-frequency bands of microbaroms, contain the quasi-continuous microbarom pressure signatures, in combination with many much stronger but transient signals from other sources (including explosions, airports, industry, traffic, etc.), but also additional noise of various kinds (for example, river-related sounds, local turbulence, small-scale and large-scale winds). Ideally, the processing shall be robust enough to not be significantly influenced by other sources, but still be sensitive to variations in the microbarom wavefield signature at the station.

Ultimately, the ambition of the international infrasound research community is to develop operational systems that can use microbarom signals to probe the upper stratosphere and to assimilate that information into atmospheric models to enhance long-term numerical weather prediction. This will require stable and accurate array signal processing pipelines adapted to assess the global microbarom soundscape. Ideally, the current work can provide results that facilitate further research towards microbarom infrasound data assimilation and numerical weather prediction enhancement.

1.2 Key results

Based on components provided by the ObsPy (Krischer et al., 2015) and University of Alaska Geophysics Tools (UAF Geophysics team, 2023) Python repositories, we build a framework and pipeline to process longer streams of infrasound with the intention of robustly estimating the direction-of-arrival of microbaroms.

Microbarom-related results are based on processing recipes applied to several months of data recorded on the IS37 infrasound array at Bardufoss.

The findings are based on in-depth elaborations on the computation of power maps and extracting direction-of-arrival time series and evaluating various aspects and the robustness of the output.

For the characterisation of the direction-of-arrival of the dominating microbarom wavefront for stations like IS37, we suggest that:

- For this kind of quasi-stationary microbarom signals, Capon's method was more sensitive to noise. Still, longer processing time-window lengths can be beneficial, as the variance is reduced.
- The delay-and-sum beamformer was more robust and handled the noisy situation better, as is also expected. Due to its robustness, we can use shorter window lengths while maintaining acceptable stability in the results and a faster processing time.

We note that for most of the analysed time, there is one single spatial region, albeit often large in extent, of microbaroms that is dominating the wavefield and that the need for separating tightly spaced simultaneous directions-of-arrival is somewhat limited.

1.3 Thesis outline

Chapter 1 – Introduction The study and the structure of the thesis is presented.

Chapter 2 – Theory We start out by constructing a short overview of recent works. This is intended to give a perspective of how this study can guide towards tuning an array signal processing recipe (a beamformer) to a specific dataset. We focus on atmospheric infrasound array data, and more precisely a specific type of infrasound, microbaroms, that is continuously generated by ocean swell. A key aspect is to determine the direction-of-arrival using array signal processing methods. From this overview, we establish a foundation of relevant literature for this study, including the establishment of theory applied in future studies.

Chapter 3 – Methods We start out by going through how the data were collected and how the data were pre-processed. From there we go into what kind of processing we used and then how the processed data are displayed. In the final section of this chapter, we investigate how to review the displayed data. This includes objectives such as resolution, sensitivity, and robustness.

Chapter 4 – Results The results are presented on the basis of applying the implemented methods to the data. This is done in two parts. In the first part, the estimations of the backazimuth direction-of-arrival are displayed. In the second part, we look more in detail at the beamformer output power maps implemented in the slowness space, which are key components in estimating the backazimuth. For each of the parts, we study how changing processing lengths affects the result. We visualise the key results and comment on the framework defined in the Methods chapter.

Chapter 5 – Discussion In this chapter, we discuss the results presented in the previous chapter. For example, how does the beamformer with a given window length perform for explaining how the path of a microbaroms changes over time.

Chapter 6 – Conclusions and further work Here, we present conclusions and recommendations in the context of the two analysed beamformers, in particular efficient beamforming of microbarom datasets at the IS37 array at Bardufoss. In addition, suggestions for future work to improve the results are discussed.

1.4 Own contributions

In this study, we have intensively studied the ObsPy Python library and applied it to process infrasound array recordings and study the infrasound soundscape, with a focus on analysing microbaroms. The framework has been adapted and fitted to load, compute, and plot infrasound signal processing output in various aspects.

A focus has been on studying the effect of varying window lengths for Capon's method and the delay-and-sum method when computing microbarom power maps as a function of horizontal slowness.

We have also developed our own frameworks for plotting the signal processing output in slowness space, as well as for visualising the backazimuth direction of the dominating microbarom peak as a function of time.

CHAPTER 2

Theory

In this study, we consider acoustic waves. These are elastic waves, which means that the waves temporarily move air particles locally. The acoustic (or sound) waves we are considering propagate at around 334 m/s at 15 degrees Celsius when on the Earth's surface.

In order to determine the direction of the source we need an array of multiple sensors. The framework for signal processing of such multi-sensor array data is called beamforming, or sometimes also array signal processing. Beamformers are specific algorithms that are applied in the array signal processing.

2.1 Acoustic waves

As a wave passes a position, the particles oscillate around their resting points as they are compressed or rarefied (Rayleigh, 1896; Pierce, 2019). The energy of a sound wave can be divided into two components, potential energy and kinetic energy. In this context, the potential energy is energy related to air compression, and the kinetic energy is energy coming from the air particles' movements and the air's rarefying. (See, e.g. Evers and Haak, 2010, for an infrasound-focused background account of acoustic theory.)

The sound frequency is defined by the number of oscillations per second. The wavelength is the distance between two zero crossings. The relation between frequency (f), wavelength (λ) and speed of sound (c) is given by

$$c = \lambda f. \tag{2.1}$$

The power spectral density shows how the signal power varies with its frequency. This is computed using a Fourier transform.

The sound intensity is the acoustic power and directivity per unit area.

The intensity of a signal decreases with distance and is at the highest in the near-field. Considering the energy of the sound wave, the kinetic energy dominates in the near-field but is in equilibrium in the far-field.

2.2 Infrasound

2.2.1 Definition and sources

We consider infrasound to be within 3.3 mHz to 20 Hz, where the lower limit is what fits within the atmosphere of the Earth. The upper boundary is not audible for humans. Infrasound is generalised into two groups, transient signals and continuous signals. Transient signals are finite in length and short in duration, while idealised continuous signals are infinite and defined for the whole duration. In addition to the two, we find some combinations of them as well.

Typical sources of infrasound are standing ocean waves, which is a near continuous hum. They are in the open sea and interact with coastlines. The source in the ocean can be associated with marine storms, giving us quasi stationary and transitory waves. Transient sources of infrasound have also been detected from severe weather, earthquakes, meteor strikes, and volcanic eruptions. From here, the infrasound can radiate from sources under water, and sometimes from both water and air (Brachet et al., 2010).

In Figure 2.1, we can see two plots, both based on a stream of infrasound, from the OKIF array station, an infrasound array 60 km from Bogoslof Island. The upper plot is a pressure plot of one channel from the stream. At around 22h25 to 22h30, we can see an increase in intensity. This change in intensity is a transient infrasound signal that originates from an eruption of Bogoslif Island, an island with a large submarine stratovolcano, which rises around 1800 m from the seafloor to 100 m above sea level (Miller et al., 1998).

In the lower plot in Figure 2.1, we can see a spectogram, found using the same channel data as in the upper plot. In the spectogram, we can see when the transient signal arrives at the array and also at what frequency range. In addition to this, we can see some higher intensity for lower frequencies around 0.1 to 0.2 Hz. This is due to the constant background of the microbarom wavefield and potentially also from other infrasonic noise contributions. The intensity is higher at lower frequencies, because low frequency waves have low attenuation. The intensity in this plot is the square root of the spectrum.

In Figure 2.2, we can see a plot similar to that in Figure 2.1, but the power spectral density in desibel. Note that the range of the colourbar is wide, and hence more colour contrast in the plot could be achieved by reducing this range.

2.2.2 Infrasound waveguides and the atmosperic structure

In this study, we seek to estimate the direction-of-arrival of microbaroms. For the infrasound station in Bardufoss, northern Norway, where we record the data, these wavefields are in wintertime mostly dominated by microbaroms with origin in the North Atlantic. Along the path from the source regions to the ground-based receiver station, these waves propagate predominantly through a waveguide, which has its upper limit in the stratosphere.

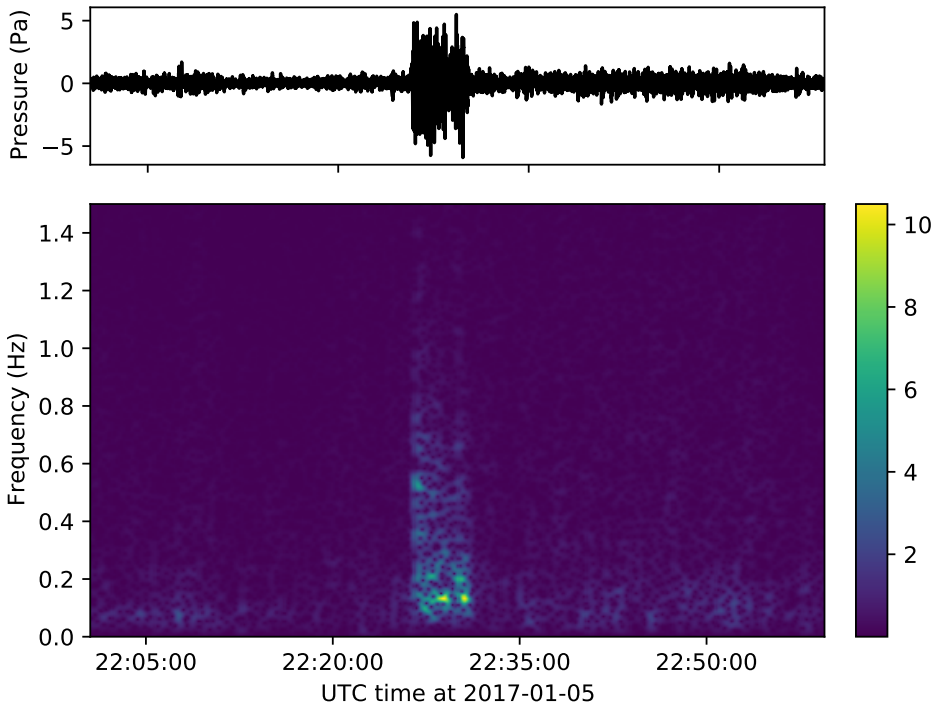

Figure 2.1: OKIF station data display for 5. of January. Top panel: a plot of an unfiltered channel (AV.OKIF.01.HDF) trace. Bottom panel: A spectogram of an unfiltered channel with 0 to 1.4 Hz displayed. Intensity of the spectogram is shown as the square root of the spectogram values.

The stratosphere is at 15 to 50 km altitude (see Figure 2.3). A field of relevance for this study is Sudden Stratospheric Warmings (Baldwin, Ayarzagüena et al., 2021), or SSWs. During such events, the polar eastward jet is slowed down, and its polar cap average zonal wind is reversed from eastward to westward. Furthermore, the temperature in the upper stratosphere can increase by up to 50 degrees. We usually get a downward coupling a few weeks later on the earth surface (in northern Europa) (Butchart, 2022). With the implications of longer periods of dry cold weather (Baldwin and Dunkerton, 2001; Baldwin, Ayarzagüena et al., 2021; Butler et al., 2017).

With the stratospheric winds in mind, we include some illustrations of this in three different time periods of interest, which have different stratospheric vortexes. The first period of interest is on 8 January 2016, shown in Figure 2.5, we can observe that the stratospheric vortex is in a normal state. Concerning the microbaroms of interest, propagating from the North Atlantic Ocean, these signals will get a tailwind.

The second time period of interest, on 3 February 2016, illustrated in Figure 2.6 the stratospheric vortex also has a strong stratospheric vortex, but the direction

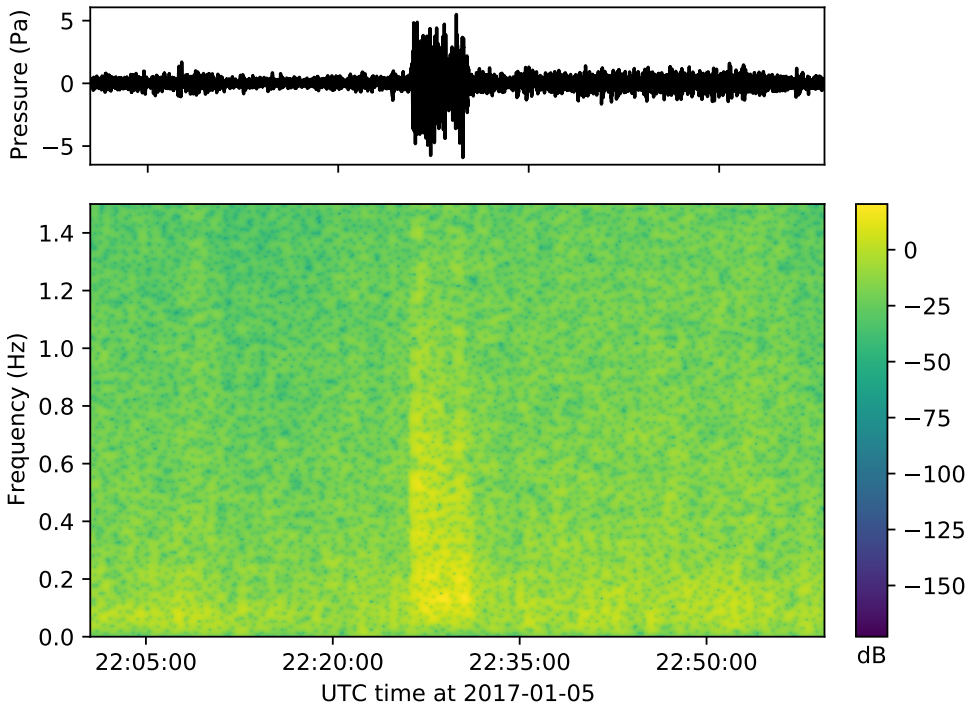

Figure 2.2: Same as in Figure 2.1, the intensity is shown in dB. Colourbar indicates the specific dB levels at a given colour in the spectogram.

of the wind has changed. Subsequently, the North Atlantic microbaroms that propagate towards the IS37 station location in Bardufoss will have a headwind in the stratosphere (consequences illustrated in Figure 2.4).

Considering the third time period of interest, on 6 March 2016, as illustrated in Figure 2.7, the stratospheric vortex has split into two. This happened during a Sudden Stratospheric Warming (Manney and Lawrence, 2016). Looking at the direction of the stratospheric winds, we can see that we get a headwind from the North Atlantic microbarom hotspot to the IS37 station location, similar to in the second period of interest.

In Figure 2.4, we can see an illustration of raytracing, found in Le Pichon, Blanc and Hauchecorne (2009). The figure shows how the infrasound is affected by the winds of the polar vortex. At this time, the polar vortex wind is directed from east to west. In the figure, we can see that the rays on the left side of the middle figure are lower than those on the right side. The rays on the right side of the middle panel are higher, since the headwind pushes the rays upward. On the left-hand side of the middle panel, we see the opposite. Most of the rays are refracted back down to the ground due to the tailwind of the stratospheric polar vortex.

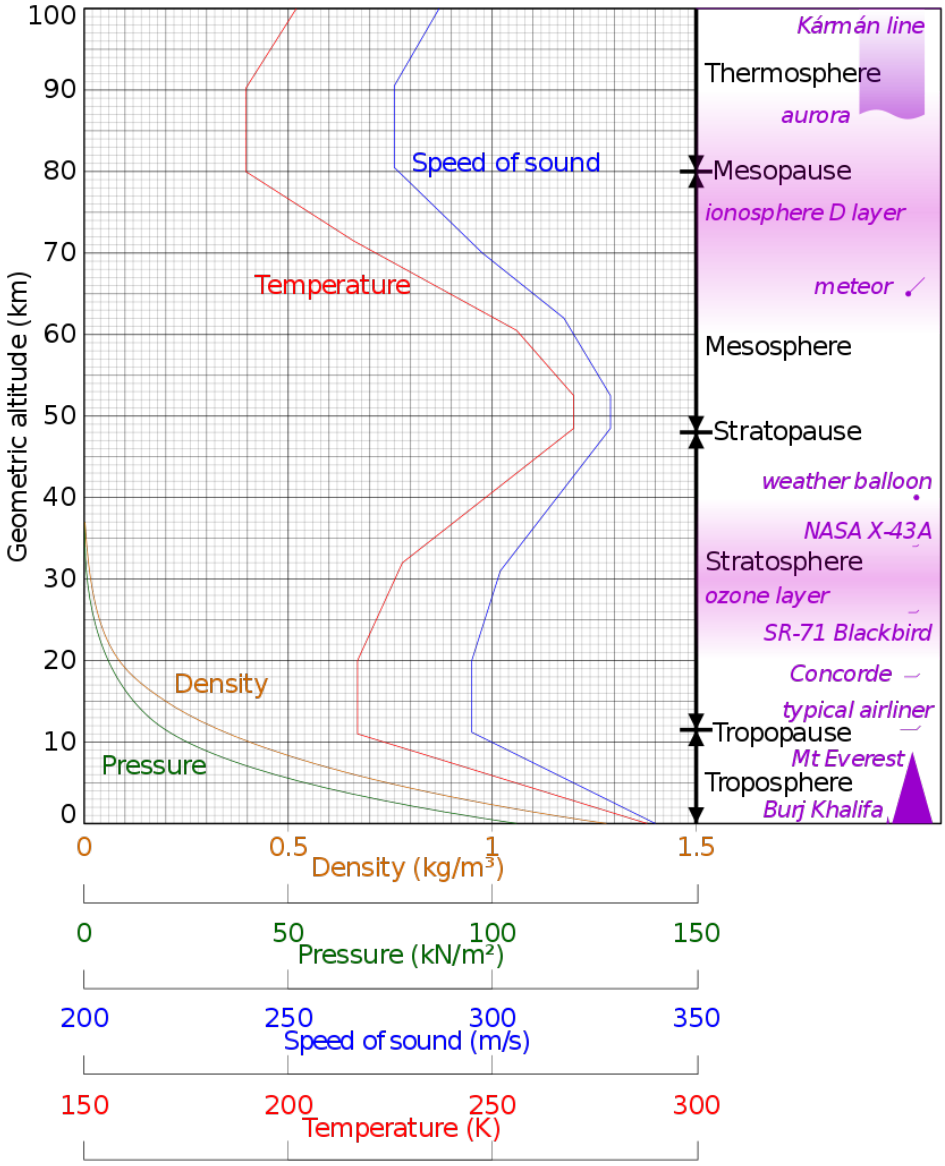

Figure 2.3: An illustration of the standard atmosphere, displaying the stratosphere to be around 15 to 50 km altitude. Note the graph of the speed and sound and temperature, dependent of the elevation. Image source: *Wikipedia page on the US standard atmosphere* (2023).

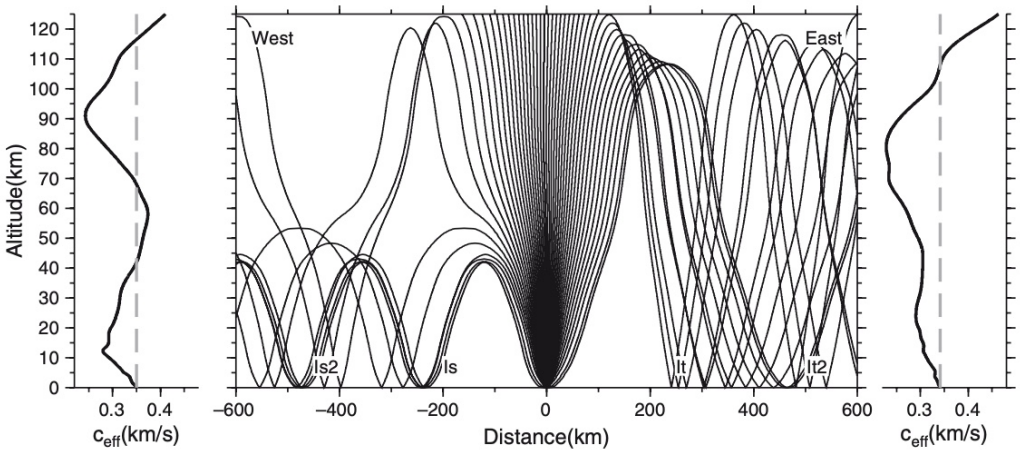

Figure 2.4: The figure illustrates raytracing during summer. The rays are shot from the ground at an angle of 4 degrees, one west and one east, seen in the middle panel. Left and right panel: Illustration of the effective velocities for the various altitudes. Middle panel: Display of raytracing. This image is extracted from Fig. 1.4 of Le Pichon, Blanc and Hauchecorne (2009).

2.2.3 Probing the stratosphere using infrasound

Long-range infrasound propagation is particularly sensitive to winds in the stratosphere (Assink, 2013; Assink et al., 2019), which is an altitude regime where there is a lack of continuous measurements, but which can be important for longer-term weather prediction on the surface, especially in the winter (Tripathi et al., 2016; Domeisen et al., 2020; Butchart, 2022; Kolstad et al., 2022, for example,). Therefore, adequate processing and interpretation of infrasound datasets have the potential to provide data that could improve stratospheric representation in atmospheric models and thus enhance long-range numerical weather prediction (Blanc et al., 2019; Lee et al., 2019). Infrasound wavefields from explosions are typically less complex to exploit than microbarom infrasound and there are some recent proof-of-concept papers that demonstrate the infrasound-based stratospheric probing and data assimilation using data recorded at the IS37 station (Blixt et al., 2019; Vera Rodriguez, Näsholm and Le Pichon, 2020; Amezcua, Näsholm et al., 2020; Amezcua and Barton, 2021).

2.3 Microbaroms

Microbaroms were first introduced Benioff and Gutenberg (1939). They studied atmospheric pressure waves over a temporal period between $3 - 8$ seconds, with an amplitude of $1 - 10$ microbars. They observed that these pressure fluctuations were closely related to microseism activity. Later, they found the relation between microbaroms and marine storms, emphasising on the origin of ocean waves.

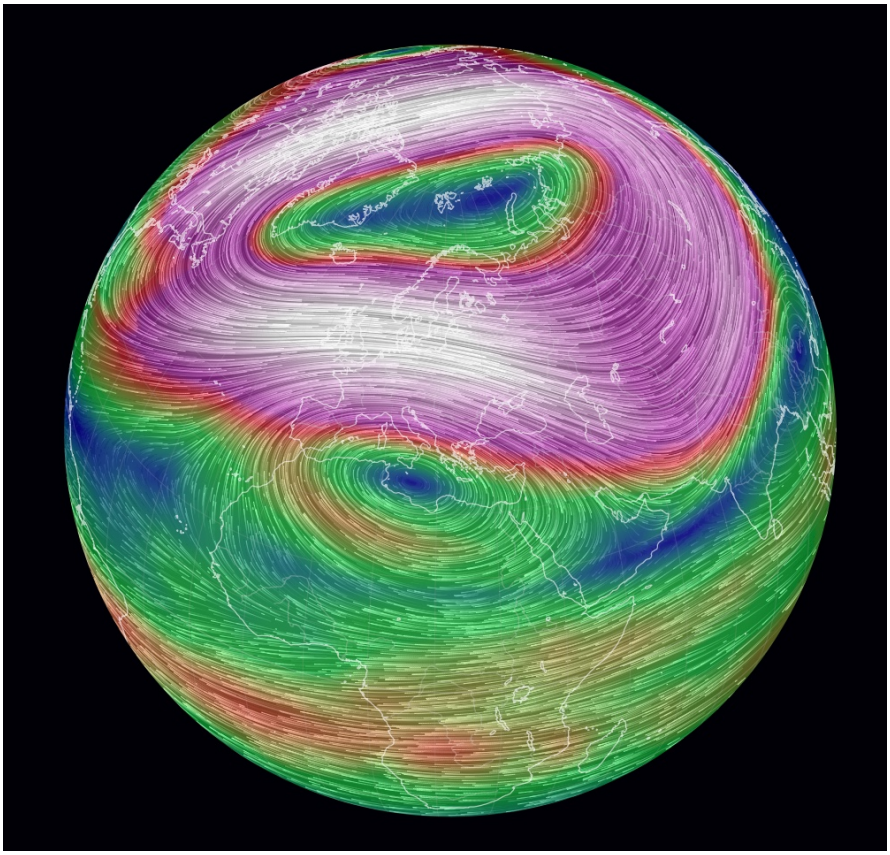

Figure 2.5: An image of earth at 10 hectopascals, at 8 January 2016. This image indicates the stratospheric winds, with the intensities of the winds shown in the colour of the illustration. In this image, we can see that the wind current has god a strong stratospheric vortex. Display generated using: *Earth Nullschool visualization of global weather conditions* (2023).

Later, observations from Benioff and Gutenberg (1939) were confirmed in multiple articles, and the definition became more specific. Microbaroms were defined as an infrasonic signal of a five-second period and are generated by standing sea waves in marine storms. They are in the low-level background in a frequency from 0.02 to 10 Hz. (Brekhovskikh et al., 1973). By considering this, we get wavelengths ranging from 0.15 km for the shorter ones up to 1.5 km for the longer ones. Because microbaroms are low-frequency and the marine storm centre radiates in all directions, microbaroms can be observed globally at infrasonic arrays during all seasons, from sources potentially more than 1000 km from the array (Donn and Posmentier, 1967).

There are studies that explain the diurnal and seasonal variations in the intensity of microbaroms, in relation to the temperature and wind currents in the lower 50 km layer of air. Also, there have been indications of seasonal variations of microbaroms and microseisms, where both have a peak in intensity in the winter. Furthermore, investigations have observed an increase in the intensity of

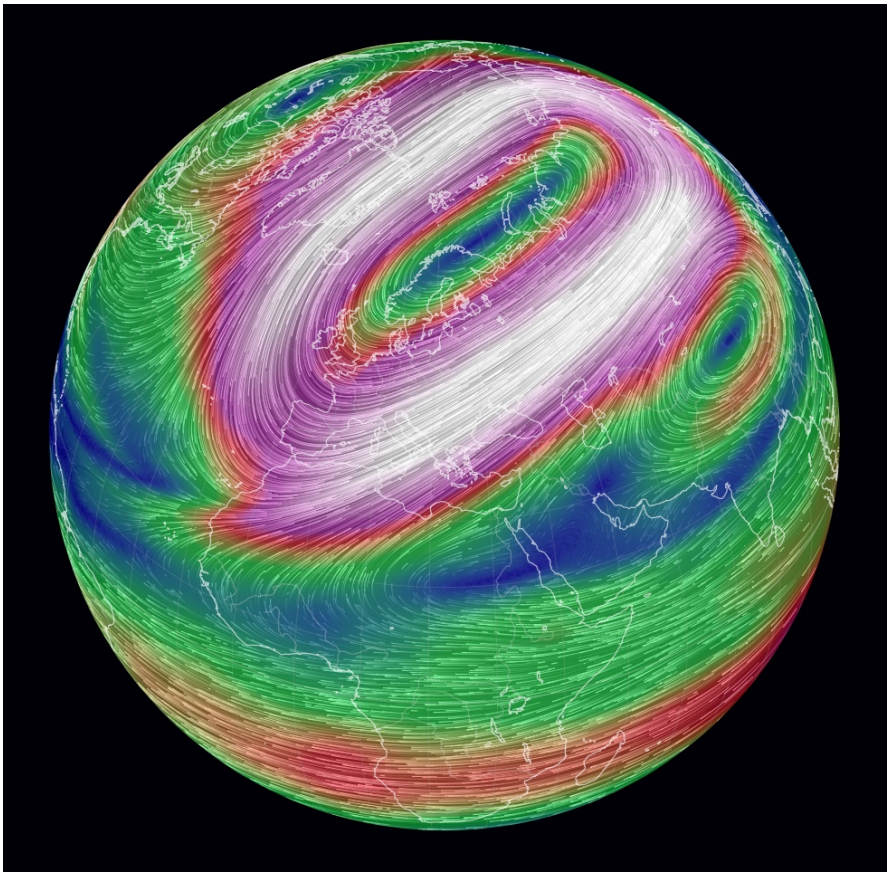

Figure 2.6: Same as in Figure 2.5, but at 3 February 2016 (same time in the Figures, 4.11 and 4.14). Note that the figure has a strong stratospheric vortex, but the direction of the wind has changed. Display generated using: *Earth Nullschool visualization of global weather conditions* (2023) .

microbarom detections at night (Daniels, 1952).

In 1966, Donn and Posmentier found that the spectral character of microbaroms and microseisms is a function of a common generating mechanism, but the variations in amplitude of the microbaroms also depend on the atmospheric conditions along the path (Donn and Posmentier, 1967).

In the 1970s Rind and Donn studied the use of natural infrasound in order to probe the upper atmosphere. They used ambient noise such as microbaroms as a near continuously source to explore. For example, they studied the state of the atmosphere by studying the change in amplitude of ambient noise observations. By studying the typical amplitude variations, they could relate this to the viscous dissipation associated with the reflexion height variation (Rind and Donn, 1975). They also associated the link between unusual microbarom intensities to variations in the stratosphere. By studying these variations, they related this to stratospheric warmings (Rind and Donn, 1978).

Later studies have focused on the radiation, where (Waxler and Gilbert, 2006)

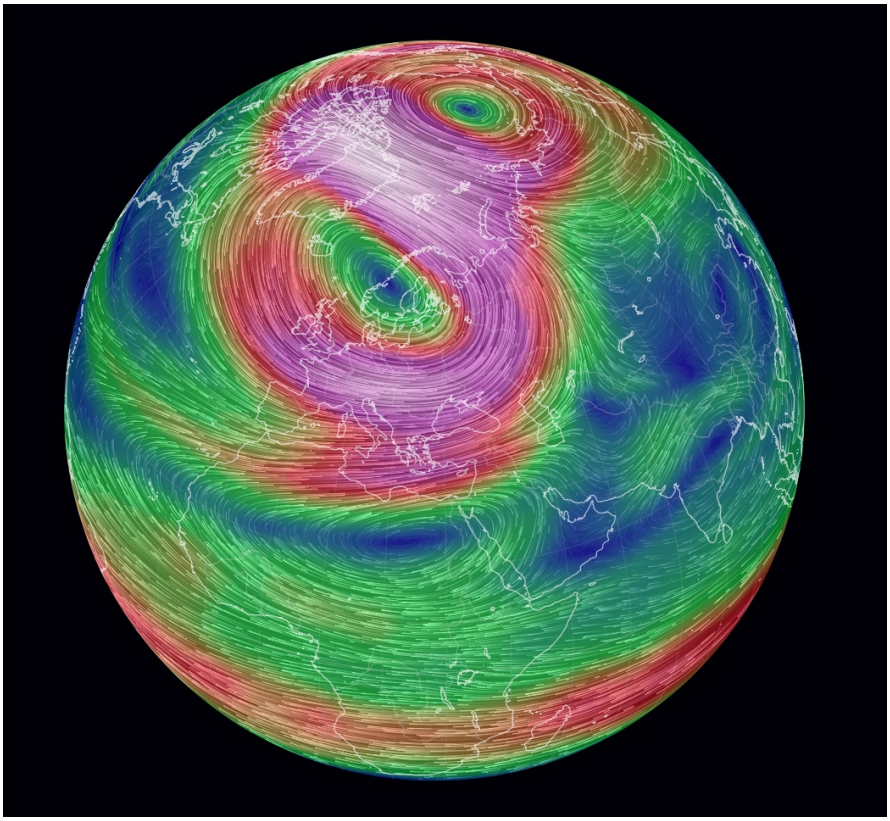

Figure 2.7: Same as in Figure 2.5, but at 6 March 2016. In comparison to the two other figures, we can see a change in wind, two centres in stead of one big, meaning there is a stratospheric vortex split. This happened during a Sudden Stratospheric Warming. Display using: *Earth Nullschool visualization of global weather conditions* (2023).

compared the physical mechanisms and source strengths of radiation into the atmosphere and ocean. Then in 2020 (De Carlo, Hupe et al., 2021) found that microbaroms dominate the coherent infrasound ambient noise measured globally. The monitored microbaroms were used to characterise source activity and probing the properties of the propagating medium, such as the middle atmosphere.

Then, related to the motivation for this study, Smets, Assink and Evers (2019) studied the effects of a stratospheric major warming on the propagation of infrasound. For example, it has been shown that there can be summer-like infrasound signatures in the middle of winter when there is a stratospheric Sudden Stratospheric Warming event. See also Garcés et al. (2004), Le Pichon, Ceranna et al. (2006), Fricke et al. (2014), Landès et al. (2014), De Carlo, Ardhuin and Le Pichon (2020), Ouden et al. (2021), den Ouden, Assink, Smets and Evers (2022), Smirnov et al. (2021) and Vorobeva et al. (2021) for comparably recent papers related to microbarom wavefield characterisation and analyses.

The trends and topics in the more recent studies are the source of motivation for this study. We aim to enhance the stratospheric probing of the atmosphere by

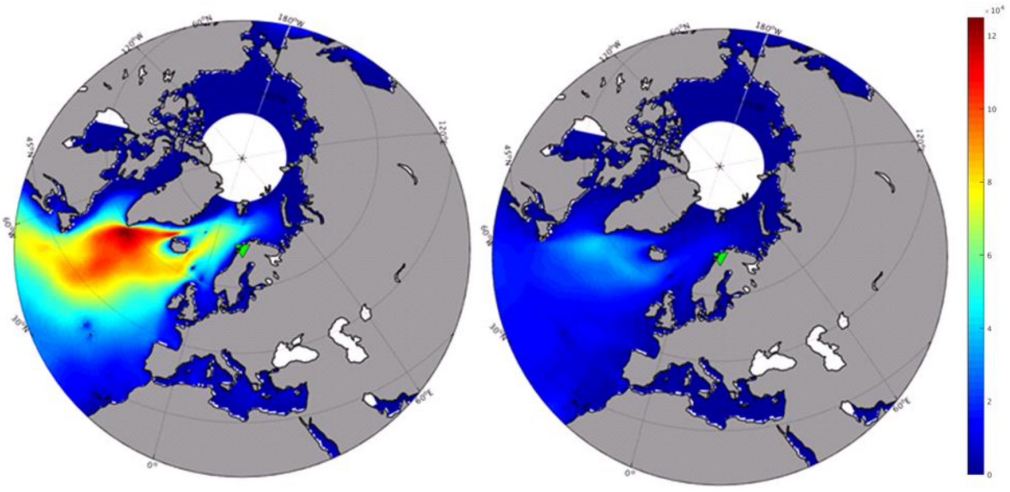

Figure 2.8: Illustration of microbarom sources. The left plot views microbarom sources in $Pa^2m^2s^{-1}$ averaged over January 2016. The right views the same, but is averaged over July 2016. This image is extracted from Fig. 1 of De Carlo, Le Pichon et al. (2018)

optimising the aspects of adopting beamformers to make appropriate microbarom-related processing of streams of array infrasound data.

2.4 Infrasound stations and sensor configuration

The current study focusses on data recorded at the IS37 infrasound station. This is a 10-element ground-based array located in Bardufoss, Norway (69.07 N, 18.61 E), and the station is sometimes also denoted I37NO Fyen, Roth and Larsen (2014).

This station is part of the International Monitoring System (IMS) of the Preparatory Commission for the Comprehensive Nuclear-Test-Ban Treaty Organization (CTBTO) (Christie and Campus, 2009; Brachet et al., 2010) Data access can be granted to third parties and researchers through the Virtual Data Exploitation Centre (vDEC) of the International Data Center[1] (Preparatory Commission for the Comprehensive Nuclear-Test-Ban Treaty Organization, The Provisional Technical Secretariat, 2011).

In Figure 2.11 we have plotted the location of the IS37 array station on a map, and the design of the array has been plotted in Figure 2.12

2.5 Filtering for microbaroms

Given that the interest of this study is infrasound, within the 0.1 to 0.5 Hz band. Then we need to filter our dataset that contains frequencies from 0.01 to 20 Hz,

[1]Direct link: https://www.ctbto.org/specials/vdec/

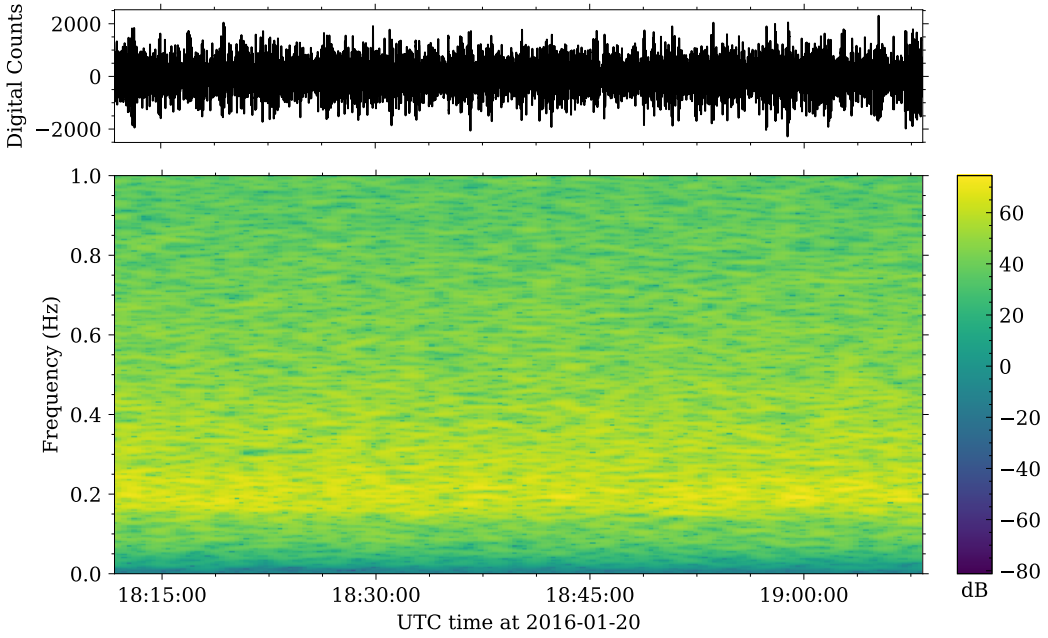

Figure 2.9: Plot of data with a highpass filter with corner frequency at 0.01 Hz was applied. The upper plot shows the pressure plot in time. The lower panel shows the spectrogram of the same trace.

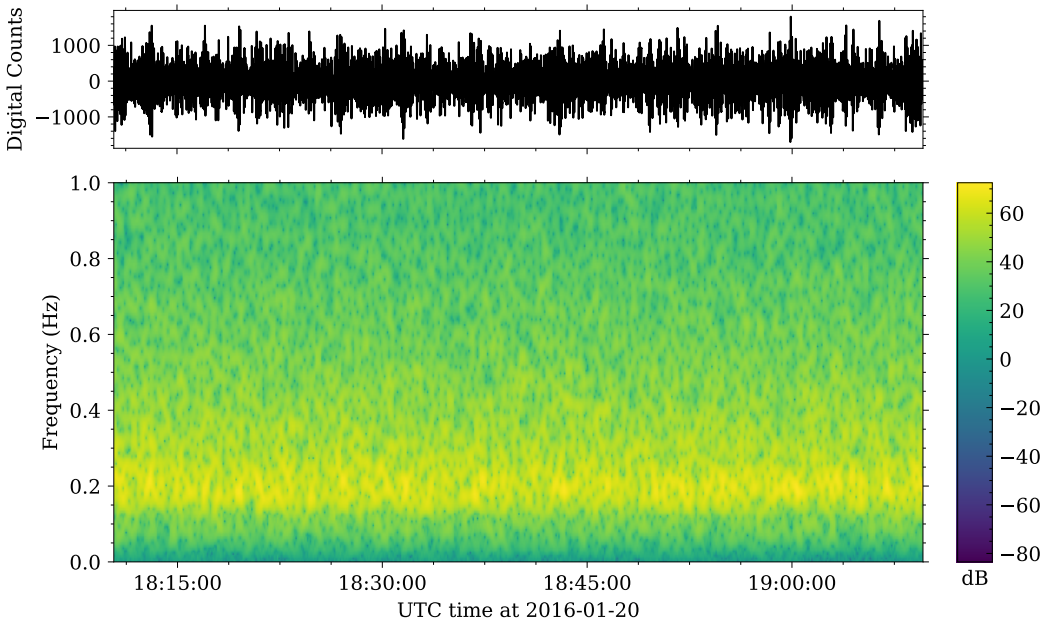

Figure 2.10: Plot of stream with highpass filter of 0.01 applied. The stream has been beamformed towards -100 degrees and 340 m/s apparent velocity, which is a known near continuous source of microbaroms. The upper plot shows the pressure plot in time. The lower shows the spectrogram of the beamformed data.

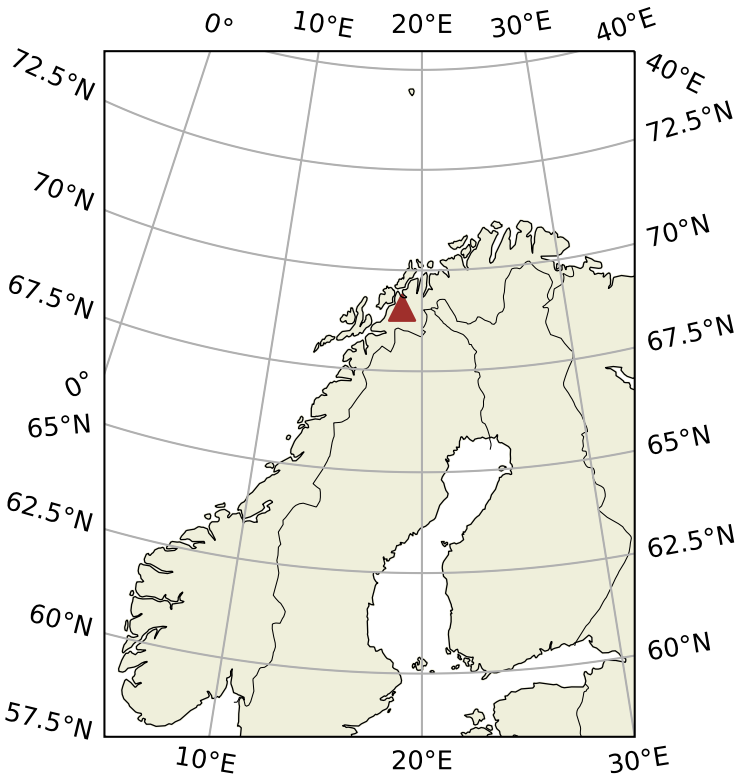

Figure 2.11: Geographical location of the IS37 array (red triangle), located at Bardufoss, Norway.

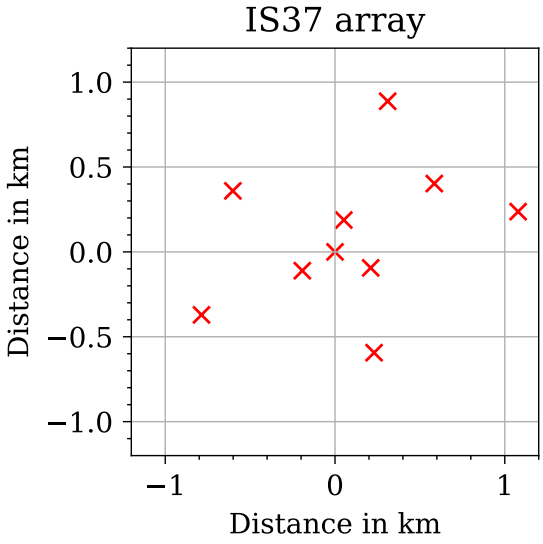

Figure 2.12: The IS37 array map with red crosses indicating each sensor in space. The figure shows the design of the infrasound array.

with a sampling rate of 20 samples per second. We get the desired frequency range by using a passband filter. The filter is implemented using preprocessing techniques such as detrending and tapering. Preprocessing is necessary to avoid artefacts in the stream of data after filtering.

First, we consider one trace of each station and start reviewing the data, before we introduce techniques in order to investigate our data more specifically in spatial coordinates.

Frequency Spectrums

Considering the dataset from the IS37 infrasound station, we need to assess the incoming waves so that we can tell in simple terms how the stream is built up. That is, of what frequency, intensity, duration and when are the incoming waves. When studying strong transient waves, this usually shows up in a pressure plot of the stream. By studying the fast Fourier transform (FFT) from the SciPy library (Virtanen et al., 2020), we study the frequency spectrum of the magnitude of the stream, dependent on frequency. The FFT algorithm implements the discrete Fourier transform in a computationally efficient manner (see, for example, Rao and Swamy, 2018, Chapter 4), defined to be

$$y[k] = \sum_{m=0}^{M-1} \exp\left(-2\pi j \frac{km}{M}\right) x[m], \tag{2.2}$$

where $y[k]$ is the intensity of a discrete frequency sample, where the sample is given by k, $x[m]$ is the stream and M length of the stream .

By considering the frequency spectrum, we can consider the entire length of a stream in one plot. This plot makes an overview of the magnitude of the various frequencies. Microbaroms are usually dominant over other sources at around 0.2 Hz. Providing an indication of whether there are microbaroms present.

In Figure 2.13, we have a frequency spectrum calculated using data from the IS37 station array. The data have a duration of 1 hour from 20 January 18h10 to 19h10. The frequency spectrum displays the magnitude of each frequency ranging from 0 to 10 Hz. It is clear that the most intense signal is around 0 to 1 Hz, so we consider this in the Figures 2.14 and 2.15.

In Figure 2.14 we see that the dominant incoming signals are around 0.2 Hz. Note that if we did not apply the highpass filter, then there would be a higher peak in frequencies around 0 and 0.1 Hz.

Figures 2.14 and 2.15 should be considered in relation to each other. We are considering the same dataset, from the IS37 array station, but in Figure 2.15, we have used all channels in the array, directed towards -100 degrees with an apparent velocity of 340 m/s using beamforming. We can note that the plots are similar, but there is some suppression outside of the peak intensities around 0.2 Hz.

In spectograms, we can study the magnitude of different frequencies over time. Such plots makes it easier to tell microbaroms apart from transient infrasound. It can also give some idea if the microbaroms has deviated from their normal paths,

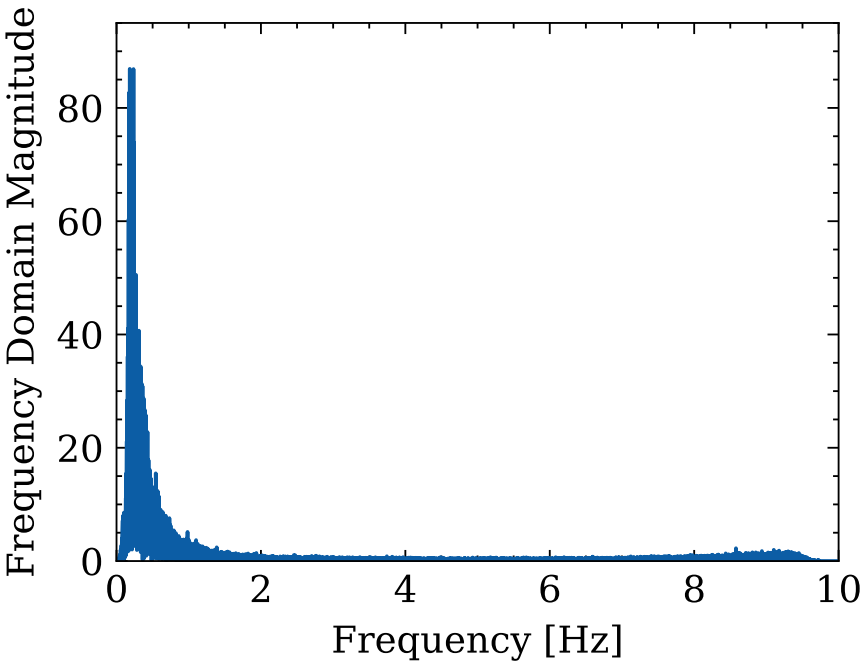

Figure 2.13: IS37 station data, plot of frequency spectrum using Fast Fourier Transform (FFT) considering an hour of channel data from 20 January 2017 from 18h10 to 19h10. In this plot a highpass filter of 0.1 Hz is applied. Note that we consider frequencies from 0.1 to 10 Hz.

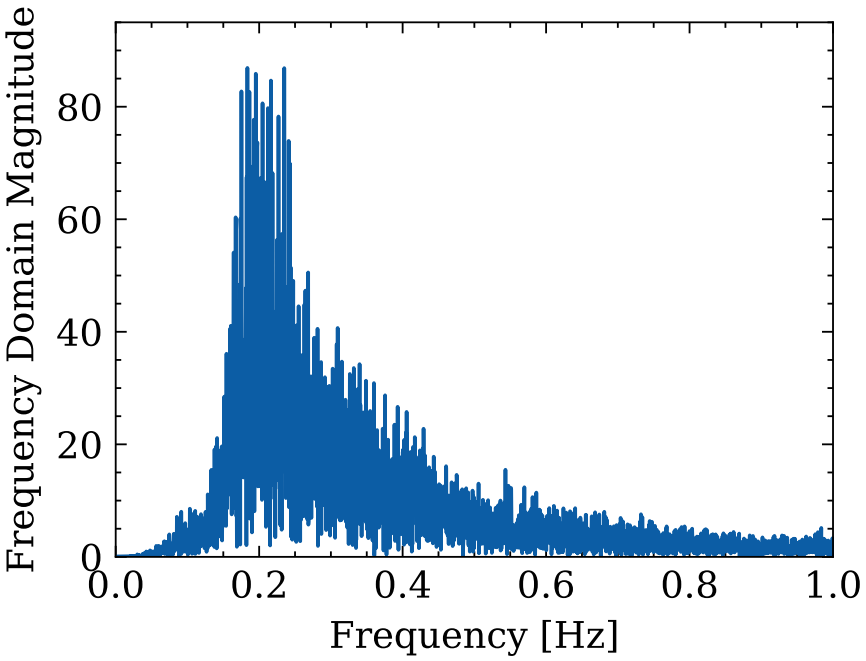

Figure 2.14: Same as in Figure 2.13, but we are considering the FFT from 0.1 to 1 Hz.

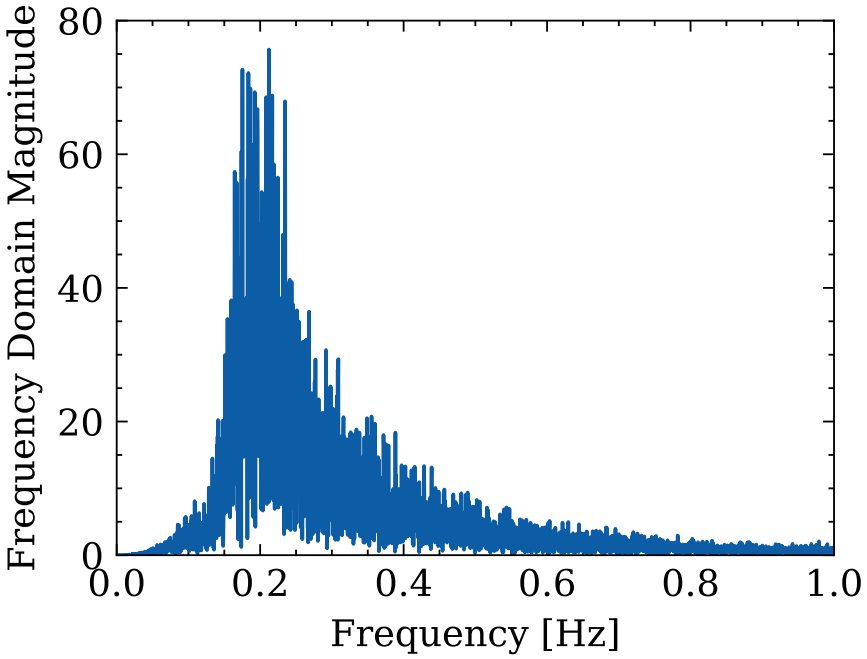

Figure 2.15: Same as in Figure 2.14, but we consider the entire stream of the array data and steer it towards the microbaroms at -100 degrees with an apparent velocity of 340 m/s.

although there are often other incoming microbaroms from other sources, hence this is not an ideal indication. More importantly, the spectogram can view other strong infrasound that could possibly affect our next processing steps. For example, when we are computing power maps, how long window lengths are needed to make the microbaroms the dominant source?

Considering spectrograms, as shown in Figure 2.10, we found that the signals below 0.1 Hz are strong and would for the most part be the dominant incoming signal over the microbarom signals. Therefore, filtering out these signals is necessary when calculating the direction-of-arrival of the microbaroms. Compared to the transient signal in Figure 2.2 from the Bogoslof volcano, the signal would be the dominant signal in an unfiltered trace.

2.6 Beamformers

2.6.1 Array signal processing

Array signal processing involves a consolidated processing of time series recorded on several sensors located at different locations in space (van Trees, 2004; Johnson and Dudgeon, 1992; Krim and Viberg, 1996; Grythe, 2015). In other words, the beamforming algorithms are applied to focus the array to a certain direction in the far-field (or location in the near-field). The sensor signals are delayed and then

summed (or stacked) to form a single trace that ideally probes waves impinging the array from a single direction.

Arrays of sensors can be used to determine properties of propagating waves. When using radars, arrays of sensors can be used to represent objects in spatial coordinates. This can be beneficial, for example, in vehicles where there is no clear vision, in lack of day light, or in bad weather.

Arrays of sensors are also used in seismic applications in order to determine the vector velocity of propagating seismic waves and to understand whether an incoming signal is from, for example, an earthquake or from an underground explosion (Schweitzer, Fyen et al., 2012; Rost and Thomas, 2002; Rost and Thomas, 2009).

In this project, we are going to study data from an infrasound station using array signal processing to detect certain incoming microbaroms that mainly originate from the North Atlantic Ocean. Our object of study is to being able to separate these waves from other infrasound (for example, due to explosions) and microbaroms from other incoming directions and to provide reliable time series of direction-of-arrival for the dominating microbarom wavefront. Our approach to this is to make a 2D plot of incoming waves dependent of the incoming directions, velocity and intensity. We better represent the incoming waves by increasing the signal-to-noise ratio (SNR). A higher SNR is achieved by repetitively steering the array signal beam in various directions, using a beamformer.

Beamformers are usually divided up into conventional and adaptive methods. The conventional methods are beamformers, where the steering of the array is done independently of the stream of data. While the adaptive methods are dependent of the stream of data. The adaptive methods usually yield a higher resolution or better sidelobe suppression, both resulting in a higher SNR.

2.6.2 Delay-and-sum (DAS) beamforming

The elaborations in the current section follow to a great extent the lines of Grythe (2015). The first beamformer we will introduce is called delay-and-sum (DAS). This beamformer is used to align the incoming data from each sensor (sensor trace) and apply weights to each individual sensor, depending on the direction for which the array is steered. The steering of the array is used to maximise the sensitivity of the array in the desired direction.

The aligning of the traces is done by applying time delays or similarly using phase shifts. The addition weights add gain or loss to each of the traces and will result in gain or suppression of the sidelobes. Suppression of the sidelobes, usually cause a wider main lobe, meaning worse resolution.

In this section, we introduce how time delays are added to each sensor. In our array, we consider 10 sensors in space, $\vec{x}_m = [x_m, y_m, z_m]$, where the data sampled is $y_m(t) = f(\vec{x}_m, t)$. We set the time delays to δ_m and the amplitude weights to w_m.

As described above, we introduce the delay-and-sum beamformer output:

$$z(t) = \frac{1}{M} \sum_{m=0}^{M-1} w_m y_m(t - \Delta_m), \tag{2.3}$$

where Δ_m are applied time delays and w_m are the sensor weights.

From here, we would like to use a set of time delays corresponding to different directions in space and then calculate the beamformer for each individual direction. Comparing the beamformer output power as a function of direction-of-arrival, we can tell where the most significant source is coming from, or what the spatial spectrum of the full wavefield is.

We can also interpolate the different numbers of output powers from all the scanning points, assigning each point in space a colour corresponding value of power, adding up to an acoustic image, called a power map. Defining each of the points in space to be listening points, $x_s = [x_s, y_s, z_s]$, and the set of delays, Δ_m needed to steer the beam towards a point in space is calculated as

$$\Delta_m = \frac{|\vec{x}_s - \vec{x}_m|}{c} = \frac{\sqrt{(x_s - x_m)^2 + (y_s - y_m)^2 + (z_s - z_m)^2}}{c}, \tag{2.4}$$

where c is the speed of sound.

We can also scan for specific angles, instead of points in the plane. The implementation with a delay applied for each of the sensor traces is as follows.

$$y_m(t) = e^{j(\omega j - \vec{k} \cdot \vec{x}_m)}, \tag{2.5}$$

where $\omega = 2\pi f$ is and f is the frequency of the input signal. $\vec{k}$ is the wavenumber vector or propagation vector, which gives the magnitude and direction-of-arrival of the incident plane wave. We can write the beamformer in another way, in terms of phase shifts:

$$z(t) = \frac{1}{M} \sum_{m=1}^{M} w_m \cdot y_m(t) \cdot e^{-j\omega\Delta_m}. \tag{2.6}$$

Then, by writing the phase delays in the received signal vector, $\mathbf{Y} = y_m(t) \cdot e^{-j\omega\Delta_m}$, we can write the beamformer in vector notation:

$$\mathbf{z} = \mathbf{w}^H \mathbf{Y}, \tag{2.7}$$

where $\mathbf{Y}$ is the vector of the received signal with the phase delays applied and $\mathbf{w}^H$ is the complex conjugate transpose of the weight vector.

Using the vector notation and assuming that the array is steered in the desired direction, we can calculate the power of the output signal:

$$P(z) = E\{|z|^2\} = \mathbf{w}^H R \mathbf{w}, \tag{2.8}$$

where $\mathbf{R} = \mathbf{E}\{\mathbf{Y}\mathbf{Y}^H\}$ is the correlation matrix of the incoming signal.

If we apply phase delays, $e^{-j\omega\Delta_m}$, to each of the sensors, we get a steering vector, $\mathbf{e}$. Applying the steering vector to the sensor data and then measuring the

output power, we get the steered response. Meaning the measure of output power of a scanning angle in the frequency domain. This measure is computed as follows:

$$z(t) = \frac{1}{M} \sum_{m=1}^{M} w_m e^{i\omega(t-\Delta-s_0 \cdot r_m)}. \tag{2.9}$$

2.6.3 Power spectral density using delay-and-sum

After we have computed the beamformer for the array, we would like to find the power for the signal, for the specific beamformed data, with a given steering and gain. Further following (Grythe, 2015), we see that this is done by using a correlation matrix of the beamformed signal and its steering vector, $\mathbf{e}$.

Taking into account the beamformed data, $\mathbf{Y}$, we find the correlation matrix of the data, $\mathbf{R} = \mathbf{E}\{\mathbf{Y}\mathbf{Y}^{\mathbf{H}}\}$, where H denotes the complex conjugate transpose. The steering vector $\mathbf{e}$ is the phase delays associated with each of the individual sensors, $e^{-j\omega\Delta_m}$.

As the steering vector, $\mathbf{e}$ defined where the beam is steered, we denote the output power in the frequency domain, the steered response. Taking the power output in the frequency domain as a function of $\mathbf{e}$, we get the power spectral density, defined as

$$P(\mathbf{e}) = \mathbf{e}^H \mathbf{R} \mathbf{e}. \tag{2.10}$$

After one direction has been computed, the array can be steered in another direction. Then the power can be calculated in the same manner. Iteratively, we can do this to find a grid from 0 to 360, a power map that consists of the output power dependent on the steering direction.

A power map can be displayed in the slowness space (introduced later in Subsection 3.5.3), called a slowness plot. This will provide a representation of the incoming wavefield, indicating the direction and velocity of a dominant signal/wave.

When computing a power map, we consider a certain time frame of the dataset. Considering multiple such time frames, we can get an overview of the incoming wavefields over time. For example, we can consider the backazimuth that is given by the incoming direction of the dominant signal. This gives us an overview of where the dominant signal comes from and when it deviates. If we consider shorter time frames, transient signals could potentially become the dominant incoming wave.

2.6.4 Capon's method

The delay-and-sum beamformer is a method where the delay and weighting of each sensor element are set based on a pre-set model. In infrasound processing, typically all elements are given the same amplitude weight, and the time delays are given by the assumption that there is a far-field plane wave impinging the sensor array.

On the contrary, in adaptive beamforming, the properties of the recorded data are adaptively exploited to enhance the array signal processing. In this study we apply the Capon's method (also denoted the Minimum-Variance beamformer, or the Minimum-Power beamformer) (Capon, 1969; van Trees, 2004). This is an adaptive beamformer, which means that information from the incoming signal is used when finding the appropriate delays and weights to each of the elements. This information can be considered by evaluating the correlation matrix of a given window length of the incoming stream (Krim and Viberg, 1996).

The reminder of the current section continues to follow to a great extent the lines of Grythe (2015). The philosophy behind Capon's method and its goal is to solve a minimisation problem, that is, to minimise the power or variance of the power output, $P(z)$, subject to $\mathbf{w}^H\mathbf{e} = 1$. The weights of the minimisation problem are given as

$$\mathbf{w} = \frac{\mathbf{R}^{-1}\mathbf{e}}{\mathbf{e}\mathbf{R}^{-1}\mathbf{e}}. \tag{2.11}$$

Note that the weights depend on both the correlation matrix $\mathbf{R}$ and the steering vector $\mathbf{e}$. It follows that the optimal element weights are found for every direction the array is steered towards.

By evaluating theoretical beampatterns, we see that, compared to delay-and-sum, Capon's method can minimise the possibility of distorted incoming signals by signals arriving at incidence angles corresponding to the location of sidelobes of the array. This is because the minimisation condition forces the beampattern to have low energy at arriving angles corresponding to other sources while obtaining maximum energy in our listening direction.

The power of Capon's method can be computed as

$$P(\mathbf{e}) = \frac{1}{\mathbf{e}^H\mathbf{R}^{-}1\mathbf{e}}. \tag{2.12}$$

Where $\mathbf{R}$ indicates the covariance matrix and its steering vector $\mathbf{e}$.

From a theoretical point of view, Capon's method has a higher resolution than the delay-and-sum method. In this study we are going to study whether this translates to infrasound, and more specifically near-continuous ocean waves (microbaroms).

Diagonal loading with Capon's method

There are several tweaks to Capon's method that can have benefits under different conditions. For example, we have IAS-Capon Gal et al. (2014), CLEAN den Ouden, Assink, Smets, Shani-Kadmiel et al. (2020b) and diagonal loading of Capon's method Synnevag, Austeng and Holm (2007).

When using Capon's method, we need an accurate correlation matrix. Using Capon's method can in practise lead to poor performance due to coherent noise. The ideal scenario would be a wavefield with one strong signal and noise that is incoherent.

To compensate for the inaccuracy in the correlation matrix, the other coherent signals need to be suppressed. Signals can be suppressed by adding spatially white noise to the wavefield. This corresponds to adding a constant to the diagonal elements in the correlation matrix, before adding the weights to the elements. This step of adding the constant to the diagonal is called diagonal loading (Synnevag, Austeng and Holm, 2007).

From this, the dilemma is the following. How much diagonal loading is needed? We set ϵ as the amount needed for the diagonal loading. ϵ is found by setting a predetermined constant value λ applied to the trace operator $\mathrm{tr}\{\cdot\}$:

$$\epsilon = \lambda \cdot tr\{\tilde{\mathbf{R}}(t)\}\mathbf{I}. \tag{2.13}$$

Note that a well-chosen diagonal element, λ, is found by trial and error.

We apply the diagonal loading, first by multiplying the diagonal loading element, λ, to the identity matrix, $\mathbf{I}$, then add this to the correlation matrix. Together we consider this to be $\tilde{\mathbf{R}}$. From here we calculate the beamformer in the same way as computing Capon's method, by replazing $\mathbf{R}$ with $\tilde{\mathbf{R}}$.

Our minimisation problem becomes

$$\min \tilde{\omega}^{\mathbf{H}}\tilde{\mathbf{R}}\tilde{\omega}, \tag{2.14}$$

$$\text{so that } \tilde{\omega}^{\mathbf{H}}\mathbf{s} = 1. \tag{2.15}$$

$\mathbf{s}$ is considered to be the directed vector with a normalizing factor.

Using the Lagranges multiplier approach, we find the weighted vector $\tilde{\omega}$ solution

$$\tilde{\omega} = \frac{\tilde{\mathbf{R}}^{-\mathbf{1}}\mathbf{s}}{\mathbf{s}^{\mathbf{H}}\tilde{\mathbf{R}}^{-\mathbf{1}}\mathbf{s}}. \tag{2.16}$$

When more noise is added, meaning that the constant, λ, has a higher value, then we get a higher constraint on the sidelobe levels in the direction of no interfering signals. It can also be shown, see Synnevag, Austeng and Holm (2007, Section 2C), that as the diagonal loading increases, the Capon beamformer solution for the weights approaches a uniformly weighted case.

The method goes towards the delay-and-sum method with uniform shading. This is because the correlation matrix is proportional to the identity matrix. $R(t) = \sigma_n^2 I$, where σ_n^2 is the variance of the noise. From equation 2.16, this implies:

$$\tilde{\omega} = \frac{\tilde{\mathbf{R}}^{-\mathbf{1}}\mathbf{s}}{\mathbf{s}^{\mathbf{H}}\tilde{\mathbf{R}}^{-\mathbf{1}}\mathbf{s}} = \frac{(\sigma_n^2\mathbf{I})^{-1}\mathbf{s}}{\mathbf{s}^{\mathbf{H}}(\sigma_n^2\mathbf{I})^{-1}\mathbf{s}} = \frac{\mathbf{s}}{\mathbf{s}^{H}\mathbf{s}} = \frac{1}{M}\mathbf{s}. \tag{2.17}$$

Considering the result, Capon's method gives the same power estimates as the delay-and-sum beamformer with uniform weights.

2.7 Beamforming example: a transient signal in an ambient microbarom background

To demonstrate that a transient signal from an explosion can co-exist with the ambient microbarom background, we look at a mining blast event from Aitik, Gällivare, northern Sweden. The Aitik mine is an open-pit mine where there regularly are explosions set off as part of the operation. For more information on infrasound-based studies using these data, see Smets, Evers et al. (2015), Gibbons, Kværna and Näsholm (2019) and Gibbons, Asming et al. (2015).

The event we look at here was characterised by the International Monitoring Center of the CTBTO and the seismic and infrasound arrivals are available in its Late Event (LEB) bulletin, see Table 2.1 for further info on this specific event. (See, for example, the introduction in Le Bras et al., 2021, for an overivew of the CTBT bulletin products and the methods applied to produce them.).

We note that the backazimuth direction at the IS37 station was found to be 148 degrees in this reviewed bulletin.

Figure 2.16 shows a stream from the IS37 array station in Bardufoss on 19 January 2016. The data were beamformed towards 148 degrees with an apparent velocity of 340 m/s, a blast from the Aitik mine in northern Sweden. The figure is a collection of two plots; the upper panel is a pressure plot of the beamformed data. The lower panel is a spectogram from the same beamformed data, with the intensities of the wavefield shown in decibels. Before beamforming, a highpass filter of 0.5 Hz had been applied in order to cancel out strong microbaroms, and even stronger infrasound noise below 0.1 Hz. In the spectogram, we can see the transient signal from the defined highpass filter, up to around 8 Hz. In the pressure plot, it is also easy to note when the transient signal arrives at the IS37 array.

Figure 2.17 shows the same stream of data from the IS37 array station. The data have been beamformed in the same way as in 2.16, but the applied high pass filter is set to 0.1 Hz. Therefore, we have included the microbaroms in the data. Considering the figure, we can still see some signature in the pressure plot, but it would be hard to define, without knowing the time of arrival. In terms of the spectogram, it is still easy to define the incoming transient signal from the mines, as it is the dominant signal in the range of 1 to 5 Hz.

To check the effect of beamforming, in Figure 2.18 chosen to steer the array towards -100 degrees with a velocity of 340 m/s. Otherwise, the data displayed are the same as in 2.17, with the same highpass filter and the same data stream from the IS37 array station. Illustrating the effect of beamforming another direction, we can see in the pressure plot that it is not possible to tell the transient signal apart from the other microbarom signals. In the spectrogram, there is still some signature of the transient signal, from around 1 to 4 Hz, but at a low intensity, compared to the spectogram in 2.17. For later analysis, this gives an idea of how the intensity of a transient signal is suppressed and its magnitude, compared to the strong incoming microbaroms from the North Atlantic Ocean, at a normal strong stratospheric vortex (see Figure 2.5).

Table 2.1: The infrasound and seismic arrivals and event info of the Aitik mining explosion on 19 January 2016 at 18h01, as provided in the IMS LEB bulletin (see, for example, Willemann, 2009, for a reference on the data format used in this bulletin).

```
EVENT  12775801 SWEDEN
Date    Time     Err  RMS Latitude Longitude  Smaj  Smin  Az Depth  Err Ndef Nsta Gap  mdist  Mdist Qual   Author   OrigID
2016/01/19 18:01:48.64   1.00  0.87  67.0539 21.2919  18.1   8.3 108   0.0f    8    4 169   2.94 7.72 m i uk IDC_LEB 12785472

Magnitude  Err Nsta Author      OrigID
ML     2.0 0.1    4 IDC_LEB   12785472
mbtmp  2.9 0.1    4 IDC_LEB   12785472

Sta     Dist  EvAz Phase     Time          TRes  Azim AzRes   Slow  SRes Def   SNR      Amp   Per Qual Magnitude    ArrID
I37NO   2.27 334.8 I       18:17:49.274 101.8 148.0  -4.3  330.5 -53.4 ___   5.3      0.1  0.60 a__              111030623
ARCES   2.94  30.2 Pn      18:02:36.225  -0.7 210.7   -3.4   13.5  -0.3 TA_  78.8      0.5  0.33 a__ ML      2.4 111029951
                                                                                      1.2  0.26     mbtmp  2.6
ARCES   2.94  30.2 Sn      18:03:14.730   1.9 210.8   -3.4   21.0  -3.7 TA_  10.0      0.6  0.33 a__              111029953
FINES   6.00 157.5 Pn      18:03:19.100   0.0 342.5    0.8   12.4  -1.3 TA_   5.2      0.1  0.33 a__ ML      2.1 111029963
                                                                                      1.0  0.65     mbtmp  3.0
FINES   6.00 157.5 Sn      18:04:27.325  -0.1 332.6   -9.1   26.6   1.9 T__   1.7      0.2  0.33 ___              111096821
FINES   6.00 157.5 Lg      18:04:57.975   0.7 342.5    0.7   30.5  -1.3 TA_   1.8      0.3  0.33 ___              111096822
NOA     7.47 220.9 Pn      18:03:37.200  -0.1  30.8   -1.0   10.4  -3.3 TA_   1.4      0.0  0.33 ___ ML      1.8 111096819
                                                                                      0.5  0.72     mbtmp  2.8
HFS     7.72 209.5 Pn      18:03:39.821  -0.4   6.7  -15.9   13.5  -0.2 T__   1.4      0.1  0.33 ___ ML      1.9 111096816
                                                                                      1.0  0.70     mbtmp  3.1
HFS     7.72 209.5 Sn      18:05:06.332   1.1  31.2    8.5   25.3   0.7 T__   2.0      0.1  0.33 ___              111102499
```

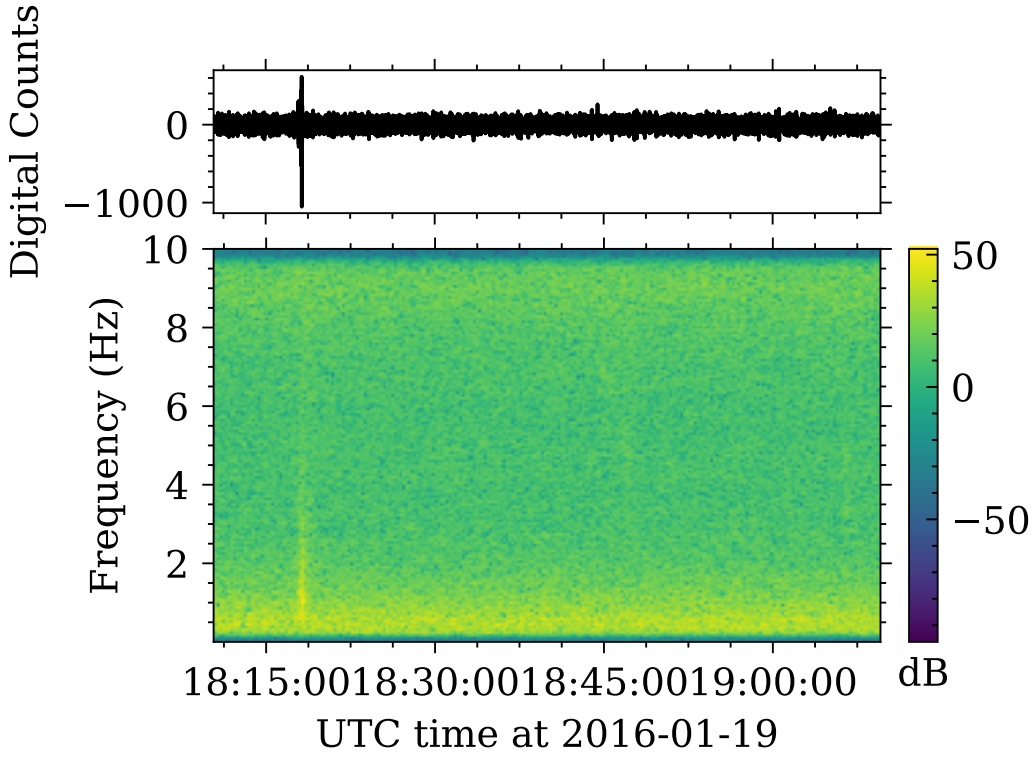

Figure 2.16: Data display of beamformed data, from the IS37 infrasound array station in Bardufoss. The data we consider is from 19 January 2016 from 18h10 to 18h10, containing a transient signal from the Aitik mine in nothern Sweden. The data has been beamformed towards the Aitik mine at 148 degrees at a apparent velocity at 340 m/s. The upper panel shows a pressure plot of the beamformed data, with a highpass filter at 0.5 Hz. The lower panel shows a spectogram in desibel, of the same beamformed data.

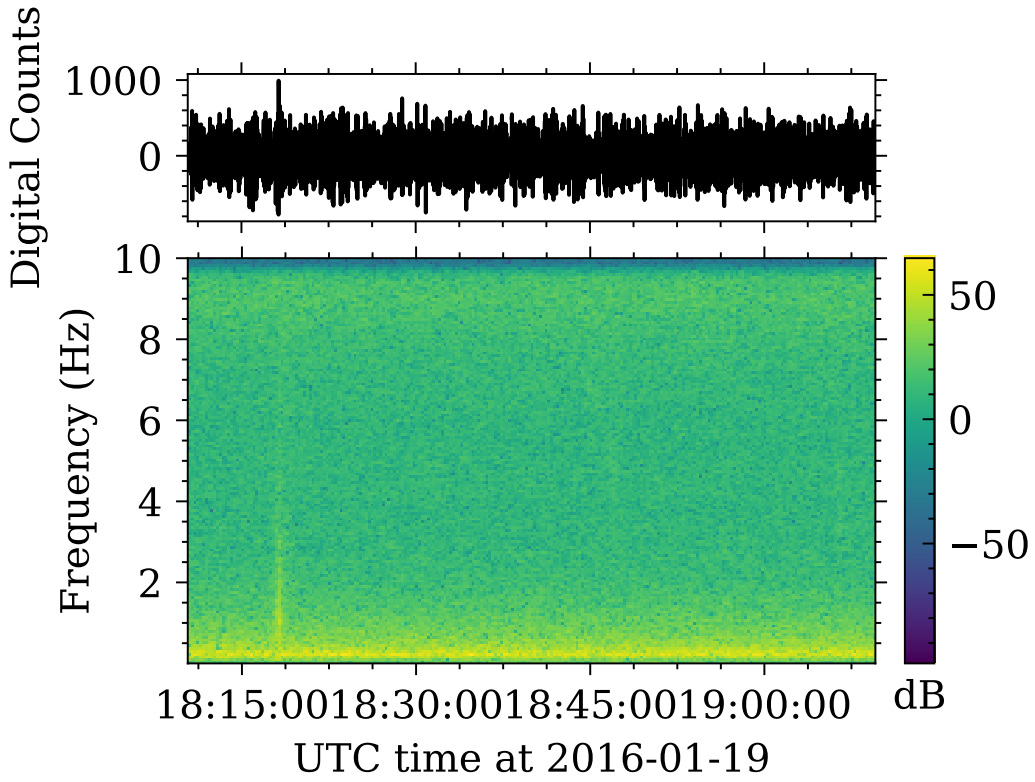

Figure 2.17: Same as in Figure 2.16, but filtering with 0.1 Hz, to illustrate how strong the microbaroms are.

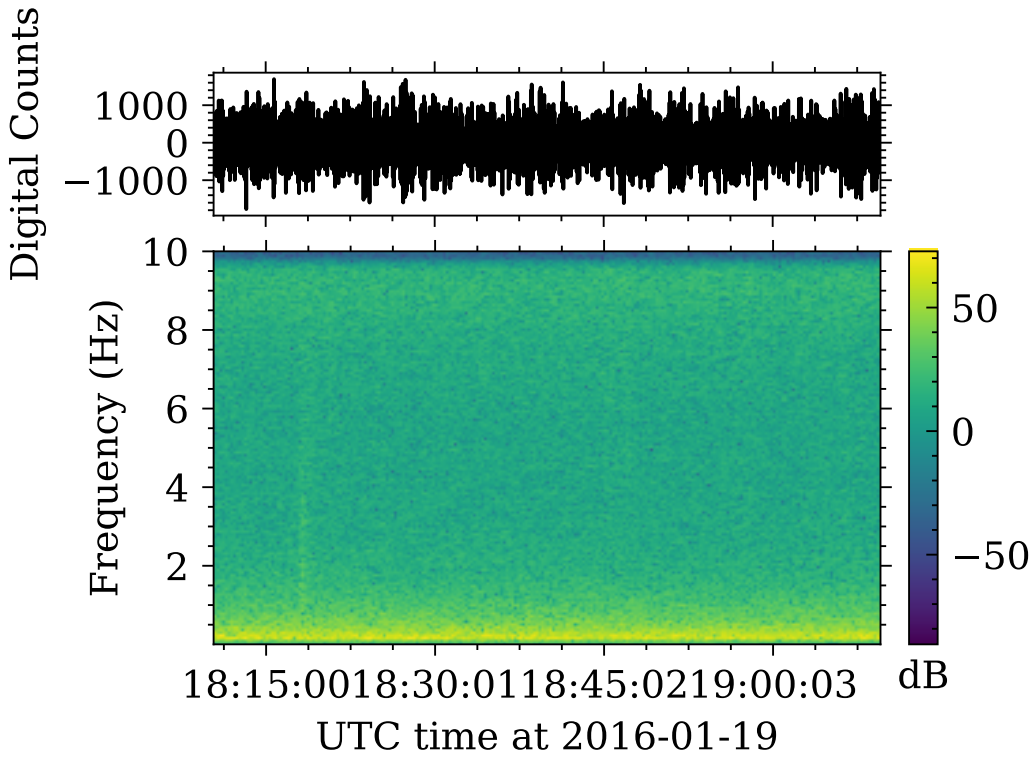

Figure 2.18: Same as in Figure 2.16, but with beamforming towards -100 and a apparent velocity of 340 m/s, that is towards the strong microbaroms from the North Atlantic.

CHAPTER 3

Methods

In this chapter, we go through how the data was collected and how the data were pre-processed. We discuss how the data are displayed and also how the displays are reviewed. In the end of the chapter, we go through a pre-project for building intuition on infrasound properties. These results will also be of relevance for comparing beamforming of transient signals(as in the trial project) to near-continuous microbarom signals from the North Atlantic Ocean.

3.1 Data processing framework

In this study, the data processing takes advantage of the ObsPy framework. ObsPy is open-source library in Python that contains a domain-specific time series analysis toolkit (Krischer et al., 2015; The ObsPy Development Team, 2019).

In the context of the current project, ObsPy provides data structures and basic modules to process time series recorded on a set of sensors. It was originally developed for seismology applications, but it is also commonly used in the international infrasound research community. It provides building blocks, for example, temporal filtering, data input and output, data segment selection, that can be combined and extended in the design of data processing pipelines. Several of these modules provide wrapped interfaces to mainstream signal processing function implementations from, for example, SciPy (Virtanen et al., 2020). ObsPy also includes its own implementations of some basic array signal processing components, for example, implementations of conventional delay-and-sum and adaptive Capon beamforming recipes.

Using this library, we can streamline the processes of analysing the data, from reading the streams and merging multiple streams together. From here we can trim the data to a desired time frame for further processing. We can also apply various pre-processing techniques, such as detrending and frequency filtering.

Using the tools available in ObsPy, we can customise the beamforming recipes, in order to make systematic studies that optimise the characterisation of microbarom infrasound wavefields.

There are several additional openly available seismic and infrasound data processing packages that, based on the ObsPy infrastructure, provide supplementary

processing and visualisation modules. One such example is the University of Alaska Fairbanks (UAF) UAF geotools Python library (UAF Geophysics team, 2023). This includes additional data logistics modules, as well as some beamforming-related code. In this project, we used the framework supplied and from there we made our own framework, based in the UAF geotools. This library incorporates a collection plotting tools to displaying data and processing outputs like, a trace, backazimuth and autocorrelation.

As a project goal is to optimise beamformers with respect to microbarom direction-of-arrival, key visualisation displays are array signal power maps as a function of horizontal slowness (S_x, S_y). After finding the horizontal slowness (which can be mapped into backazimuth and apparent velocity) of the peak power, we study how this evolves as the signal time window is slid over the array data time series.

3.2 Preparing the data

When reviewing the dataset, there were some bugs when reading the miniSEED. The files were troubleshooted one-by-one, and when we found the corrupted bug. From this we split the dataset into two, with the split defined by the bug (so the bug is excluded from both data streams). We also had some artefacts when plotting the power maps in the slowness space, where the estimated slowness of the dominant source was found in the centre of the (S_x, S_y) grid, indicating an infinite apparent velocity corresponding to a wavefront impinging from the vertical direction.

The dataset is stored in a format called miniSEED, which is a format widely adopted in the seismology and infrasound communities. miniSEED is a subset of SEED, a standard that is used to store time-series data. Being a more restricted file format, storing less metadata makes this a more compact file format (Ahern et al., 2012). The format is also supported by ObsPy, which makes the pipeline more streamlined, as there are functions for reading miniSEED-files in this library.

After the miniSEED files had been read, we could start processing the data and retrieving relevant information about the infrasonic soundscape. Combined with the information available from a station-specific metadata file (in stationXML format; see, for example, Saurel et al. (2020) for an overview of the format), all data and metadata information for further processing are available, including the names of the traces, start and stop time of the stream, geographical location of the array sensors, sampling frequencies, etc.

As the stream was long, it was provided in multiple files. These files could be read one-by-one and later merged into a single Stream object in ObsPy. After this, the position data for all traces were added to the miniSEED file. Using the position date, we could create a function to calculate r_{ij}. A variable that stored all the position data, which was put as a parameter when computing the power maps.

Before we started the computation of power maps, we needed to perform some pre-processing to the stream. This procedure is explained in the following

sub-chapter.

3.3 Pre-processing and temporal filtering

Before we start applying any beamforming to our stream of data, using detrending, by implementing `st.detrend`, we are making sure that the data are demeaned. Otherwise, we can end up with massive artefacts when filtering. Then we use `st.taper` to specify the type of tapering that we are using to detrend, for example, a Hann window. In addition, we can specify the maximum percentage of tapering at the end. Finally, we apply a bandpass filter using `st.filter`, we are using this to get the signal in the frequency ranges that is of our interest. As demonstrated in, for example, De Carlo, Hupe et al. (2021), the microbarom wavefield peaks at around 0.2Hz. Therefore, we study the data after filtering with a passband of 0.1 - 0.5 Hz. An illustration of the tapering in time is provided in Figure 3.1.

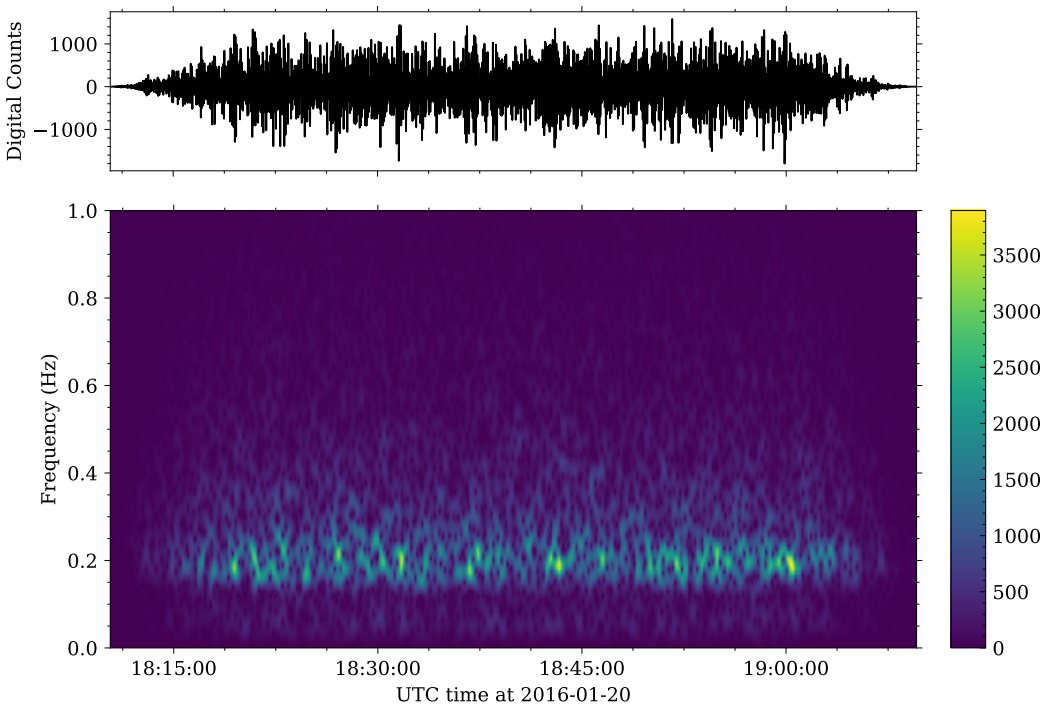

Figure 3.1: Plot of the microbaroms at a normal state, without strong competing transient signals. A heavy tapering is applied when filtering the channel data trace, for a better illustration of how a tapering effects the wavefield. The colour-bar on the right indicates the intensities as the square root of the spectogram.

3.4 Processing the data

After we have pre-processed the data, we need to set parameters for the beamformers. This includes parameters like window length, window fraction, the slowness grid, the threshold for semblance, the lower and upper frequency of the data, start and end time, whether to use prewhitening, and which coordinate system to use.

The window length defines the window length for which each of the power maps is computed. The window fraction gives the stride until the start of the next process window, in relation to the window length. By defining a ratio between the window length and their respective window fraction, we can set the length of each step so that the number of the collection of the power maps corresponds to the same time for a different computation using a different beamformer. We define this as the starting point for each computation.

When we consider incoming waves, they are acoustic waves travelling in the air, which means that they have a speed of around 340 m/s at ground level. Hence, we construct a slowness grid where this would be the most natural focus. We defined the grid to be plus minus 4 for both axes. We also display a circle with the slowness corresponding to the local speed of sound.

After making multiple calculations using the Capon's method without prewhitening, we got some really noisy results. The prewhitening is a diagonal loading applied to the correlation matrix. This corresponds to adding white noise to our known signal, meaning that the Capon method resembles the delay-and-sum beamformer a bit more. The idea is to reduce leakage of the most intense spectral components that have been badly resolved. Hence we will get a more uniformly distributed spectrum that approaches white noise. (Thomson and Emery, 2014).

In our study, we have split the project into phases. The first phase comprised gathering the data and storing this in miniSEED files. We then made a function for gathering the data in a more accessible way. From this we could get the desired data with a defined start and stop time. The next step was to perform computations, such as computing power maps of the stream. To make these computations available in later stages, like plotting in slowness space, etc., we need a way to store this. This is done by a store function, which allows us to save the power maps in `.npz` files.

3.5 Reviewing the processed data

3.5.1 Backazimuth

Considering longer datasets of infrasound arrays, we can construct multiple power maps in a time series. From this we can extract the dominant position of the power maps iterative. This gives us the backazimuth given by the incoming direction of the dominant signal. Considering backazimuth plots, we can display how the dominant incoming signals in a wavefield change over time. For example, do we

have one dominant infrasound source over time, or is the dominant part of the wavefield mostly a collection of transient signals?

If we consider shorter window lengths when finding power maps, then there is a greater possibility that a transient signal is the most dominant signal. Such strong signals can, for example, be a signal from a volcanic eruption, like the signal observed at the OKIF array station, which will be studied further in the Section "Initial pre-project to build intuition on infrasound array data properties".

When we consider the backazimuth plots later, we need an idea of what makes a good backazimuth estimate. For example, when we consider the OKIF array station, we need to have backazimuth estimation that can pick up shorter duration signals, like the transient signal from a vulcanic eruption. In contrast, when we consider longer, near-coninious signals, such as the microbaroms that originate from the North Atlantic Ocean, we would like a plot with low variance and with window lengths sufficiently long, so that transient signals are filtered out (see the plot of the explosions from the mine from Aitik in northern Sweden, 2.16). With this sort of boundary for filtering out transient signals, we would still like to keep the window lengths short to be able to pick up smaller changes between incoming microbarom signals.

3.5.2 Median of backazimuth

When we compare the estimated backazimuth with the plots where we apply a mean or median over a given window, we get a smoothing effect, which gives less variation in the plot. However, by doing this, we might lose some resolution in the temporal variations. Therefore, we apply a shorter sliding window when calculating the mean and median of these estimates. When comparing the plot of mean compared to median, the median statistic is known to be robust to outliers. These outliers could potentially lead to a skew in the estimated direction.

First, we will display the backazimuth found from the data processing. To assess the results, we want to evaluate the stability and robustness of the beamformer. When we plot the standard deviation, we can get a view of how the backazimuth varies in time to study the beamformer stability. The standard deviation plot also shows when there are structural changes in the dominant incoming signal.

Hence, to evaluate the processing output, we have implemented statistics such as mean, standard deviation, and median. Then we will evaluate whether one of the approaches can be superior when considering the incoming direction-of-arrival. We may implement these statistics on the data in several ways, but we have opted to use a rolling window of 7 samples. In the time series, the distance from one data point to another corresponds to 7 minutes and 30 seconds. Therefore, the total time of a sliding 7-sample window is 52 minutes and 30 seconds. In Figure 3.4, we show a transient signal that originates from an eruption of the Bogoslof volcano in Alaska for a duration of 5 minutes.

Using the rolling window, we keep a similar number of data points in the plots. The length of the rolling window is 7, so we keep some variation in the plots,

focussing more on cancelling out potential outliers. By outliers, we mean potential noise from strong infrasound sources near the array that is not considered to be microbaroms but more likely transient sources.

With the aim of cancelling out transient sources from our plots, we are going to choose the most desired statistic for presenting the data. By plotting the standard deviation, we get a view of the variation of the stream. It can potentially be a good way to tell when the incoming direction of a dominant signal changes, but it does not tell us anything about where this new source is coming from.

Considering plotting the mean of a 7 sample rolling window, it can most likely be a good way to remove smaller local variations. However, if we have an incoming transient signal from a different direction, this can have a greater impact. These transient signal outliers could potentially skew the estimated direction. Since we use overlapping window lengths, multiple estimations will be affected by the outlier, and hence the estimated incoming direction will change. That is, the predictions are not as precise.

To cancel out potential transient signals in the backazimuth display, we apply the median. This will provide some smoothing of local variations and cancel out shorter transient signals. If we consider the incoming transient signal from the volcano eruption, this would be present in two windows at most, and would be filtered out by the rolling median window of 7 samples.

3.5.3 Power maps plotted in slowness space

The power map plot displays the intensity of the dominant incoming wavefront and its geometry, such as the direction and velocity of the incoming wave. When we display the power maps, we plot them in terms of relative power in the slowness space. Slowness is the reciprocal of velocity. The slowness space is defined by two slowness components, S_x and S_y, one in each direction. From this we can build the slowness grid. We start by defining S_x and S_y (see, for example Schweitzer, Fyen et al., 2012);

$$S_x = \frac{\sin(\theta)}{V} \tag{3.1}$$

and

$$S_x = \frac{\cos(\theta)}{V}, \tag{3.2}$$

where V is a grid of different velocities.

From this we can define the slowness grid as:

$$S(x, y) = \sqrt{S_x^2 + S_y^2}. \tag{3.3}$$

We have made a figure that contains five subplots. The upper part is a 2-by-2 of square-shaped slowness plots, while the lower subplot is a backazimuth plot. All the slowness plots have a label shown in the upper right corner indicating

which beamformer is used and the window length applied. The slowness plots each have their corresponding colour bar, placed to the right of the subplot. In the backazimuth plot, the starting times of all the displayed power maps are indicated in red, in the upper right part of the plot. The window length of the backazimuth estimation is indicated with a transparent red box that hovers over the entire length of the y-axis. The window length, along with the beamforming method, is placed in the upper right of the backazimuth plot.

3.5.4 Initial pre-project to build intuition on infrasound array data properties

In this section, we apply array signal processing in a small-scale experiment to build intuition and understanding of the characteristics of atmospheric infrasound signals recorded at array stations. Here, we are processing a stream with a duration of 7 minutes consisting of four traces.

This is a dataset that contains a frequency of a range similar to our main data, but for the current mini-study we have a known source. It is a stream from an infrasound station called OKIF. This station is near an underwater volcano and we reproduce the results of Lyons et al. (2020).

In Figure 3.2, we have an overview of the OKIF array station. On the lower right, we can see the array design, showing the position of each of the station elements. On the upper right, we have the array response function for the array, showing the theoretical resolution. On the upper and lower left, we have the estimated uncertainties of the backazimuth and apparent velocity, respectively.

In Figure 3.3, we can see a data display of the OKIF array station, calculated using a library from the University of Alaska Geophysics Tools (UAF Geophysics team, 2023) Python repositories. The display gives us a good overview of the stream of data. This will later be used as inspiration when deciding which calculation and techniques should be used on the IS37 array station data.

The upper panel of the data display shows a simple pressure plot of one channel. The second panel is a plot of the median of the cross-correlation maxima for each processed window. A good indication to know if the incoming stream is incoherent and, if so, if the signal changes. The third plot is an estimate of the trace velocity of the dominant incoming signal. This estimation can be used as another way to characterise the incoming signals. The fourth plot shows an estimation of backazimuth showing the direction-of-arrival. Such plots will be studied in more detail later. In the bottom plot, we have an estimate of the uncertainty in the measurements.

As both the source and station positions are known, it is easy to compute the angle of the incoming wave field. Using these as known factors and by making a cut-out of a stream where we know when the wave arrival was present in the data, we can use this to study how beamformers perform when we estimate the backazimuth. In 3.4 we have plotted a collection of plots from computations using the delay-and-sum beamformer. Considering the slowness plots, we see that

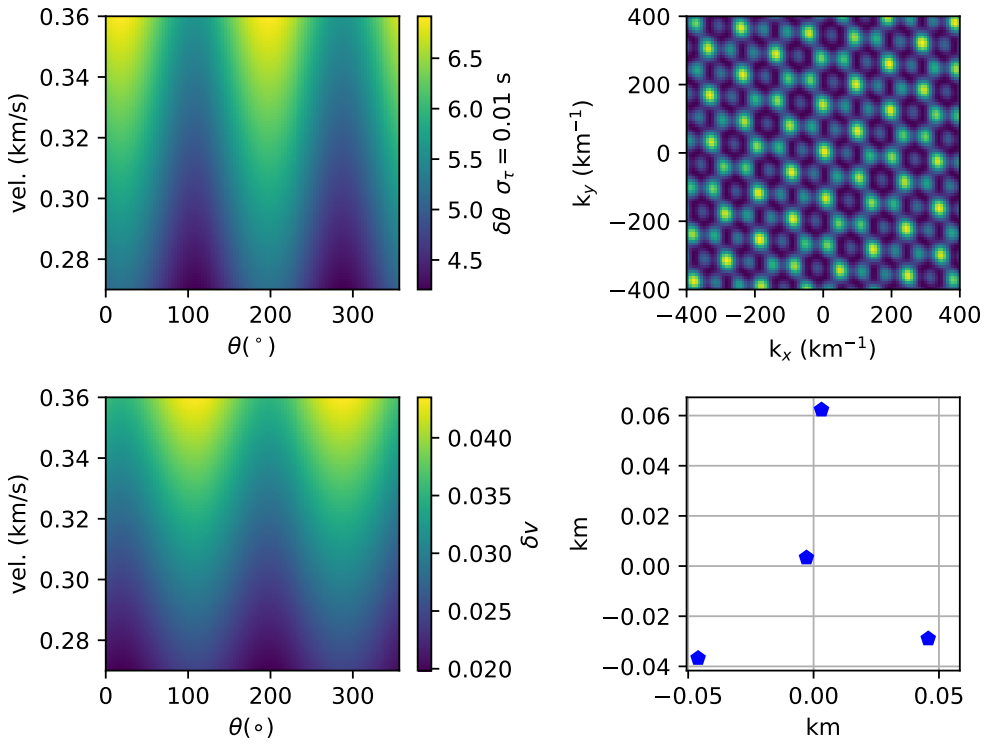

Figure 3.2: Collection plot of the design of OKIF array station using the UAF-geotool package. This uses the framework of Szuberla and Olson (2004) to estimate the uncertainty in backazimuth estimation (top left panel) and in the apparent velocity estimation (bottom left panel). The top right shows the array response function and the bottom right the array sensor relative locations.

the indicated intensities of the incoming sources are large, which means that the resolution of the beamformer is low.

What makes this interesting is the comparison between the two lower subplots. The lower subplot shows the preprocessed stream from the incoming signal from the Bogoslof Volcano eruption. The incoming signal is a transient infrasound with a duration of around 5 minutes. When estimating the backazimuth, it is quite clear when the signal arrives. The backazimuth is close to constant under the same duration as the incoming signal from the eruption is present.

Studying Figures 3.4 and 3.5, we can see higher intensities in the slowness plot using the Capon's method. We can also see that when using Capon's method, the main lobe in the plot is smaller, meaning the resolution is higher, compared to using delay-and-sum.

Again, considering Figures 3.4 and 3.5, these plots are mainly how we will consider the data from the IS37 array station at Bardufoss. That is, each plot of the backazimuth and then of the power maps displayed in the slowness space.

The plots will mostly be considered by eye; for example, when we consider

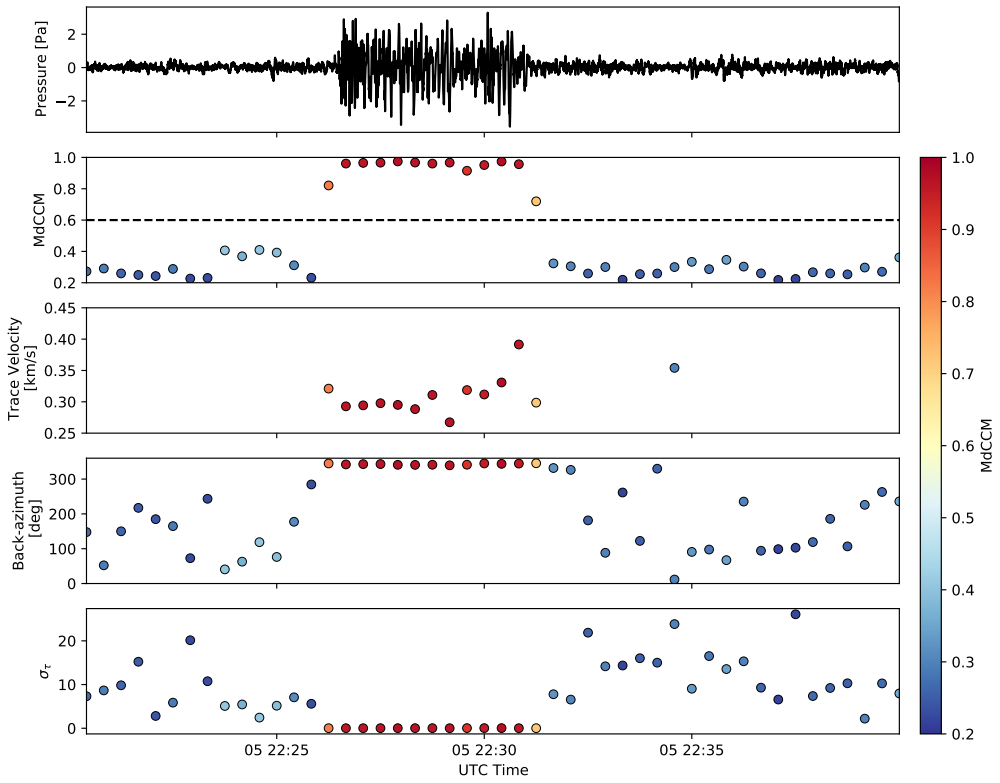

Figure 3.3: Data display of the OKIF array station for estimating direction-of-arrival. Top panel: Pressure trace or the central array element, bandpass filtered between 0.1 and 20 Hz. Second panel: average inter-element correlations for each processing sliding window. Third panel: Trace velocity estimates. Fourth panel: Backazimuth estimates. Bottom panel: an estimate of uncertainty in the measurements (see Bishop, Fee and Szuberla, 2020).

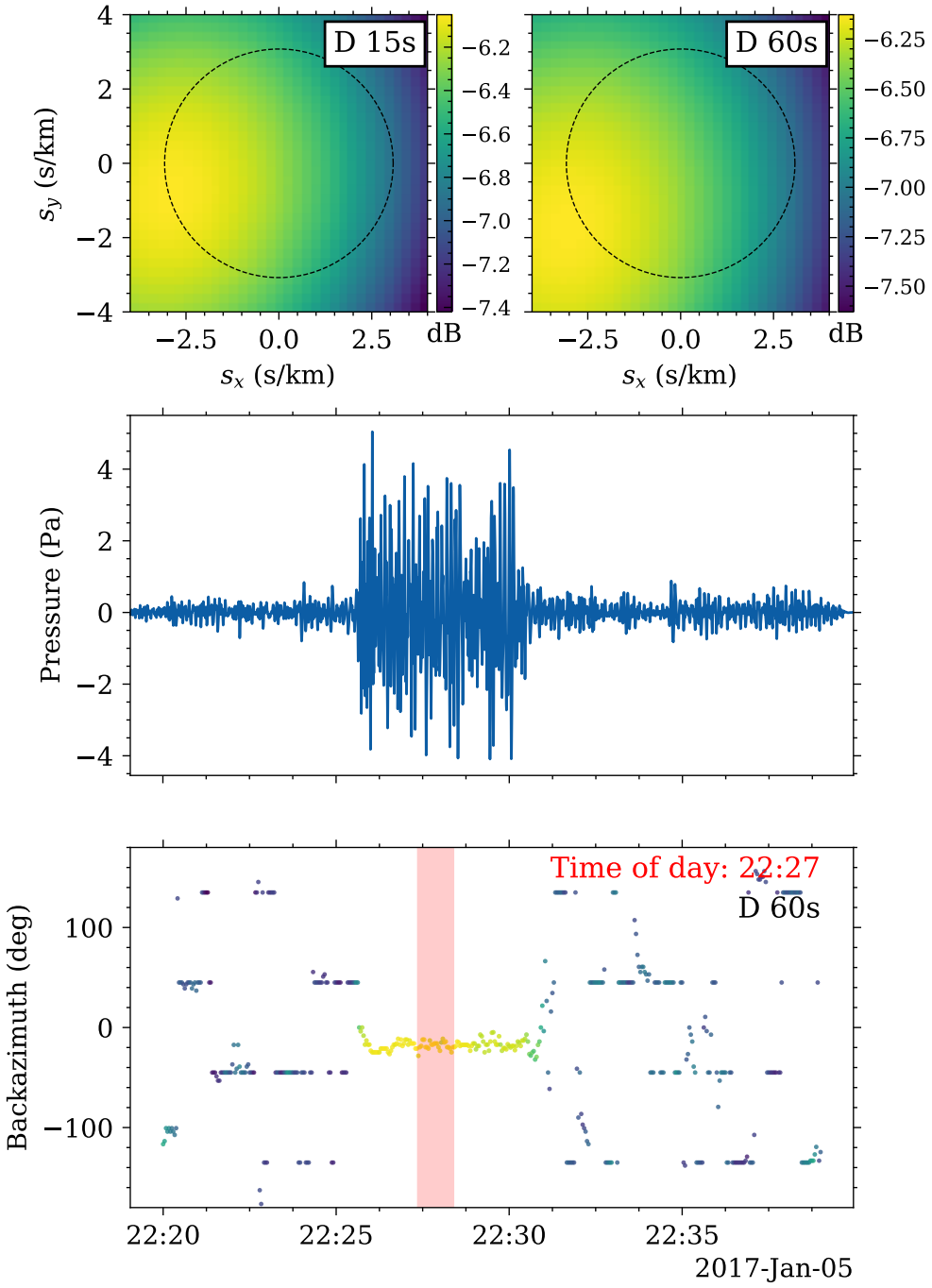

Figure 3.4: OKIF array station data display for 5 January 2005. Top panels: Power in dB as a function of slowness estimated using delay-and-sum, with a window length of 15 (left) and 60 (right) seconds. The black circles correspond to an apparent velocity of 340 m/s. Middle panel: Bandpass filtered channel trace from 0.1 to 0.5 Hz. Bottom panel: backazimuth as a function of time, with a transparent red box at 22h27 indicating the window length.

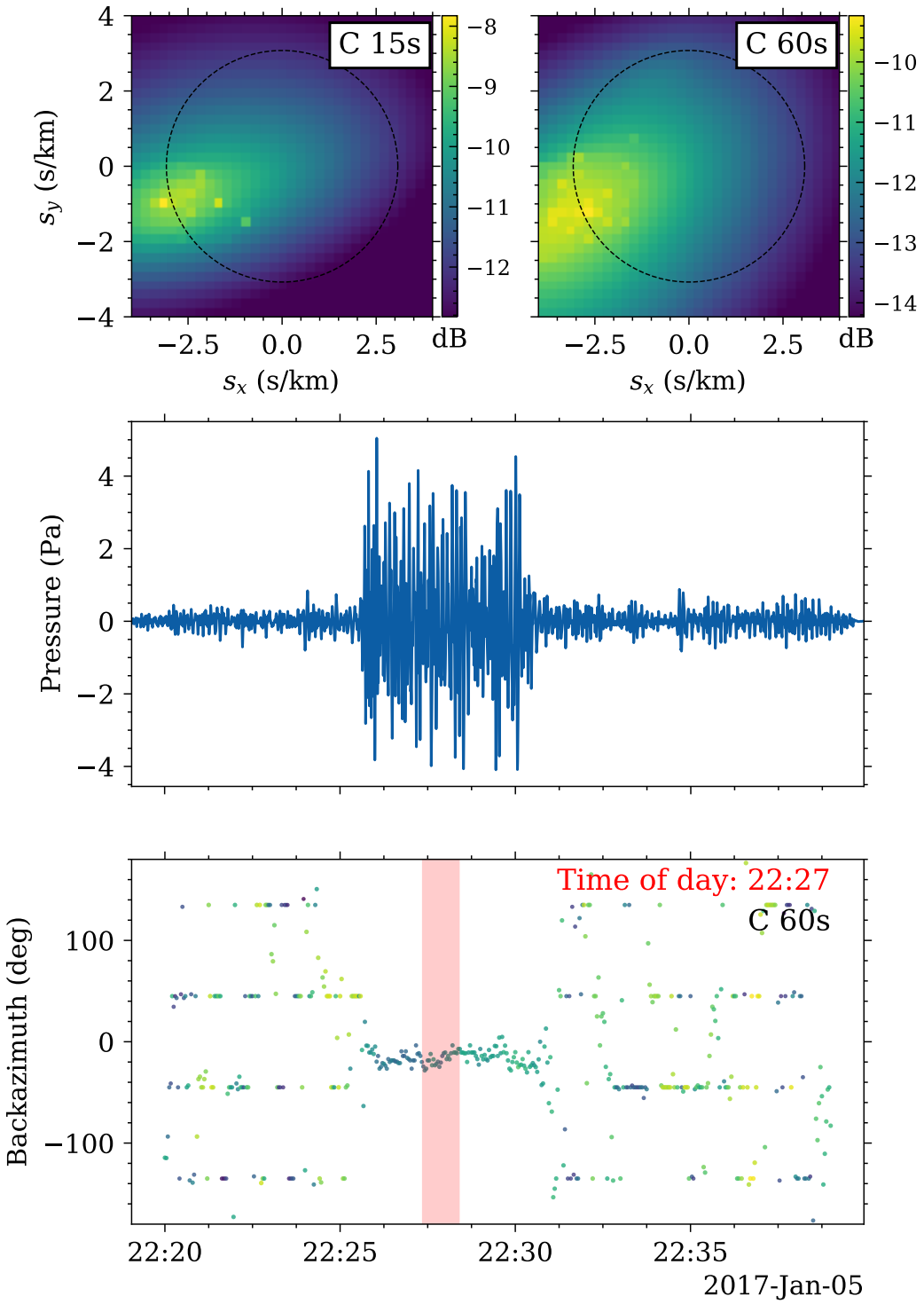

Figure 3.5: Same as Figure 3.4, but estimated using Capon's method.

backazimuth plots, then we would mostly prefer a locally low variance, but it is also essential that the estimations pick up changes in the incoming wavefield and how fast these changes are noticed. The changes in backazimuth are compared with the stratospheric winds similar to what we see in the images 2.5, 2.6 and 2.7. Also, as we know of the stronger microbarom sources and their location, we have a few expected directions-of-arrivals. The strongest and therefore the most commonly found dominant incoming signals are microbarom sources from the North Atlantic Ocean, the Greenland Sea, and the Barents Sea Vorobeva et al. (2021). Later, the backazimuth plots will also be evaluated in relation to the power maps to consider whether the estimation of the apparent velocity makes sense. Summarised, for the backazimuth plots, we would like as little local variance as possible, but the ability to notice changes in the wavefield is essential.

After the backazimuth plots have been evaluated, we are going to display and evaluate power maps in the slowness space. In all of the plots, we add a plot of backazimuth in the bottom panel, as a reference to the power map calculations. For each of the data displays of power maps, we have included the backazimuth estimated with the same beamformer as the four power map plots, estimated with what we found to be the ideal window length.

CHAPTER 4

Results

In this chapter, we provide the results of our main study related to microbarom wavefield characterisation, using the methods implemented and described in the previous section. First, we describe and comment on the findings from estimating the backazimuth direction-of-arrival. We do this by plotting and commenting estimations of backazimuth and plotting the estimations as a function of time.

The focus is on assessing the effects of choice of beamformer and length of the moving processing time window on the estimated backazimuth of the dominating microbarom wavefront. We also study the beamformer algorithm and the window length effects on the power maps, where the estimated beamformer output is plotted as a function of horizontal slowness.

4.1 Backazimuth estimation

In this section, we evaluate the backazimuth estimations, a plot that indicates the direction of arrival of the dominant incoming signal. Normal backazimuth plots are reviewed first. Then in order to minimise the variance of the plot, we use a rolling 7-sample median. The standard deviation plots of the backazimuth are also reviewed.

Here, we give an overview of the displays presented in this section. First, we show the two figures, 4.1 and 4.2, showing backazimuth estimates. The first is a comparison plot of the two beamformers, both estimated by using a one-hour window length. The second is a comparison plot of what we found to be the ideal window length for the specific beamformer. That is 15 minutes for the delay-and-sum beamformer and 8 hours for the Capon's method. Looking at Table 4.1, we can clearly see that the estimates using Capon's beamformer would benefit from a longer window length, while the delay-and-sum beamformer has a reasonable low variance for the shortest window length compared to the results found by the Capon's beamformer.

For the other following estimations of backazimuth, a 7-sample rolling median was used, in order to cancel out potential outliers and also for reducing the variance in the plots.

Table 4.1: From the IS37 array station from 28 January to 4 February 2016. In this table, the averaged variance of the estimated backazimuth has been computed for the two beamformers, with window lengths from 0.25 to 8 hours. The calculations were performed using the SciPy method to calculate the variance of the measurements made in degrees (`scipy.stats.circvar`) and then to average the result over the number of samples.

Window length	— Variance $[[^\circ]^2]$ — Delay-and-sum	Capon
0.25h	62.4	1119.5
1h	30.7	831.5
2h	22.1	710.9
4h	19.8	846.2
8h	17.6	458.8

In Figure 4.3 we compare the two beamformers (DAS and Capon's method) using a 7-sample rolling median of the backazimuth, using the same window lengths(one hour), indicates that the Capon's method results in more variation when estimating backazimuth for finding direction-of-arrival. In Figure 4.4 we have a similar plot similar to that of Figure 4.3, but we use window lengths of four hours. The result is similar, that we get higher variation using Capon's method. In Figure 4.5, we display a comparison plot of different window lengths, 15 minutes and 8 hours, both with the delay-and-sum beamformer. The results are similar, but the computation with a shorter window length has more variation. The Figure 4.6, the plot similar to that of Figure 4.4, but using Capon's method. The result is the same, meaning that a shorter window gives a higher variation. The Figure 4.7, is a comparison plot of the two beamformers, delay-and-sum with a processing length of 15 minutes and Capon's method with a processing length of 8 hours. The Figure 4.8, is a plot demonstrating the importance of preprocessing before beamforming.

We had access to 3 months of infrasound channel data recordings from the IS37 station, starting from 1 January 2016. This time frame is of particular interest because it comprised both an initial period of a strong stratospheric polar vortex, but in early March there was a major final Sudden Stratospheric Warming that disrupted the vortex structure (Manney and Lawrence, 2016). This means that early in 2016, we expect strong ducting of microbaroms from the North Atlantic source region to be recorded at IS37 at backazimuths towards the west. However, from early March, we expect this duct to be disrupted by the change in stratospheric circulation and instead observe microbarom wavefronts from other directions.

When displaying segments of processing output and the associated backazimuth estimation, we plot one week long time period of data. The first example segment is between 28 January and 4 February 2016, where we mostly have a strong eastward stratospheric wind that gives microbarom arrivals at IS37 approximately from

the west. In early February, there is a brief period with dominant microbarom wavefronts that arrive from the north. Considering this period of time, we can study the processing output when the stratosphere is in a normal winter state, but also see how the beamformer performs when another source direction dominates the microbarom soundscape at IS37.

In practise, we apply the processing pipelines in chunks, one week at a time, to the entire stream of available data. Both power maps and backazimuth estimations were saved in separate folders and were hence accessible later for plotting and further analysis. The output of the different options of the beamformers and parameter settings was saved separately in an ordered folder structure. We coded a generic plotting framework that allows one to visualise the backazimuth estimates as a function of time.

Thereafter, we plotted the backazimuth rolling medians estimated using different computation approaches and compared these.

4.1.1 Estimation plots of Backazimuth

In this section, we study how the results vary when we consider the two different beamformers in the study: the delay-and-sum beamformer and Capon's method. In the following computations, we have used the same window length when comparing the two methods. We perform the same comparison using two different window lengths.

In the figures, 4.1 and 4.2, we display two plots for comparing the beamformers. The first was at a one-hour window length, then at what we found to be the ideal window length for the beamformer. The beamformer used and the window length of the computation are specified in the upper right corner in the figures.

We can note that the variation is high in Figure 4.1, where Capon's method has been applied. In comparison, the variance for the delay-and-sum beamformer is low. Also, both of the beamformers seem to roughly follow the same estimated direction-of-arrival. In Figure 4.2, the results are as expected. We can see that the variance of Capon's method is much lower, and the predicted directions-of-arrivals are better. For the delay-and-sum beamformer, there is more local variation, compared to the one-hour window-length computation.

4.1.2 Beamformers comparison using the same sliding window

In this section, we study how the results vary when we consider the two different beamformers in the study: the delay-and-sum beamformer and Capon's method. In the following computations, we have used the same window length when comparing the two methods. We perform the same comparison using two different window lengths.

The output shown in Figure 4.3 was calculated with a window length of one hour, while Figure 4.4 had a window length of four hours.

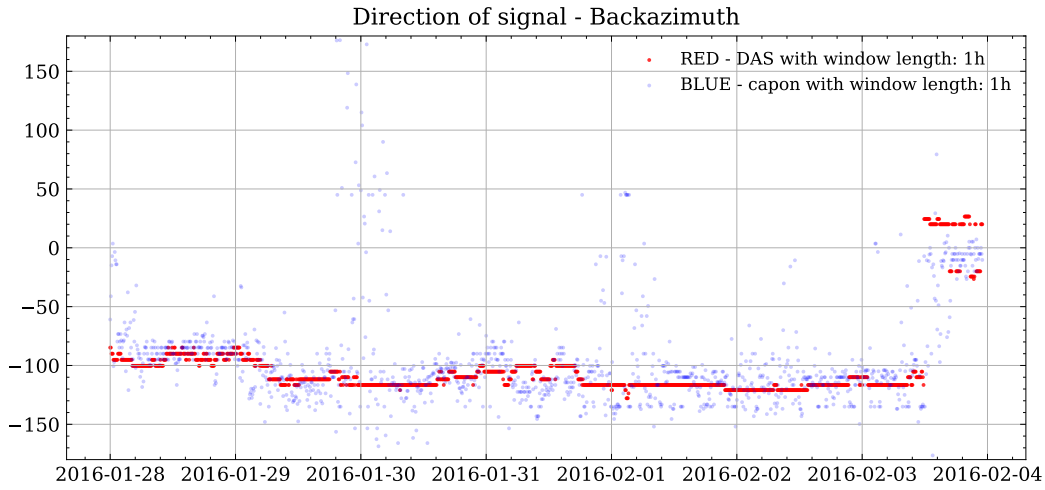

Figure 4.1: I37S station data processing output, displaying the estimated backazimuth from 28 January to 4 February 2016. Estimations of a microbarom direction-of-arrival is shown as backazimuth estimations using the beamformers, delay-and-sum (blue) and Capon's method (red). For both beamformers, the processing time window length is one hour.

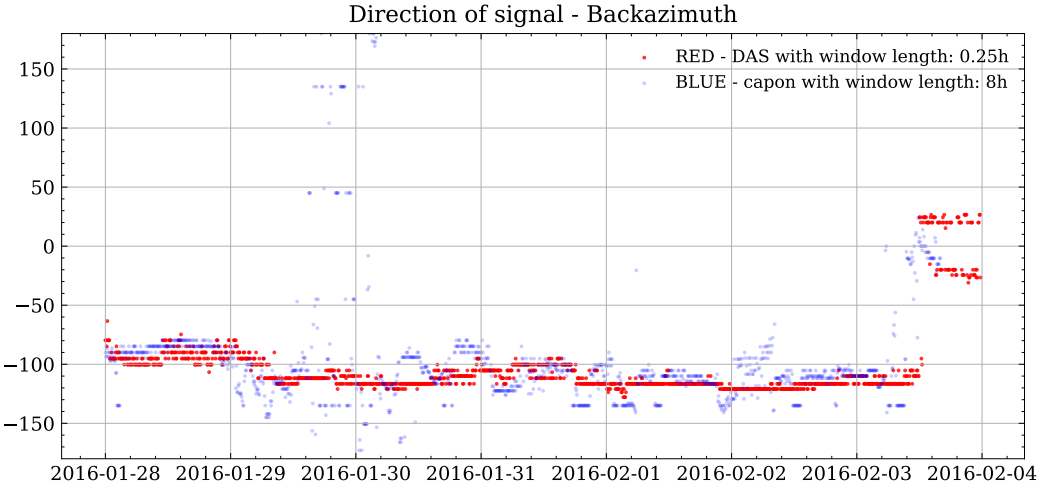

Figure 4.2: Same as in 4.1, displaying the estimated backazimuth from 28 January to 4 February 2016. Calculations made using the beamformers, delay-and-sum (blue) and Capon's method (red).

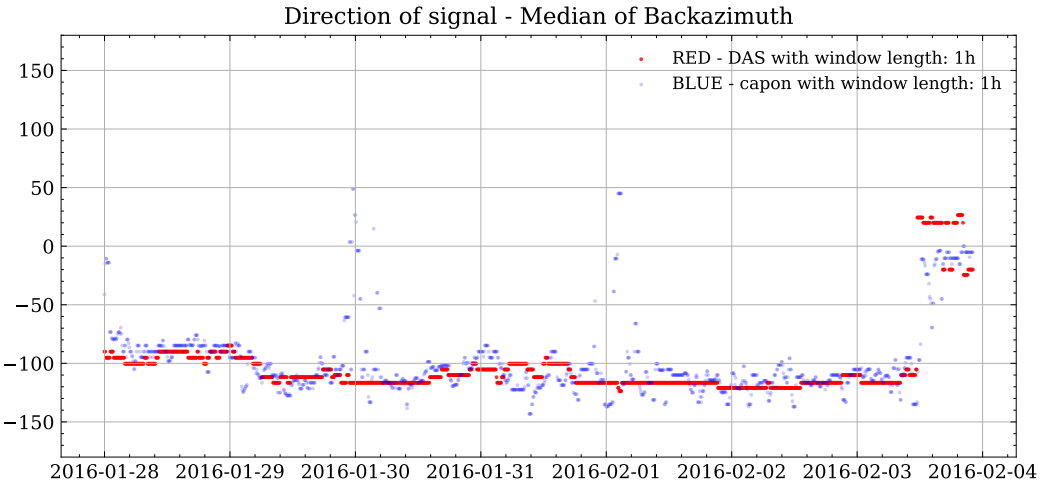

Figure 4.3: I37S array station data processing output, displaying the estimated backazimuth from 28 January to 4 February 2016. Estimations of a microbarom direction-of-arrival is shown as the median of the backazimuth estimations using the beamformers, delay-and-sum (blue) and Capon's method (red). For both beamformers, the processing time window length is one hour.

Looking at Figure 4.3, we note that the variation of the computation using Capon's method, represented with blue dots, is higher. We also see estimates of some incoming signals from around zero degrees around 30 January and 1 February. Comparing this to the delay-and-sum beamformer, displayed with red dots, we find that these incoming signals are not picked up. However, both beamformers picked up the new signal backazimuth structure at the end of the timeframe, which appears on 3 February.

Further comparing the beamformers Figure 4.3, with the plots in Figure 4.4, where the window length is four hours, we can see that the variance is lower. Capon's method appears more consistent in the computation with four hours than with a one-hour window, but still contains the changes around 30 January and the first of February that the delay-and-sum beamformer did not estimate. In these figures, it seems that Capon's method is more sensitive to picking up signals from other directions.

With the insights from Figure 4.3 and Figure 4.4 in mind, we now investigate how the estimates vary when we change the window length. Figure 4.5 shows the plots from using delay-and-sum with a 15 minute and an 8-hour window, and Figure 4.6 shows the estimated microbarom backazimuth from the Capon's method with the same window length.

In Figure 4.5, we see that the blue-dotted graph of the 8-hour window has a low variance with almost no changes in the median but still indicates another source at the end of the timeframe. The other plot, the blue dotted with a window length of 15 minutes, shows slightly more variation, but does not deviate much from the other plot.

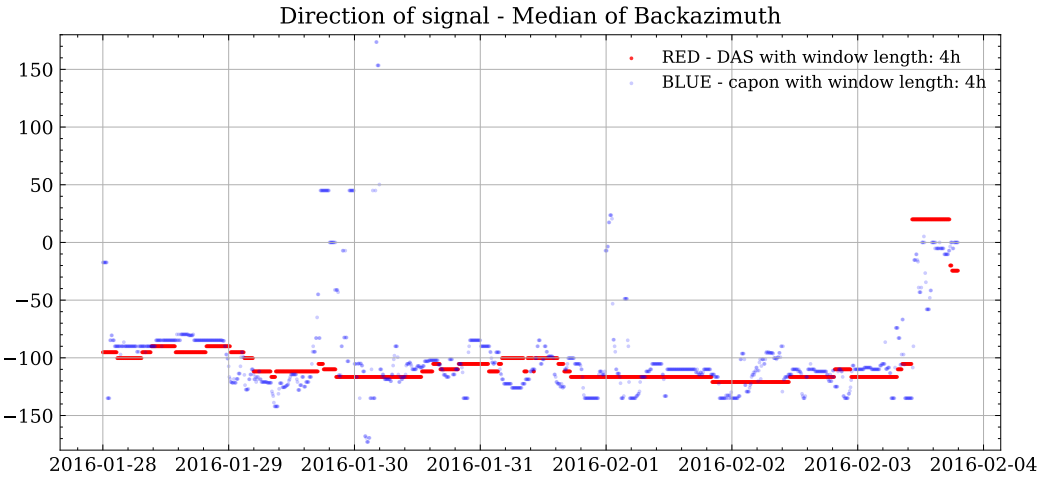

Figure 4.4: Same as in Figure 4.3, but with the backazimuth estimations made using a window length of four hours.

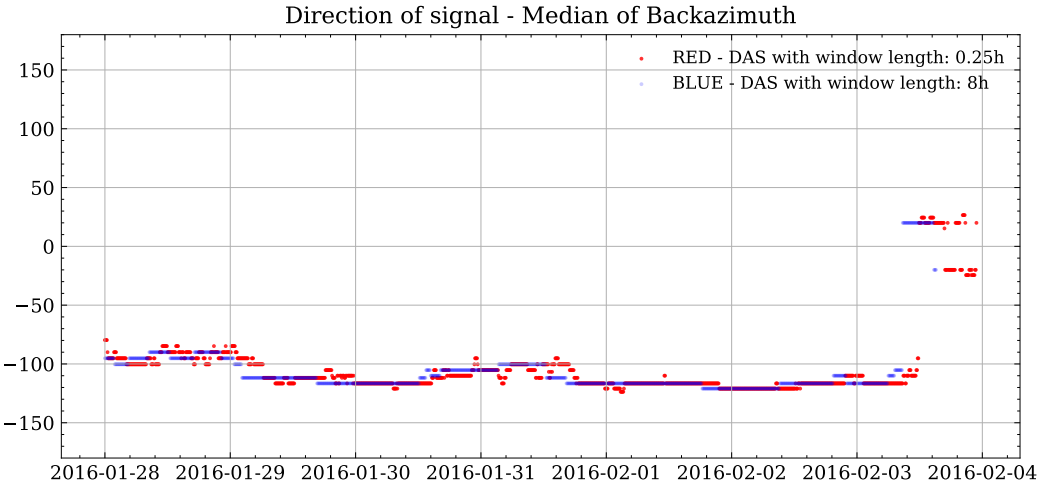

Figure 4.5: Same as in Figure 4.3, but both estimations have been made using delay-and-sum, using a window length of 15 min (red) and 8 hours (blue).

In Figure 4.6, we see a pattern similar to that in Figure 4.5. The shorter window length shows a higher variation in the plot, whereas the beamformer with a longer window length seems more constant. Also, the possible alternate source on the first of February is not present using the longer window length.

Figure 4.7 shows a comparison of how the median of the estimated backazimuth compares using Capon's method with a long window length and the delay-and-sum beamformer using a short beamformer. We can see that the computation using Capon's method, illustrated by the red-dotted plot, still has more variation and shows the alternate incoming source in 30 January. On the other hand, the blue-dotted plot illustrating the computation using delay-and-sum shows that the

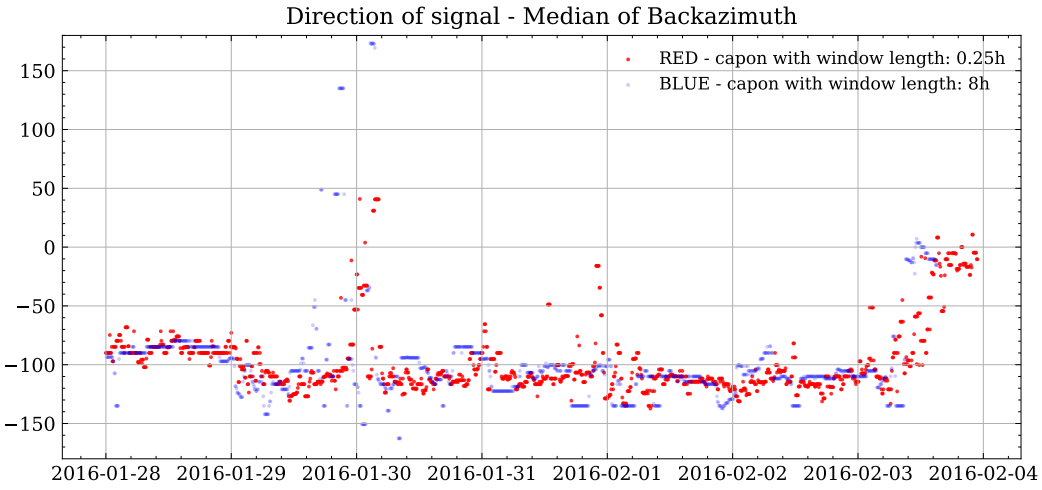

Figure 4.6: Same as in Figure 4.3, but both estimations have been made using Capon's method, using a window length of 15 min (red) and 8 hours (blue).

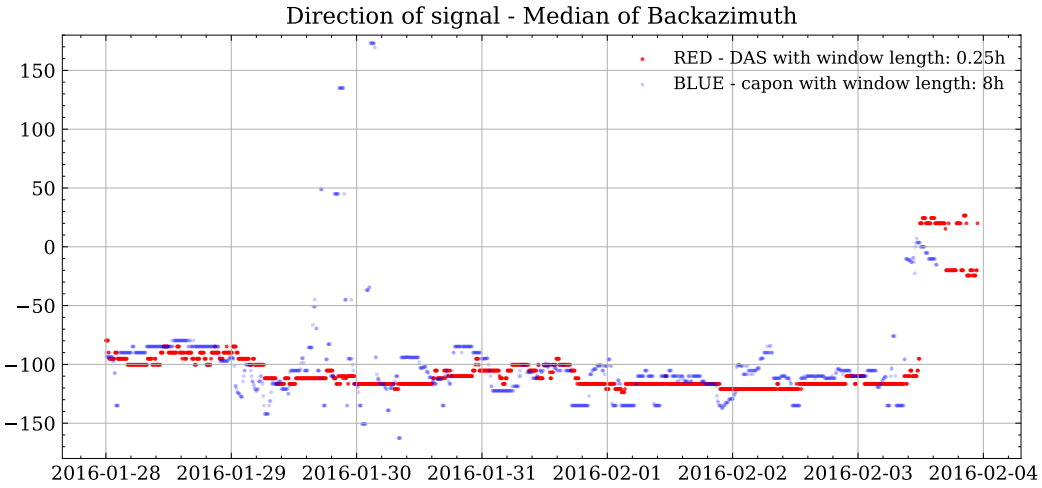

Figure 4.7: Same as in Figure 4.3, but one estimation is made using delay-and-sum with a window length of 15 min (red), while the other is made using Capon's method with a window length of 8 hours (blue).

new dominant incoming source is more pronounced.

4.1.3 Demonstration of beamforming without prewhitening

In Figure 4.8, we see the difference between a computation using Capon's method, with and without the usage of prewhitening. The addition of prewhitening corresponds to the addition of white noise on the correlation matrix, called diagonal loading. The plot shows the improvement in performance using diagonal loading. For later studies, it would be interesting to see how the performance compares to

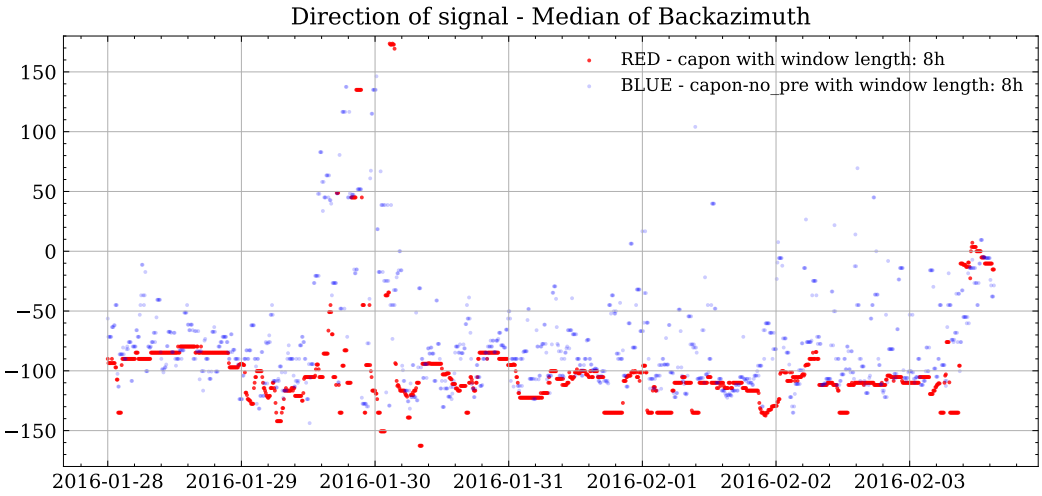

Figure 4.8: Same as in Figure 4.3, both estimations have been made using Capon's method with a window length of 8 hours, but one is estimated without prewhitening (blue).

a heavier diagonal load. This is because the delay-and-sum beamformer seems to perform better than Capon's method with a light diagonal load.

4.2 Power maps in slowness space

In this section, we consider the power maps plotted in slowness space. First, we give a general introduction to the type of figure that we use in our illustrations (power map). We then proceed to describe the various figures before rounding off with comparisons of the beamformers when choosing a fitting window length.

The intensity of the infrasound is displayed in colour, described by the colourbar to the right of each plot. All plots contain a dotted black circle indicating the speed of sound at 15 degrees Celsius, which is 334 m/s. This circle is a reference for the slowness space plots. Sources that go towards the centre have a higher velocity and go towards infinity. If something is outside the circle, it means that the infrasound has a lower speed and decreases as we go towards the boundaries.

To compact the number of figures, we made an outline of four slowness plots with different window lengths. Under the four slowness plots, we plot the estimation of the backazimuth. We have not used the median in this section, as this would delay not be a direct fit, in time, to the power maps plotted in slowness space. This figure outlay gives a better overview, as we can compare how the slowness maps look at a specified time, shown on the time series of the backazimuth plot.

To highlight more of the difference between the different plots, we have added a flooring effect for the colours in the plots. By doing this, we might lose some of the noise and other incoming sources of lower intensities, but this will make it easier for us to compare the plots and evaluate its resolution.

The intensity of the plot varies over time and certainly in the presence of transient signals. To cancel out this variation, we created a new scale in decibels for every image. We do this by finding the max decibel value in the image and set this to be an upper bound. Subsequently, we set the lower bound of the image with a flooring effect, i.e., setting the lower bound to be the upper bound in decibels minus 5.

In Figure 4.9 we have plotted the power map from an instance where the estimated backazimuth was constant. In the slowness space, we see a clear source with a higher intensity in the lower right of the figure, around the dotted circle, defined as the speed of sound. Also, the four plots in the slowness space are similar.

In Figure 4.10 we have plotted the power map of an instance where the backazimuth plot had a high variance. Note that the delay-and-sum did not estimate a dominant source from another incoming direction, even though the intensity of the backazimuth plot at that time was weaker than that of the normal state. Evaluating the four plots of power maps plotted in the slowness space, we see a lot of variation. There do not appear to be clear similarities between the plots and there do not appear to be any clear signs of a source, as in Figure 4.9.

Evaluating Figure 4.11, we have chosen another moment in the time series to consider another plot in the slowness space. This moment has been chosen because both the computation using the delay-and-sum and Capon's method estimated the backazimuth to have a dominant signal from another incoming direction; see Figure 4.7. In this slowness plot, we can see that the upper right slowness plot, with a window length of two hours, is of decent quality. The upper left is not as good, and the two plots in the middle are mostly random noise.

In Figure 4.12, we see the plot in the slowness space, under a near constant estimate of backazimuth. As the signal seems to be more constant, we have chosen to plot the slowness from a window length of 15 minutes to two hours. In the plots, we see a plot that has the same tendencies as the plot from 4.9, although the contrast that highlights the source is much better. The power map in slowness space computed using Capon's method had a rounder appearance, while Figure 4.9 had a highlighted source that was narrower and followed the black dotted circle, indicating the speed of sound. There are also signs of another secondary incoming source to the left of the dominant source.

In Figure 4.13, we see a display of power maps in the slowness space. We see similarities to the plot in Figure 4.12, but in this figure we see more noise because the contrast is lower. Note that most of the other indicated noise is around the same velocity as our dominant source of microbaroms.

In Figure 4.14, we show a power map in the slowness space, where the associated backazimuth plot indicates that the dominant source is a microbarom wavefront coming from another direction than usual for this time of year. In the slowness plots, we can also observe multiple incoming infrasound sources. A collection of sources comes from the middle left, corresponding to plus/minus 25 degrees. The other collection in these plots comes from the southeast at around -100 degrees.

Analysing the slowness space plots of Figures 4.9, 4.10 and 4.11, we see a small

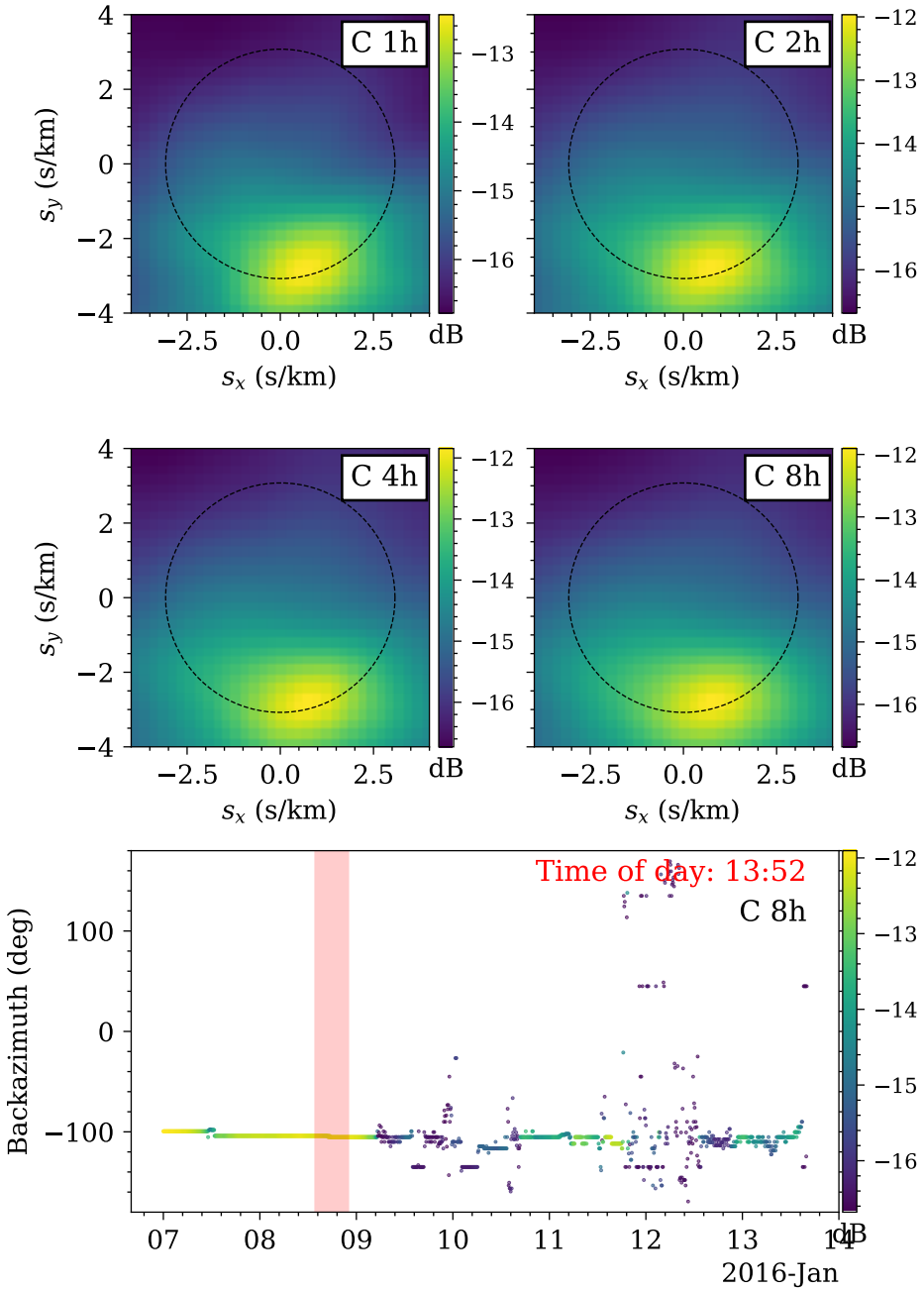

Figure 4.9: IS37 station data display from 7 January to 14 January 2016. Top and middle panels: Power in dB as a function of slowness estimated using capon's method(indicated with "C" in the upper right of each plot, while the "h" stands for the window length in hours), with a window length of 1 h (upper left), 2 h (upper right), 4 h (middle left) and 8 h (middle right) hours. The black circles correspond to an apparent velocity of 340 m/s. Bottom panel: Backazimuth as a function of time, with a transparent red box at 13h52 08 January indicating the window length.

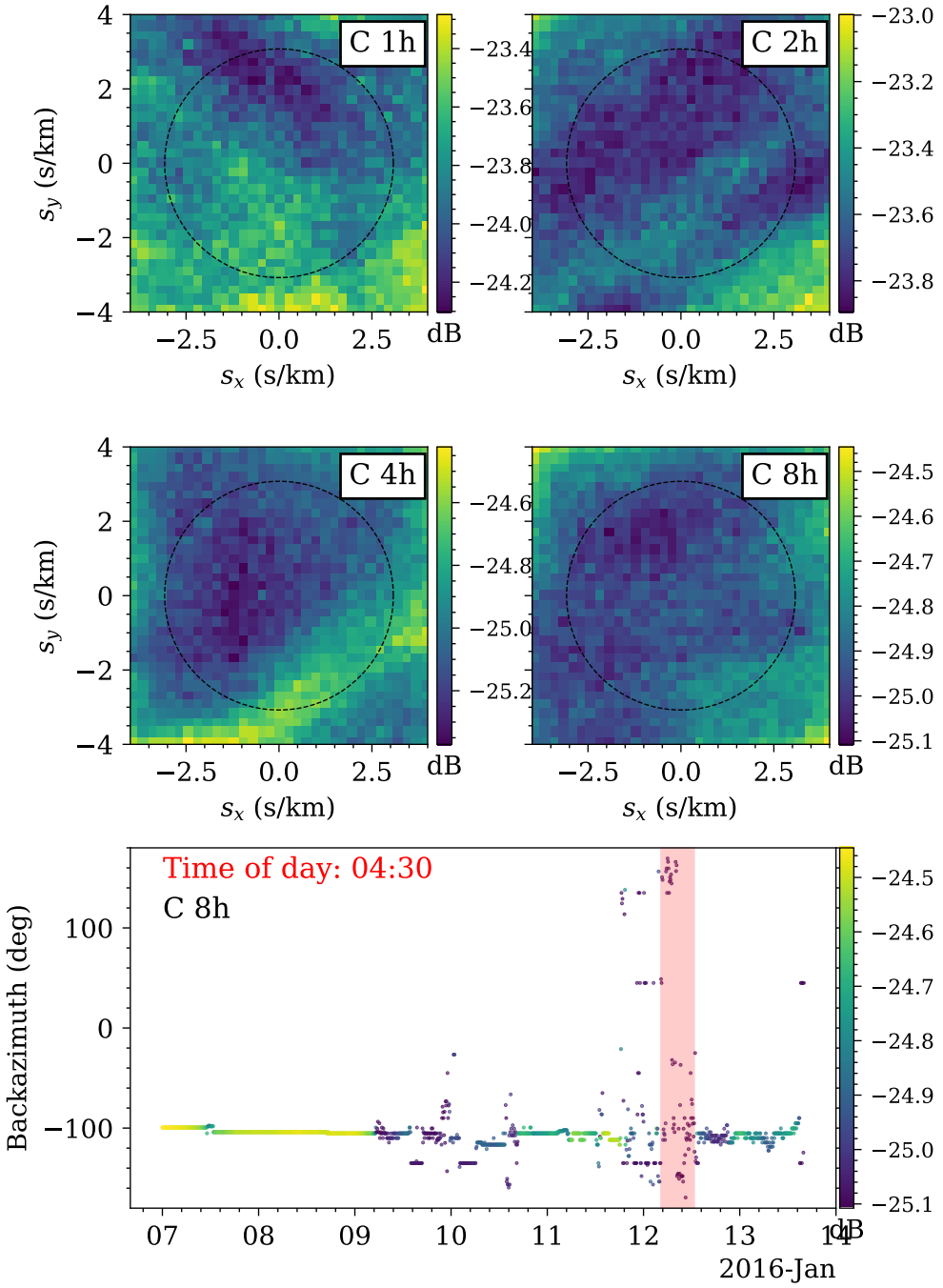

Figure 4.10: Same as in Figure 4.9, but the window length has been set to 04h30 12 January 2016.

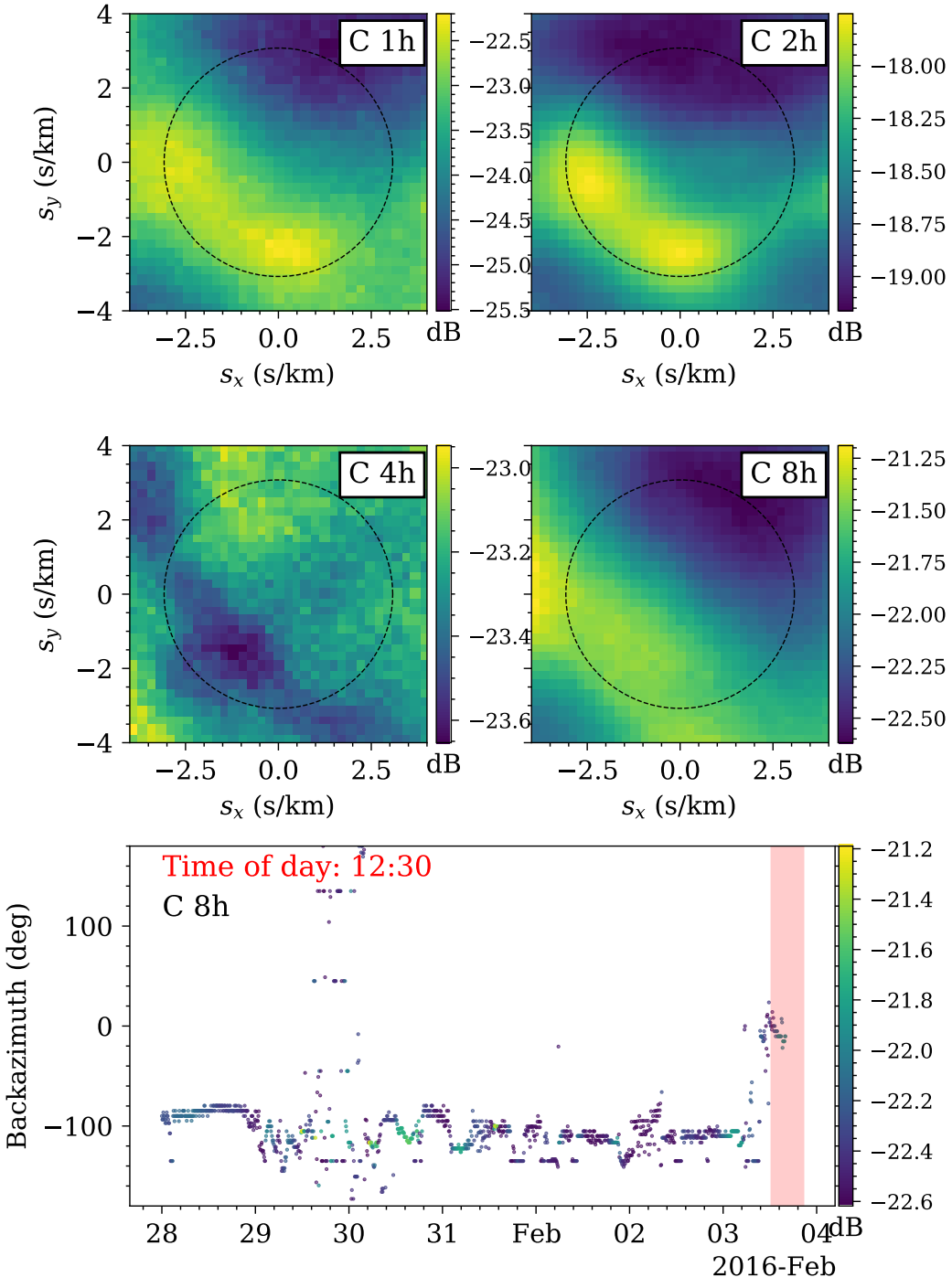

Figure 4.11: Same as in Figure 4.9, but the data display is from 28 January to 4 February and the window length has been set to 12h30 3 February 2016.

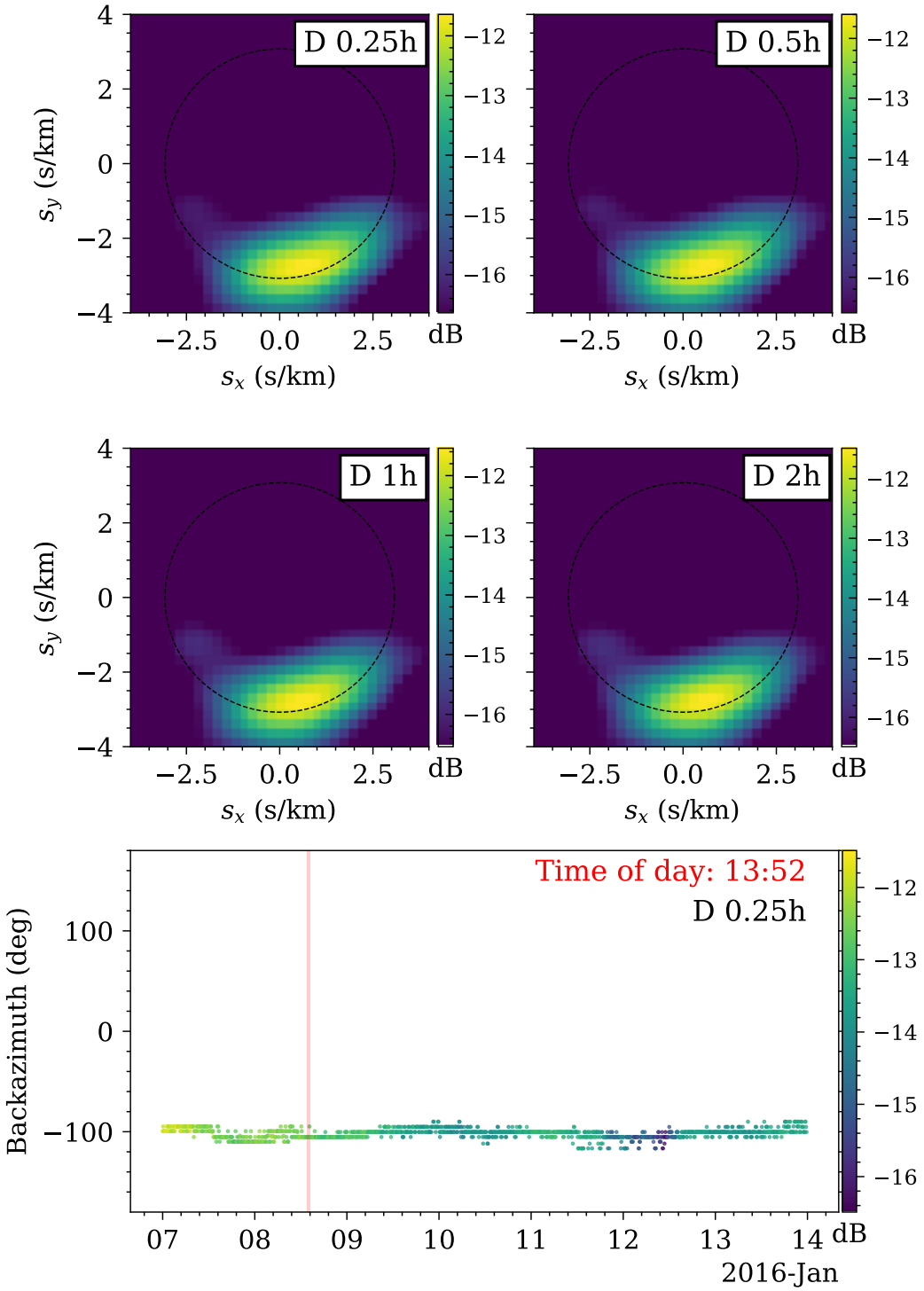

Figure 4.12: Same as in Figure 4.9, but estimations has been made using the delay-and-sum beamformer. The beamformer and window lengths are indicated in the upper right corner of each slowness plot.

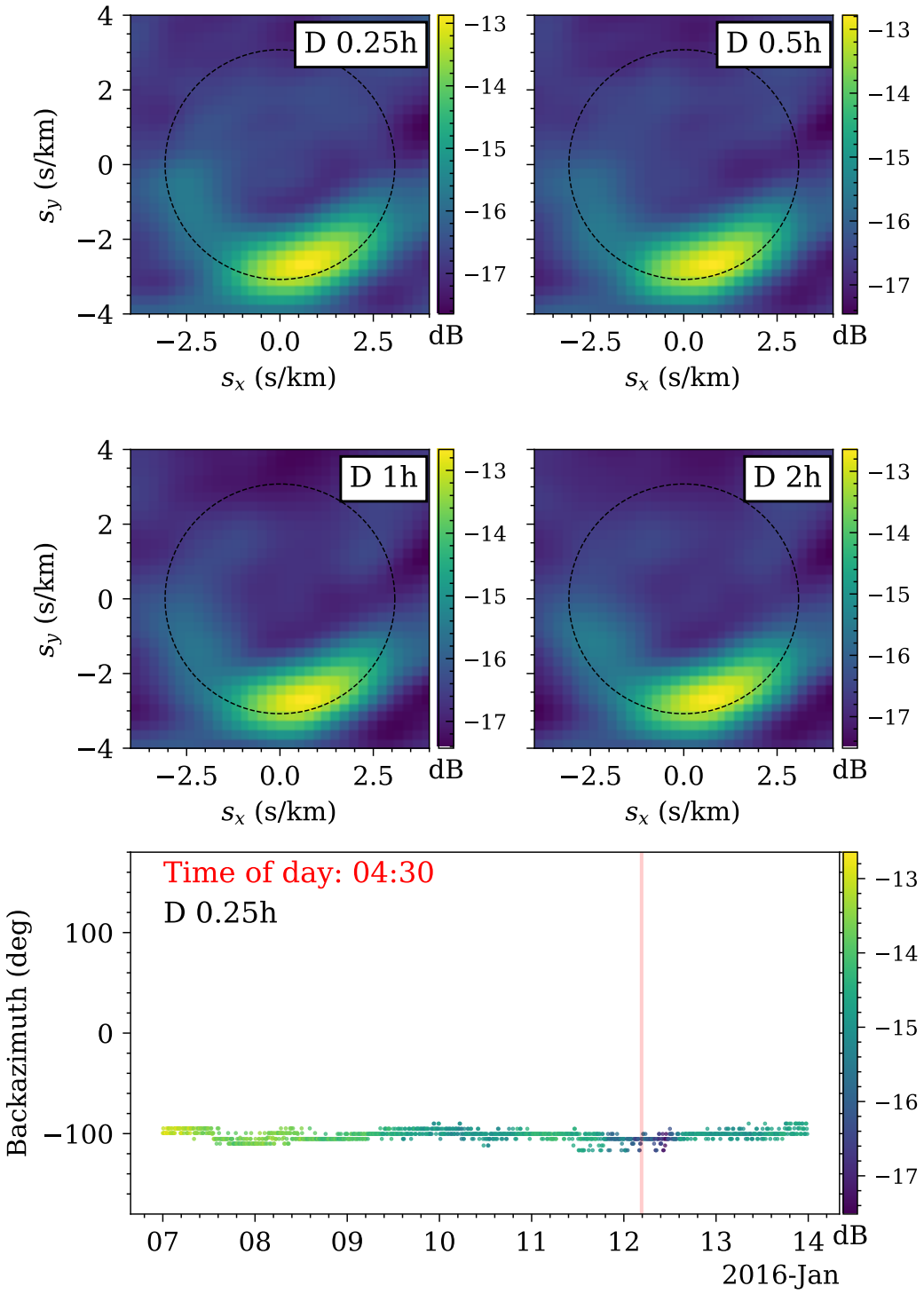

Figure 4.13: Same as in Figure 4.9, but estimations has been made using the delay-and-sum beamformer. The window lengths are indicated in the upper right corner of each slowness plot. Also the window length has been set to 04h30 12 January 2016.

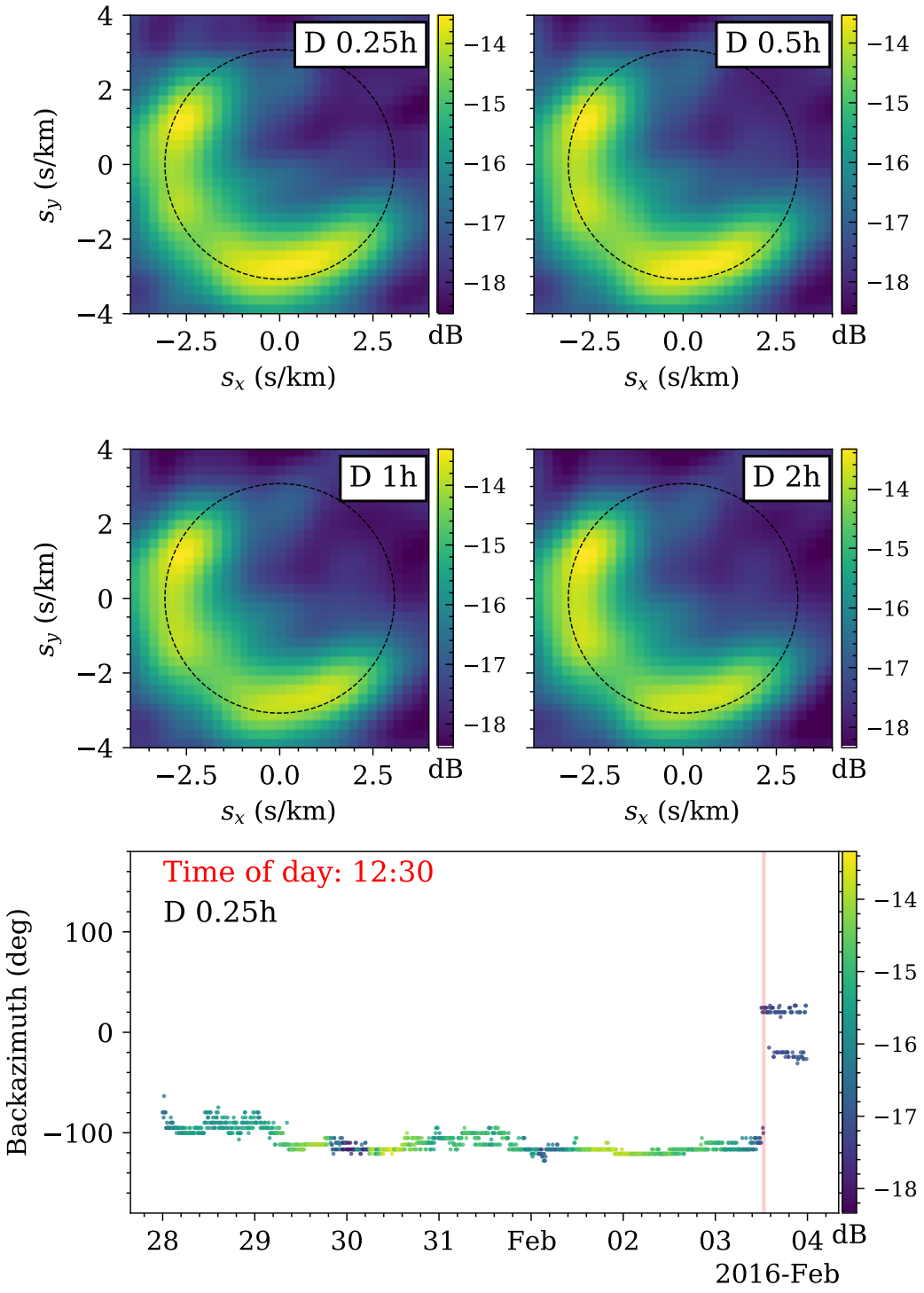

Figure 4.14: Same as in Figure 4.9, but estimations has been made using the delay-and-sum beamformer. With the window lengths indicated in the upper right corner of each slowness plot. Also the window length has been set to 12h30 3 February 2016.

tendency of more noise and lower resolution in the plots of longer window lengths. This is barely visible, but when considering the dominant source in Figure 4.11 and looking at the plots of a 15 minute window length and a 2 hour window length, it is easier to separate the two sources placed west in the plot for the plot using a 15 minute window length.

CHAPTER 5

Discussion

In this chapter, we consider the results of the Results chapter. Our main focus is on characterising a wavefield and how to optimise the parameters for estimating backazimuth and power maps viewed in slowness space. In addition, the study of the beamformer algorithm and the effects of window length on power maps will be discussed.

5.1 Comparing power maps from OKIF and IS37 Stream

Comparing the plots using the stream from the OKIF station and the IS37 station shows that the results are different. den Ouden, Assink, Smets, Shani-Kadmiel et al. (2020a) shows that the capability of detecting interfering signals comes down to the resolution of the beamforming. The resolution is quantified by the array response determined by the beamformer and the array outlay, which concludes that if the resolution is low, then the dominant source masks out other subdominant sources.

Considering Figure 3.4 using the delay-and-sum method on the OKIF dataset, we see that the number of different values in the backazimuth plot is limited. We also see large gaps between the angles. Considering the plot in slowness space, we see that the size of the dominant source is so big that it masks out potential other sources. Comparing this to the plots using the data from the IS37 station, we see that the resolution is higher. This indicates the difference from using the four-element array in the OKIF array to the IS37 array of 10 elements. This corresponds well to (den Ouden, Assink, Smets, Shani-Kadmiel et al., 2020a), that a short aperture provides a low resolution, while a longer aperture makes a higher resolution.

When we consider the plots of power maps shown in the slowness space, there are also differences in the results. Considering the power maps from the OKIF array station, we can see that the resolution is significantly higher when using Capon's method. In contrast, for the IS37 array station, we see that the resolution is higher when the delay-and-sum beamformer is used. Considering the intensities

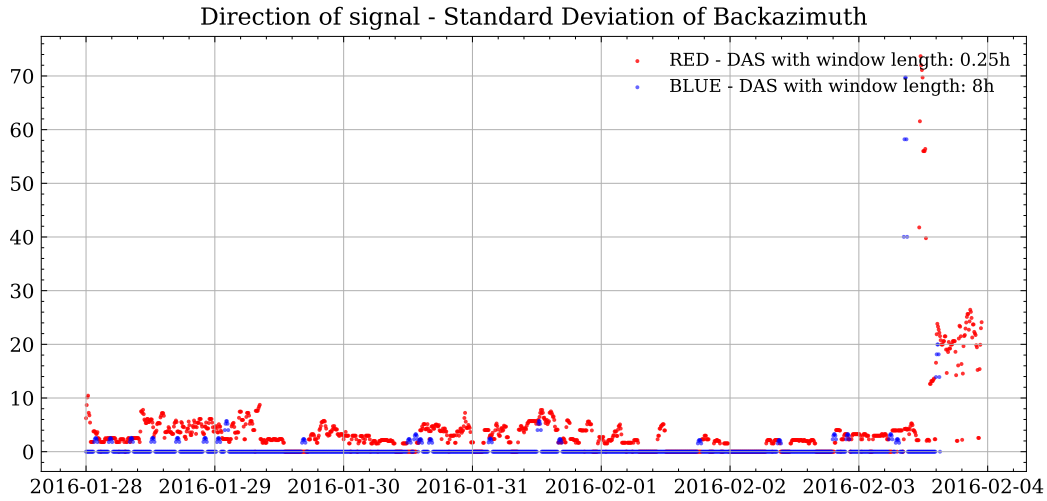

Figure 5.1: Plot of the standard deviation of the estimated backazimuth using delay-and-sum. The red dots display the estimates using a window length of 15 minutes, while the blue are for a window length of 8 hours.

in the slowness plots, we can see that the intensity is higher in the data from the OKIF array station. Hence, we suggest that the signal-to-noise ratio (SNR) is higher for the transient signal in the OKIF data, and building on this, the Capon's method performs better under such conditions.

Calculations of the Capon's method has been with the addition of prewhitening (see the diagonal loading subsection). An alternate of the Capon's method where some diagonal loading is applied. Since our calculations using this modification of Capon's method perform worse when considering microbaroms, in a later study we could try to add a heavier load of diagonal loading. Otherwise, the CLEAN alteration of the Capon's method could possibly yield better results, as it performs better in the presence of multiple sources(see, den Ouden, Assink, Smets, Shani-Kadmiel et al., 2020b).

5.2 Backazimuth plots

Starting with the delay-and-sum beamformer, we see that it is robust, as it gives consistent estimates of the backazimuth. This is also confirmed when one looks at the standard deviation of the backazimuth as estimated over a sliding window and plotted in Figure 5.1. We see that the standard deviation is higher when we apply a shorter window length, which indicates that this makes the beamformer more sensitive and therefore also detects potential competing signals from shorter or weaker sources, impinging from other directions.

When Capon's method is applied, Figure 5.2 displays the standard deviation of the backazimuth estimation evaluated over a sliding window. We can see similar traits as in the standard deviation plot for delay-and-sum, with the variation being

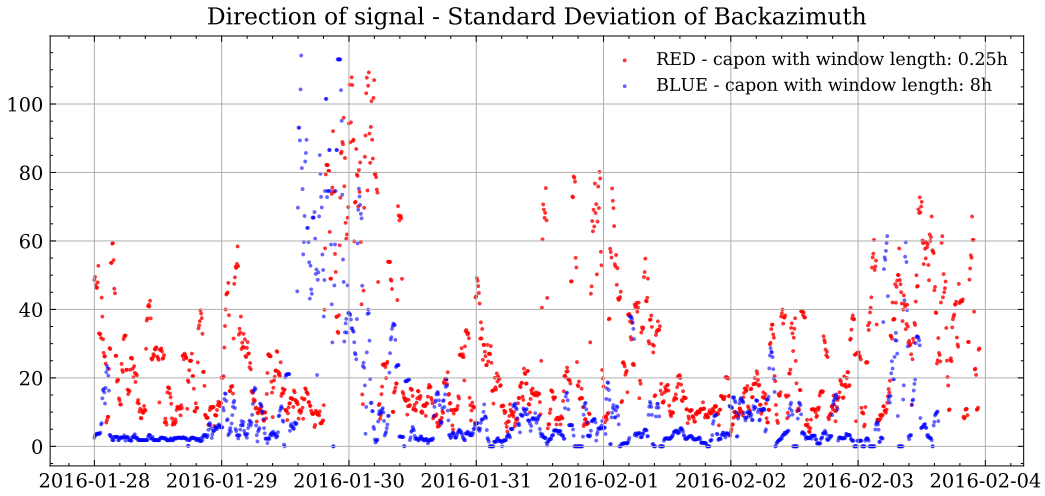

Figure 5.2: Same as Figure 5.1, but with the backazimuth estimated using Capon's method.

lower for longer window lengths. Comparing the two figures 5.1 and 5.2, we can note that the variance of the computation using Capon's method is significantly higher compared to that for the delay-and-sum beamformer. This illustrates that Capon's method is more sensitive. We can observe that it estimates the backazimuths corresponding to waves impinging a great variety of directions.

We tried to compensate for the sensitivity by changing the window length. For the delay-and-sum beamformer, we used a window length of 15 minutes, while on the Capon's method, we used a window length of 8 hours (can be seen in 4.2). In the figure, we can see that the variation between the two beamformers is more similar, but the Capon's method seems to be more sensitive to change in the direction of the incoming waves.

To further reduce the local variation in the backazimuth plot, we investigated the use of a rolling median of 7 samples, as seen in the figures of 4.3 – 4.7. This leads to a beneficial averaging effect with the addition of cancelling out potential outliers. The downside of the 7-sample rolling median is that some sensitivity is lost.

5.3 Slowness-space power map displays

After we have studied the backazimuth estimates generated using various window lengths for the two beamformers, we now investigate properties of the associated power maps in slowness space. The backazimuth (and apparent velocity) of the dominating wavefront is extracted by reading off these parameters from the point in slowness space where the beamformer output power is maximised.

We have chosen three-time particular time instances of interest where the impinging wavefields are of different character. The first chosen instance was on

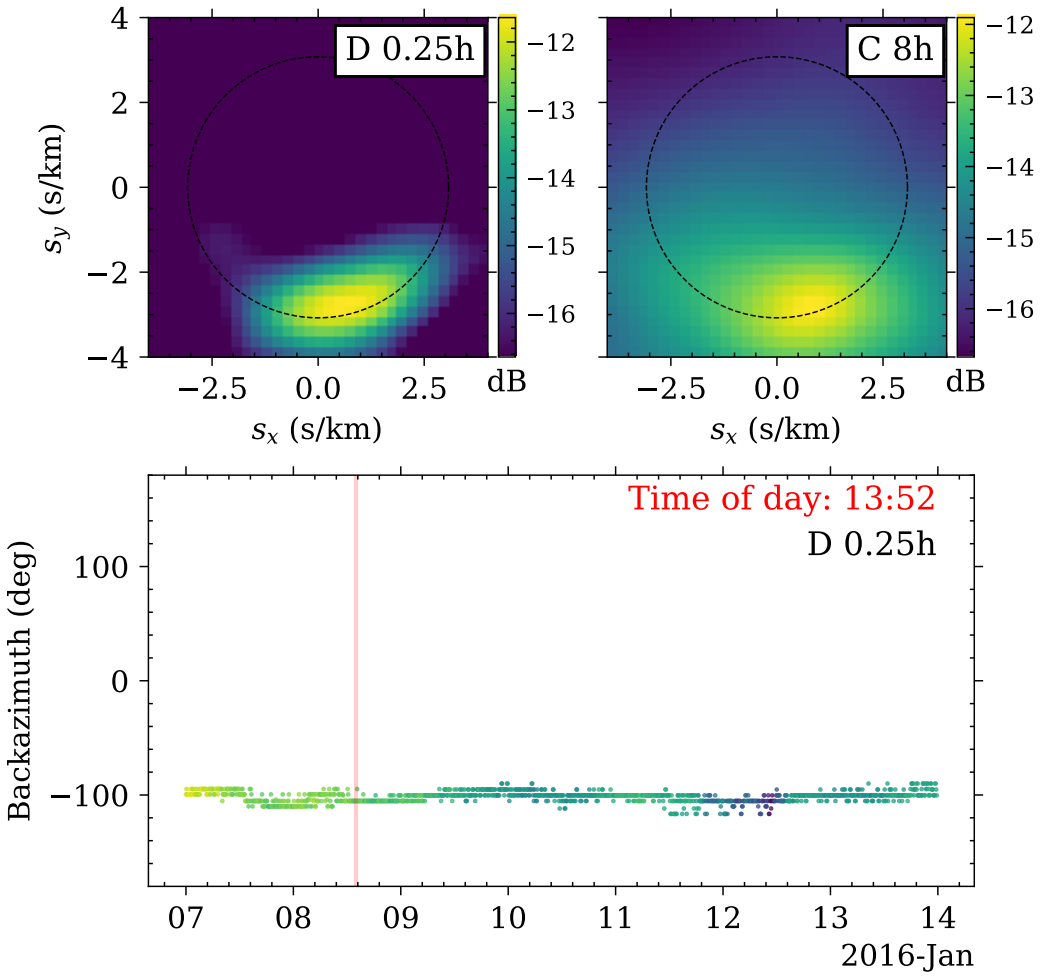

Figure 5.3: IS37 station data display from 7 January to 14 January 2016. Upper left: Slowness space plots of power map computed with the delay-and-sum beamformer using a window length of 0.25 hours.
Upper right: Slowness space plots of power map computed with the Capon's method using a window length of 8 hours.
Lower plot: Backazimuth computed with the delay-and-sum beamformer with a window length of 0.25 hours.

8 January 2016, with the displayed results corresponding to a data window that started at 13h52. The second timeframe of interest that is displayed is on 12 January 2016, with the data window starting at 04h30. The last timeframe of interest is on 3 February 2016, with the data window starting at 12h30. For these three time frames of interest, we have displayed the corresponding power maps in the slowness space in Figures 5.3, 5.4 and 5.5. These time frames of interest were also included in the earlier figures displaying power maps in slowness space.

The plots displayed comprise only a subset of the displays assessed and considered in the processing time window analysis. From all window lengths

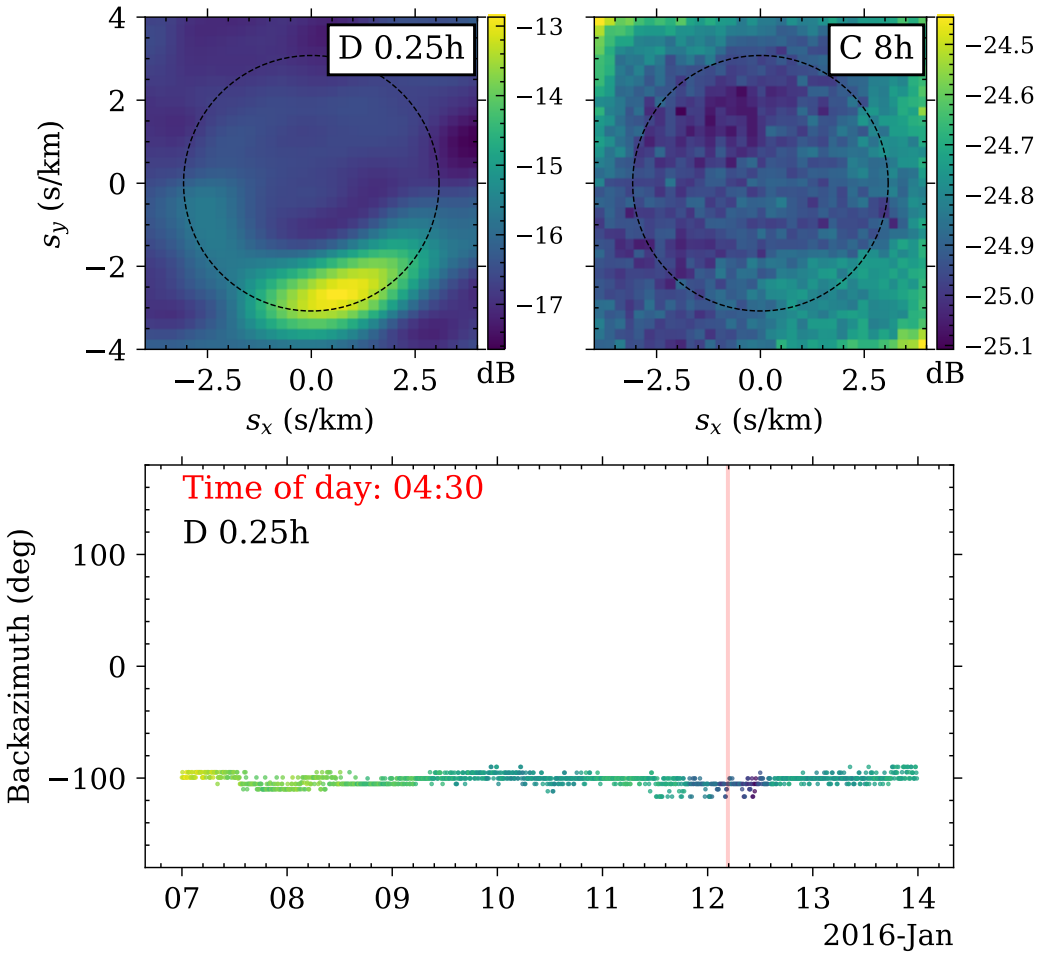

Figure 5.4: Same as in Figure 5.3, but with the window length set to 12h30 at 04h30 12 February 2016.

tested out, we have picked out what appear to be beneficial choices of window lengths, when studying the resulting backazimuth estimate patterns and variations. Thus, we conclude that the delay-and-sum beamformer gives more reliable estimates for a window length of 15 minutes. For the Capon's method related window length, we have assessed that a longer window length is beneficial in order to get a more robust result. Hence, we find that, for processing this kind of data at this station, the delay-and-sum estimation of the backazimuth appears to be the preferred choice.

We are also interested in assessing how well a beamformer can detect abrupt changes in the arriving microbarom signal structure, and whether it can handle a case with two signals from different directions of arrival. First, we consider Capon's method with a window length of one up to 8 hours. In the upper right panel of Figure 5.3, we can study a slowness plot that shows a single clear direction-of-arrival. We can consider this to be an appropriate resolution for these kinds of microbarom waves, since the "mainlobe blob" is distinct and clear. Moreover, the

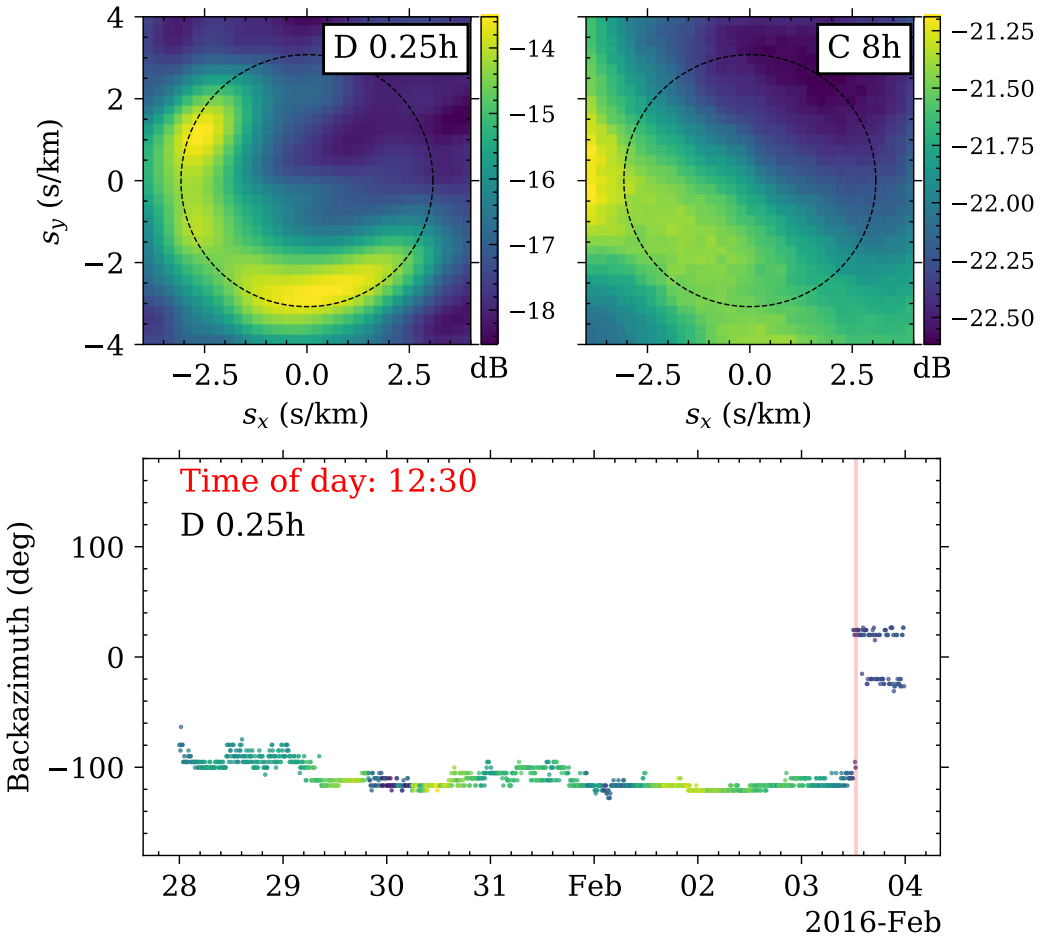

Figure 5.5: Same as in Figure 5.3, but from 28 January to 4 February 2016. With the window length set to 12h30 at 3 February 2016.

rest of the display does not indicate many traits of disturbing noise. In the upper left panel of the same figure, we display the power maps resulting from applying the delay-and-sum beamformer. This looks similar to the slowness plot using Capon's method, although the size of the incoming signal mainlobe blob has more contrast relative to the background, and the lobe follows a circle indicated at the horizontal slowness amplitude corresponding to the local speed of sound. There are also some signs of another source impinging at the same time. We did not see this pattern from the estimates using Capon's method, plotted in the upper right of the same figure.

Taking into account the second time period of interest, perform a similar analysis. That is, we compare the two beamformers but now for the time frame on 12 January 2016. Using the Capon's method, plotted in the upper right in Figure 5.4. Recall that in the lower plot of Figure 4.10, we can see the corresponding estimated backazimuth time series. Therefore, we have selected an instance in time where there was a lot of variation in the direction-of-arrival. Note that when

considering this time frame, and for outputs computed with the delay-and-sum beamformer, we can study the lower plot of Figure 4.13. The direction-of-arrival from the dominant signal does not vary, unlike the calculations using Capon's method for the same time period. To evaluate whether Capon's method picks up another source, we inspect a power map in slowness space corresponding to this time period. This can potentially indicate whether there is a change in direction of the most dominant signal or whether there are multiple competing incoming waves.

After analysing the slowness plots in the upper left of Figure 5.4, we note that the estimates seem noisy, without a strong indication of a dominant wavefront. This plot certainly does not look like the previously displayed slowness plot in the upper right panel of Figure 5.3, which has a distinct peak. More likely, for this period there is a presence of incoherent noise, like transient infrasound or prospectively local turbulence at the array station, that makes the Capon's method perform worse. Later studies could investigate local conditions using local weather stations, etc.

Comparing the second time period of interest and the delay-and-sum beamformer power map in slowness space, we interpret the following: We still find the maximum in a similar area as in Figure 5.3(upper left), but we note that there is another weak source that contributes with power on the left side of the slowness plot. Considering the colour variations in the plot in the time series, which shows the power peak in slowness of the incoming infrasound, the intensity is lower, compared to the more common power within the plotted time period. This could be an indication that Capon's method performs worse when the infrasound source is weaker, i.e. when the microbarom signal-to-noise ratio is lower.

Investigating the third time period of interest, we find a time instance where both beamformers give a change in backazimuth. This time instance was investigated in a similar way to the other two time frames of interest and is shown in Figure 5.5. As presented in 4.2, the setting with the most decent output quality for this case was with a window length of two hours. We can take into account that the peak intensity of the power map was located inside the dotted line (334 m/s apparent velocity). This indicates that the dominant incoming wave has an apparent velocity considerably higher than in the normal state.

Examining the maximum power in slowness space, which can be read from the dB-scale of the plots, we note that the one with a more distinguished peak and clear output corresponds to a time period with a higher peak power. When comparing the intensity of these slowness plots in Figure 5.3, which has a significantly more robust output, we can see that those plots are much higher in power at the maximum. Similarly, in Figure 4.10, the plots have low power and show a less distinctive signature. Hence, a suggestion could be that Capon's method performs better in an environment where the dominant incoming signals are of high power since we have a higher signal-to-noise ratio. Otherwise, various infrasound sources, such as other strong microbaroms, will affect the beamforming output characteristics.

Considering the third time period of interest processed with the delay-and-sum

beamformer, displayed in the slowness space in the upper left panel of Figure 5.5, we note that there are multiple sources resolved resolution. In these slowness plots, we can see two or maybe even more than two groups of arrivals of similar intensity. These are more straightforward to assess with a lower window length so that it can be distinguished whether the source complex components are separated in time or not.

Considering the collection of slowness plots, the results indicate that the output of the delay-and-sum beamformer is more suited for microbarom wavefield assessment. Also, we note that Capon's method produces less stable output for several of the investigated cases. It seems that the Capon's method is too sensitive to the various noise contributions on the IS37 array. These results are in line with Capon (1969) where it is stated that the beamformer benefits from a low amount of incoherent background noise.

5.4 Reflections on the processing stepsize

In these computations, we used window lengths that overlap from 50% up to 98.4% for the longest window length. This means that when we compute power maps, there are overlapping samples between the multiple calculations. When we doubled the window length, we reduced the window fraction by half. By doing this, we obtained a similar number of power maps when using a window length of 8 hours, compared to the number of power maps we obtained when using a window length of 15 minutes, and this can facilitate comparisons. The same goes for the number of datapoints when we found the backazimuth with different window lengths.

A benefit of this is that when plotting the backazimuth, we had the same number of datapoints, making it easier to plot two different plots in one figure. Also, because we have a higher number of datapoints, we have plots that were more straightforward to interpret with enough points to visually assess how the estimates change over time. However, this naturally involved a higher computational burden to produce these outputs compared to a more critically sampled case. This could potentially be a trade-off factor when studying a long time period, as we did in this study. For example, computing an out signal for one week with a window length of 8 hours and a window fraction of 0.5/32 takes close to two hours to process. This is a considerable amount of time, compared to the calculations on the OKIF infrasound data with a stream of 20 minutes. In these computations, we used around 10 seconds, in total, for all 4 window lengths ranging from $5 - 60$ seconds.

CHAPTER 6

Conclusions and further work

6.1 Conclusions

In this study, we have investigated different temporal window lengths and beamforming techniques to estimate the direction-of-arrival of microbarom infrasound wavefronts. We applied both Capon's method and the delay-and-sum beamformer. It should be noted that Capon's method without prewhitening performed poorly, and hence all computations using this method had a prewhitening applied. This means that a diagonal loading has been applied to the correlation matrix.

For the IS37 array station calculations using Capon's method, with the prewhitening applied, the results gave for the most parts worse resolution than the delay-and-sum beamformer. This has been a surprising element in this study. An additional further study of this would be interesting to investigate the local conditions that affect the results. It would also be interesting to see how the CLEAN beamformer (an alteration of Capon's method) would perform, since it performs better when multiple incoming sources are present (den Ouden, Assink, Smets, Shani-Kadmiel et al., 2020b).

We evaluated the effect of various window lengths for each of the beamformers. This was done via an evaluation of the resulting time development of the dominating wavefront backazimuth direction-of-arrival estimation, extracted from the maximum peak of the power map in slowness space as produced by the beamformers, given a selected window length.

To build an intuition about properties of infrasound datasets and their processing, we started out with a smaller project where we processed an infrasound array data stream containing a transient signal from a volcano eruption. From this we built a framework to process longer streams of infrasound data and predicted the direction-of-arrival from microbaroms.

Subsequently, we considered a stream of several winter months of infrasound recorded from an infrasound array, IS37 at Bardufoss, northern Norway. We performed extensive experimentation with computations of power maps over horizontal slowness grids, using varying window lengths both for the Capon and delay-and-sum beamformers. Each processing setting results in a separate time

series of backazimuth towards the dominating microbarom wavefront.

Evaluating the visualisation of these results, we found that the Capon's method was sensitive to the present incoherent noise. Therefore, the method benefits from using a longer window length as the variance is reduced. The delay-and-sum beamformer was found to be more robust and handled incoherent noise much better. Due to the robustness, we found that we can use shorter window lengths while still maintaining a reliable backazimuth estimate. This approach is also less computationally demanding and hence requires less processing time. Using shorter window lengths also helps to pick up changes in signals faster, and there is also a chance of noticing smaller changes in the incoming wavefield. Therefore, based on the results from the IS37 array station, we suggest using the delay-and-sum beamformer with a window length of 15 minutes.

6.2 Suggestions for further study

For future work, it would be interesting to see additional flavours of adaptive beamformers implemented, in particular, if they can be further tuned to the microbarom context. This could be, as an example, combined with the CLEAN beamformer iterative processing (den Ouden, Assink, Smets, Shani-Kadmiel et al., 2020b), which addresses the challenges of separating the directional peaks of interfering signals, which are not necessarily distinguishable directly from the power maps output using Capon's method. The CLEAN beamformer is constructed to iterative select the maximum of the f-k-spectra, and then remove a percentage of the corresponding signal from the cross-spectral density matrix.

It would also be interesting to study post-processing filters for noise reduction, to see how they could affect the plot of the power maps in slowness space.

Moreover, assessing the reliability of beamformers and processing settings for microbaroms could be facilitated if it was combined with an appropriate modelling of the microbarom soundscape. This can be done with the support of specialised microbarom source and wave propagation modelling (see, for example, De Carlo, Ardhuin and Le Pichon (2020), De Carlo, Hupe et al. (2021), Vorobeva et al. (2021) and Ouden et al. (2021)). It is also worth underlining that a combination of the output from microbarom wavefield modelling with processed infrasound array data recordings will probably be key components in a prospective future assimilation to enhance atmospheric models. Ideally, such frameworks would include an analysis of datasets from global networks of infrasound stations and not single-station assessments, as in the current study.

Bibliography

Ahern, Tim, Casey, Rob, Barnes, Deborah, Benson, R and Knight, T (2012). "SEED Reference Manual–Standard for the Exchange of Earthquake Data". In: *International Federation of Digital Seismograph Networks Incorporated Research Institutions for Seismology United States Geological Survey, version* vol. 2.

Amezcua, Javier and Barton, Zak (2021). "Assimilating atmospheric infrasound data to constrain atmospheric winds in a two-dimensional grid". In: *Quarterly Journal of the Royal Meteorological Society* vol. 147, no. 740, pp. 3530–3554. DOI: 10.1002/qj.4141.

Amezcua, Javier, Näsholm, Sven Peter, Blixt, Erik Mårten and Charlton-Perz, Andrew J (2020). "Assimilation of atmospheric infrasound data to constrain tropospheric and stratospheric winds". In: *Quarterly Journal of the Royal Meteorological Society* vol. 146, no. 731, pp. 2634–2653. DOI: 10.1002/qj.3809.

Assink, J. D. (2013). "Infrasound as Upper Atmospheric Monitor". PhD thesis. University of Mississippi. ISBN: 9781493555321.

Assink, Jelle, Smets, Pieter, Marcillo, Omar, Weemstra, Cornelis, Lalande, Jean-Marie, Waxler, Roger and Evers, Läslo (2019). "Advances in infrasonic remote sensing methods". In: *Infrasound Monitoring for Atmospheric Studies: Challenges in Middle Atmosphere Dynamics and Societal Benefits*, pp. 605–632. DOI: 10.1007/978-3-319-75140-5_18.

Baldwin, Mark P and Dunkerton, Timothy J (2001). "Stratospheric harbingers of anomalous weather regimes". In: *Science* vol. 294, no. 5542, pp. 581–584. DOI: 10.1126/science.1063315.

Baldwin, Mark P., Ayarzagüena, Blanca, Birner, Thomas, Butchart, Neal, Butler, Amy H., Charlton-Perez, Andrew J., Domeisen, Daniela I. V., Garfinkel, Chaim I., Garny, Hella, Gerber, Edwin P., Hegglin, Michaela I., Langematz, Ulrike and Pedatella, Nicholas M. (2021). "Sudden Stratospheric Warmings". In: *Reviews of Geophysics* vol. 59, no. 1. e2020RG000708 10.1029/2020RG000708, e2020RG000708. DOI: https://doi.org/10.1029/2020RG000708. eprint: https://agupubs.onlinelibrary.wiley.com/doi/pdf/10.1029/2020RG000708.

Benioff, Hugo and Gutenberg, Beno (1939). "Waves and currents recorded by electromagnetic barographs". In: *Bulletin of the American Meteorological Society* vol. 20, no. 10, pp. 421–428. DOI: 10.1175/1520-0477-20.10.421.

Bishop, Jordan W, Fee, David and Szuberla, Curt AL (2020). "Improved infrasound array processing with robust estimators". In: *Geophysical Journal International* vol. 221, no. 3, pp. 2058–2074. DOI: 10.1093/gji/ggaa110.

Blanc, Elisabeth, Pol, Katy, Le Pichon, Alexis, Hauchecorne, Alain, Keckhut, Philippe, Baumgarten, Gerd, Hildebrand, Jens, Höffner, Josef, Stober, Gunter, Hibbins, Robert et al. (2019). "Middle atmosphere variability and model uncertainties as investigated in the framework of the ARISE project". In: *Infrasound Monitoring for Atmospheric Studies: Challenges in Middle Atmosphere Dynamics and Societal Benefits*, pp. 845–887. DOI: 10.1007/978-3-319-75140-5_28.

Blixt, Erik Mårten, Näsholm, Sven Peter, Gibbons, Steven J, Evers, Läslo G, Charlton-Perez, Andrew J, Orsolini, Yvan J and Kværna, Tormod (2019). "Estimating tropospheric and stratospheric winds using infrasound from explosions". In: *The Journal of the Acoustical Society of America* vol. 146, no. 2, pp. 973–982. DOI: 10.1121/1.5120183.

Brachet, Nicolas, Brown, David, Bras, Ronan Le, Cansi, Yves, Mialle, Pierrick and Coyne, John (2010). "Monitoring the Earth's atmosphere with the global IMS infrasound network". In: *Infrasound monitoring for atmospheric studies*. Springer, pp. 77–118. DOI: 10.1007/978-1-4020-9508-5_3.

Brekhovskikh, L M, Goncharov, V V, Kurtepov, V M and Naugolny, K A (1973). "Radiation of infrasound into atmosphere by surface-waves in ocean". In: *Izvestiya Akademii Nauk SSSR Fizika Atmosfery i Okeana* vol. 9, no. 9, pp. 899–907.

Butchart, Neal (2022). "The stratosphere: a review of the dynamics and variability". In: *Weather and Climate Dynamics* vol. 3, no. 4, pp. 1237–1272. DOI: 10.5194/wcd-3-1237-2022.

Butler, A. H., Sjoberg, J. P., Seidel, D. J. and Rosenlof, K. H. (2017). "A sudden stratospheric warming compendium". In: *Earth System Science Data* vol. 9, no. 1, pp. 63–76. DOI: 10.5194/essd-9-63-2017.

Capon, Jack (1969). "High-resolution frequency-wavenumber spectrum analysis". In: *Proceedings of the IEEE* vol. 57, no. 8, pp. 1408–1418. DOI: 10.1109/PROC.1969.7278.

Christie, Douglas R. and Campus, Paola (2009). "The IMS infrasound network: Design and establishment of infrasound stations". In: *Infrasound monitoring for atmospheric studies*, pp. 29–75. DOI: 10.1007/978-1-4020-9508-5_2.

Dahlman, Ola, Mackby, Jenifer, Mykkeltveit, Svein and Haak, Hein (2011). *Detect and deter: can countries verify the nuclear test ban?* Springer Science & Business Media. DOI: 10.1007/978-94-007-1676-6.

Daniels, Fred B (1952). "Acoustical energy generated by the ocean waves". In: *The Journal of the Acoustical Society of America* vol. 24, no. 1, pp. 83–83. DOI: 10.1121/1.1906855.

De Carlo, Marine, Ardhuin, Fabrice and Le Pichon, Alexis (2020). "Atmospheric infrasound generation by ocean waves in finite depth: unified theory and

application to radiation patterns". In: *Geophysical Journal International* vol. 221, no. 1, pp. 569–585. DOI: 10.1093/gji/ggy520.

De Carlo, Marine, Hupe, Patrick, Le Pichon, Alexis, Ceranna, Lars and Ardhuin, Fabrice (2021). "Global microbarom patterns: A first confirmation of the theory for source and propagation". In: *Geophysical Research Letters* vol. 48, no. 3, e2020GL090163. DOI: 10.1029/2020GL090163.

De Carlo, Marine, Le Pichon, Alexis, Ardhuin, Fabrice and Näsholm, Sven Peter (2018). In: *NNC RK Bull* vol. 2, pp. 144–151.

den Ouden, Olivier F C, Assink, Jelle D, Smets, Pieter S M, Shani-Kadmiel, Shahar, Averbuch, Gil and Evers, Läslo G (Jan. 2020a). "CLEAN beamforming for the enhanced detection of multiple infrasonic sources". In: *Geophysical Journal International* vol. 221, no. 1, pp. 305–317. ISSN: 0956-540X. DOI: 10.1093/gji/ggaa010. eprint: https://academic.oup.com/gji/article-pdf/221/1/305/32291191/ggaa010.pdf.

den Ouden, Olivier FC, Assink, Jelle D, Smets, Pieter SM and Evers, Läslo G (2022). "A climatology of microbarom detections at the Kerguelen Islands: unravelling the ambient noise wavefield". In: *Geophysical Journal International*. DOI: 10.1093/gji/ggab535.

den Ouden, Olivier FC, Assink, Jelle D, Smets, Pieter SM, Shani-Kadmiel, Shahar, Averbuch, Gil and Evers, Läslo G (2020b). "CLEAN beamforming for the enhanced detection of multiple infrasonic sources". In: *Geophysical Journal International* vol. 221, no. 1, pp. 305–317. DOI: 10.1093/gji/ggaa010.

Domeisen, Daniela IV, Butler, Amy H, Charlton-Perez, Andrew J, Ayarzagüena, Blanca, Baldwin, Mark P, Dunn-Sigouin, Etienne, Furtado, Jason C, Garfinkel, Chaim I, Hitchcock, Peter, Karpechko, Alexey Yu et al. (2020). "The role of the stratosphere in subseasonal to seasonal prediction: 2. Predictability arising from stratosphere-troposphere coupling". In: *Journal of Geophysical Research: Atmospheres* vol. 125, no. 2, e2019JD030923. DOI: 10.1029/2019JD030920.

Donn, William L and Rind, David (1971). "Natural infrasound as an atmospheric probe". In: *Geophysical Journal International* vol. 26, no. 1-4, pp. 111–133. DOI: 10.1111/j.1365-246X.1971.tb03386.x.

Donn, William L. and Posmentier, Eric S. (1967). "Infrasonic Waves from the Marine Storms of April 7, 1966". In: *Journal of Geophysical Research*. DOI: 10.1029/JZ072i008p02053.

Earth Nullschool visualization of global weather conditions (Apr. 2023). URL: https://earth.nullschool.net (visited on 04/2023).

Evers, Läslo G. and Haak, Hein W. (2010). "The characteristics of infrasound, its propagation and some early history". In: *Infrasound monitoring for atmospheric studies*. Springer, pp. 3–27. DOI: 10.1007/978-1-4020-9508-5_1.

Fricke, Julius Tobias, Evers, Läslo G., Smets, Pieter S. M., Wapenaar, Kees and Simons, D. G. (2014). "Infrasonic interferometry applied to microbaroms observed at the Large Aperture Infrasound Array in the Netherlands". In: *Journal of Geophysical Research: Atmospheres* vol. 119, no. 16, pp. 9654–9665. DOI: 10.1002/2014JD021663.

Fyen, Jay, Roth, Michael and Larsen, Paal W. (2014). "IS37 Infrasound Station in Bardufoss, Norway". In: *NORSAR Scientific Report*, no. 2-2013, pp. 29–39.

Gal, Martin, Reading, Anya M., Ellingsen, S. P., Koper, Keith D., Gibbons, Steven J. and Näsholm, Sven Peter (2014). "Improved implementation of the fk and Capon methods for array analysis of seismic noise". In: *Geophysical Journal International* vol. 198, no. 2, pp. 1045–1054. DOI: 10.1093/gji/ggu183.

Garcés, Milton, Willis, Mark, Hetzer, Claus, Le Pichon, Alexis and Drob, Douglas (2004). "On using ocean swells for continuous infrasonic measurements of winds and temperature in the lower, middle, and upper atmosphere". In: *Geophysical research letters* vol. 31, no. 19. DOI: 10.1029/2004GL020696.

Gibbons, Steven, Kværna, Tormod and Näsholm, Peter (2019). "Characterization of the infrasonic wavefield from repeating seismo-acoustic events". In: *Infrasound Monitoring for Atmospheric Studies*. Springer, pp. 387–407. DOI: 10.1007/978-3-319-75140-5_10.

Gibbons, Steven J., Asming, Vladimir, Eliasson, Lars, Fedorov, Andrey, Fyen, Jan, Kero, Johan, Kozlovskaya, Elena, Kvaerna, Tormod, Liszka, Ludwik, Näsholm, Sven Peter, Raita, Timo, Roth, Michael, Tiira, Timo and Vinogradov, Yuri (2015). "The European Arctic: A Laboratory for Seismoacoustic Studies". In: *Seismological Research Letters* vol. 86, no. 3, pp. 917–928. DOI: 10.1785/0220140230.

Grythe, Jørgen (2015). "Beamforming algorithms-beamformers". In: *Technical Note, Norsonic AS, Norway*.

Johnson, Don H and Dudgeon, Dan E (1992). *Array signal processing: concepts and techniques*. Simon & Schuster, Inc.

Kolstad, Erik W, Lee, Simon Haydn, Butler, Amy Hawes, Domeisen, Daniela IV and Wulff, C. Ole (2022). "Diverse surface signatures of stratospheric polar vortex anomalies". In: *Journal of Geophysical Research: Atmospheres* vol. 127, no. 20, e2022JD037422. DOI: 10.1029/2022JD037422.

Krim, Hamid and Viberg, Mats (1996). "Two decades of array signal processing research: the parametric approach". In: *IEEE signal processing magazine* vol. 13, no. 4, pp. 67–94. DOI: 10.1109/79.526899.

Krischer, Lion, Megies, Tobias, Barsch, Robert, Beyreuther, Moritz, Lecocq, Thomas, Caudron, Corentin and Wassermann, Joachim (2015). "ObsPy: A bridge for seismology into the scientific Python ecosystem". In: *Computational Science & Discovery* vol. 8, no. 1, p. 014003. DOI: 10.1088/1749-4699/8/1/014003.

Landès, Matthieu, Le Pichon, Alexis, Shapiro, Nikolai M, Hillers, Gregor and Campillo, Michel (2014). "Explaining global patterns of microbarom observations with wave action models". In: *Geophysical Journal International* vol. 199, no. 3, pp. 1328–1337. DOI: 10.1093/gji/ggu324.

Le Bras, Ronan, Arora, Nimar, Kushida, Noriyuki, Mialle, Pierrick, Bondár, Istvan, Tomuta, Elena, Alamneh, Fekadu Kebede, Feitio, Paulino, Villarroel, Marcela, Vera, Beatriz, Sudakov, Alexander, Laban, Shaban, Nippress, Stuart, Bowers, David, Russell, Stuart and Taylor, Tammy (July 2021). "NET-VISA from

Cradle to Adulthood. A Machine-Learning Tool for Seismo-Acoustic Automatic Association". In: *Pure and Applied Geophysics* vol. 178, no. 7, pp. 2437–2458. ISSN: 1420-9136. DOI: 10.1007/s00024-020-02508-x.

Le Pichon, Alexis, Blanc, Elisabeth and Hauchecorne, Alain (2009). *Infrasound Monitoring for Atmospheric Studies*. Springer, p. 735. DOI: 10.1007/978-1-4020-9508-5.

Le Pichon, Alexis, Ceranna, Lars, Garcés, Milton, Drob, Douglas and Millet, Christophe (2006). "On using infrasound from interacting ocean swells for global continuous measurements of winds and temperature in the stratosphere". In: *Journal of Geophysical Research: Atmospheres* vol. 111, no. D11. DOI: 10.1029/2005JD006690.

Lee, Christopher, Smets, Pieter, Charlton-Perez, Andrew, Evers, Läslo, Harrison, Giles and Marlton, Graeme (2019). "The potential impact of upper stratospheric measurements on sub-seasonal forecasts in the extra-tropics". In: *Infrasound Monitoring for Atmospheric Studies: Challenges in Middle Atmosphere Dynamics and Societal Benefits*, pp. 889–907. DOI: 10.1007/978-3-319-75140-5_29.

Lyons, John J, Iezzi, Alexandra M, Fee, David, Schwaiger, Hans F, Wech, Aaron G and Haney, Matthew M (2020). "Infrasound generated by the 2016–2017 shallow submarine eruption of Bogoslof volcano, Alaska". In: *Bulletin of Volcanology* vol. 82, pp. 1–14. DOI: 10.1007/s00445-019-1355-0.

Manney, Gloria L and Lawrence, Zachary D (2016). "The major stratospheric final warming in 2016: dispersal of vortex air and termination of Arctic chemical ozone loss". In: *Atmospheric Chemistry and Physics* vol. 16, no. 23, pp. 15371–15396. DOI: 10.5194/acp-16-15371-2016.

Marcillo, Omar, Arrowsmith, Stephen, Charbit, Maurice and Carmichael, Joshua (2019). "Infrasound signal detection: re-examining the component parts that makeup detection algorithms". In: *Infrasound Monitoring for Atmospheric Studies: Challenges in Middle Atmosphere Dynamics and Societal Benefits*, pp. 249–271. DOI: 10.1007/978-3-319-75140-5_7.

Marty, Julien (2019). "The IMS infrasound network: current status and technological developments". In: *Infrasound Monitoring for Atmospheric Studies: Challenges in Middle Atmosphere Dynamics and Societal Benefits*, pp. 3–62. DOI: 10.1007/978-3-319-75140-5_1.

Mialle, Pierrick, Brown, David, Arora, Nimar and IDC, colleagues from (2019). "Advances in operational processing at the international data centre". In: *Infrasound monitoring for atmospheric studies: challenges in middle atmosphere dynamics and societal benefits*, pp. 209–248. DOI: 10.1007/978-3-319-75140-5_6.

Miller, Thomas P, McGimsey, Robert G, Richter, Donald H, Riehle, James R, Nye, Christopher J, Yount, M Elizabeth and Dumoulin, Julie A (1998). *Catalog of the historically active volcanoes of Alaska*. United States Department of the Interior, United States Geological Survey.

Ouden, Olivier F. C. den, Smets, Pieter S. M., Assink, Jelle D. and Evers, Läslo G. (2021). "A Bird's-Eye View on Ambient Infrasonic Soundscapes". In: *Geophysical Research Letters* vol. 48, no. 17, e2021GL094555. DOI: 10.1029/2021GL094555.

Pierce, Allan D (2019). *Acoustics: an introduction to its physical principles and applications*. Third. Springer. DOI: 10.1007/978-3-030-11214-1.

Preparatory Commission for the Comprehensive Nuclear-Test-Ban Treaty Organization, The Provisional Technical Secretariat (2011). *The virtual Data Exploitation Centre (vDEC)*. Accessed on 7 March, 2023.

Rao, K Deergha and Swamy, Madisetti NS (2018). *Digital signal processing: Theory and practice*. Springer. DOI: 10.1007/978-981-10-8081-4.

Rayleigh, John William Strutt Baron (1896). *The theory of sound*. Vol. 2. Macmillan.

Rind, David and Donn, William L (1975). "Further use of natural infrasound as a continuous monitor of the upper atmosphere". In: *Journal of Atmospheric Sciences* vol. 32, no. 9, pp. 1694–1704. DOI: 10.1175/1520-0469(1975)032<1694:FUONIA>2.0.CO;2.

Rind, David H and Donn, William L (1978). "Infrasound observations of variability during stratospheric warmings". In: *Journal of Atmospheric Sciences* vol. 35, no. 3, pp. 546–553. DOI: 10.1175/1520-0469(1978)035<0546:IOOVDS>2.0.CO;2.

Rost, Sebastian and Thomas, Christine (2002). "Array seismology: Methods and applications". In: *Reviews of geophysics* vol. 40, no. 3, pp. 2–1. DOI: 10.1029/2000RG000100.

— (2009). "Improving seismic resolution through array processing techniques". In: *Surveys in Geophysics* vol. 30, no. 4-5, pp. 271–299. DOI: 10.1007/s10712-009-9070-6.

Saurel, Jean-Marie, Hellman, Sidney, Casey, Robert, Hagerty, Mike, Lisowski, Stefan, Pardo, Constanza, Pedersen, Helle A., Péquegnat, Catherine, Ronan, Tim, Schaeffer, Jonathan, Sikhotskyi, Oloksandr, Templeton, Marie, Trabant, Chad and Wolyniec, David (May 2020). *Yasmine: a new tool for stationXML*. Videos.

Schweitzer, Johannes, Fyen, Jan, Mykkeltveit, Svein, Gibbons, Steven J, Pirli, Myrto, Kühn, Daniela and Kvaerna, Tormod (2012). "Seismic arrays". In: *New manual of seismological observatory practice 2 (NMSOP-2)*. Ed. by Bormann, Peter. Deutsches GeoForschungsZentrum GFZ, pp. 1–80. DOI: 10.2312/GFZ.NMSOP-2_CH9.

Schweitzer, Johannes, Köhler, Andreas and Christensen, Jon (Jan. 2021). "Development of the NORSAR Network over the Last 50 Yr". In: *Seismological Research Letters* vol. 92. DOI: 10.1785/0220200375.

Smets, Pieter, Assink, Jelle and Evers, Läslo (2019). "The Study of Sudden Stratospheric Warmings Using Infrasound". In: *Infrasound Monitoring for Atmospheric Studies: Challenges in Middle Atmosphere Dynamics and Societal Benefits*. Ed. by Le Pichon, Alexis, Blanc, Elisabeth and Hauchecorne, Alain.

Cham: Springer International Publishing, pp. 723–755. ISBN: 978-3-319-75140-5. DOI: 10.1007/978-3-319-75140-5_23.

Smets, Pieter S. M., Assink, Jelle D., Le Pichon, Alexis and Evers, Läslo G. (2016). "ECMWF SSW forecast evaluation using infrasound". In: *Journal of Geophysical Research: Atmospheres* vol. 121, no. 9, pp. 4637–4650. DOI: 10.1002/2015JD024251.

Smets, Pieter S. M. and Evers, Läslo G. (2014). "The life cycle of a sudden stratospheric warming from infrasonic ambient noise observations". In: *Journal of Geophysical Research: Atmospheres* vol. 119, no. 21, pp. 12–084. DOI: 10.1002/2014JD021905.

Smets, Pieter S. M., Evers, Läslo G., Näsholm, Sven Peter and Gibbons, Steven J. (2015). "Probabilistic infrasound propagation using realistic atmospheric perturbations". In: *Geophysical Research Letters* vol. 42, no. 15, pp. 6510–6517. DOI: 10.1002/2015GL064992.

Smirnov, Alexandr, De Carlo, Marine, Le Pichon, Alexis, Shapiro, Nikolai M and Kulichkov, Sergey (2021). "Characterizing the oceanic ambient noise as recorded by the dense seismo-acoustic Kazakh network". In: *Solid Earth* vol. 12, no. 2, pp. 503–520. DOI: 10.5194/se-12-503-2021.

Synnevag, Johan Fredrik, Austeng, Andreas and Holm, Sverre (2007). "Adaptive beamforming applied to medical ultrasound imaging". In: *IEEE transactions on ultrasonics, ferroelectrics, and frequency control* vol. 54, no. 8, pp. 1606–1613. DOI: https://doi.org/10.1109/TUFFC.2007.431.

Szuberla, Curt AL and Olson, John V (2004). "Uncertainties associated with parameter estimation in atmospheric infrasound arrays". In: *The Journal of the Acoustical Society of America* vol. 115, no. 1, pp. 253–258. DOI: 10.1121/1.1635407.

The ObsPy Development Team (Feb. 2019). *ObsPy 1.1.1*. Version 1.1.1. DOI: 10.5281/zenodo.1040770.

Thomson, Richard E. and Emery, William J. (2014). "Chapter 5 – Time Series Analysis Methods". In: *Data Analysis Methods in Physical Oceanography (Third Edition)*. Ed. by Thomson, Richard E. and Emery, William J. Third Edition. Boston: Elsevier, pp. 425–591. ISBN: 978-0-12-387782-6. DOI: 10.1016/B978-0-12-387782-6.00005-3.

Tripathi, Om P, Baldwin, Mark, Charlton-Perez, Andrew, Charron, Martin, Cheung, Jacob CH, Eckermann, Stephen D, Gerber, Edwin, Jackson, David R, Kuroda, Yuhji, Lang, Andrea et al. (2016). "Examining the predictability of the stratospheric sudden warming of January 2013 using multiple NWP systems". In: *Monthly Weather Review* vol. 144, no. 5, pp. 1935–1960. DOI: 10.1175/MWR-D-15-0010.1.

UAF Geophysics team (2023). *Codes for seismology, infrasound, and geodesy at the University of Alaska Fairbanks*.

van Trees, H. L. (2004). *Optimum Array Processing: Part IV of Detection, Estimation, and Modulation Theory*. DOI: 10.1002/0471221104.

Vera Rodriguez, Ismael, Näsholm, Sven Peter and Le Pichon, Alexis (2020). "Atmospheric wind and temperature profiles inversion using infrasound: An ensemble model context". In: *The Journal of the Acoustical Society of America* vol. 148, no. 5, pp. 2923–2934. DOI: 10.1121/10.0002482.

Virtanen, Pauli, Gommers, Ralf, Oliphant, Travis E., Haberland, Matt, Reddy, Tyler, Cournapeau, David, Burovski, Evgeni, Peterson, Pearu, Weckesser, Warren, Bright, Jonathan, van der Walt, Stéfan J., Brett, Matthew, Wilson, Joshua, Millman, K. Jarrod, Mayorov, Nikolay, Nelson, Andrew R. J., Jones, Eric, Kern, Robert, Larson, Eric, Carey, C J, Polat, İlhan, Feng, Yu, Moore, Eric W., VanderPlas, Jake, Laxalde, Denis, Perktold, Josef, Cimrman, Robert, Henriksen, Ian, Quintero, E. A., Harris, Charles R., Archibald, Anne M., Ribeiro, Antônio H., Pedregosa, Fabian, van Mulbregt, Paul and SciPy 1.0 Contributors (2020). "SciPy 1.0: Fundamental Algorithms for Scientific Computing in Python". In: *Nature Methods* vol. 17, pp. 261–272. DOI: 10.1038/s41592-019-0686-2.

Vorobeva, Ekaterina, De Carlo, Marine, Le Pichon, Alexis, Espy, Patrick Joseph and Näsholm, Sven Peter (2021). "Benchmarking microbarom radiation and propagation model against infrasound recordings: a vespagram-based approach". In: *Annales Geophysicae* vol. 39, no. 3, pp. 515–531. DOI: 10.5194/angeo-39-515-2021.

Waxler, Roger and Gilbert, Kenneth E (2006). "The radiation of atmospheric microbaroms by ocean waves". In: *The Journal of the Acoustical Society of America* vol. 119, no. 5, pp. 2651–2664. DOI: 10.1121/1.2191607.

Wikipedia page on the US standard atmosphere (Apr. 2023). URL: https://en.wikipedia.org/wiki/U.S._Standard_Atmosphere.

Willemann, Raymond J (2009). "Data-Type Bulletin IMS1.0: Short". In: *New Manual of Seismological Observatory Practice (NMSOP)*. Deutsches GeoForschungsZentrum GFZ, pp. 1–8. DOI: 10.2312/GFZ.NMSOP-2_IS_10.1.